Real-time *In-situ* Monitoring and Control of Silicon Epitaxy By Fourier Transform Infrared Spectroscopy

by

Zhen-Hong Zhou

Science Master, Electrical Engineering and Computer Science
Massachusetts Institute of Technology, (1991)

Bachelor of Science, Electrical Engineering
Polytechnic University, (1989)

Submitted to the
Department of Electrical Engineering and Computer Science
in Partial Fulfillment of the Requirements for the Degree of

Doctor of Philosophy

at the

Massachusetts Institute of Technology

December 1993

© Massachusetts Institute of Technology, 1993

Signature of Author ______________________
Department of Electrical Engineering and Computer Science
December 28, 1993

Certified by ______________________
Rafael Reif
Professor of Electrical Engineering and Computer Science
Director, Microsystems Technology Laboratories
Thesis Supervisor

Accepted by ______________________
Campbell L. Searle
Chairman, Departmental Committee on Graduate Students

MASSACHUSETTS INSTITUTE
OF TECHNOLOGY

JUL 13 1994

ARCHIVES

Real-time In-situ Monitoring and Control of Silicon Epitaxy By Fourier Transform Infrared Spectroscopy

by

Zhen-Hong Zhou

Submitted to the
Department of Electrical Engineering and Computer Science
on March 8, 1994 in Partial Fulfillment of the
Requirements for the Degree of
Doctor of Philosophy

Abstract

The objective of this thesis is to explore and demonstrate the application of sensors in various stages of a semiconductor manufacturing process development. For this research, a Fourier transform infrared spectrometer (FT-IR) is selected as a test vehicle, a low temperature silicon epitaxy process is selected as a test environment, and a low temperature silicon epitaxial chemical vapor deposition (CVD) reactor is selected as a test bed.

The procedures and results of refractive index measurements by FT-IR is reported. We observed that the refractive index of heavily doped silicon varies significantly with wavelength. We also observed that the refractive index of silicon decreases with increasing wafer temperature for long wavelengths. Furthermore, we examined the effect of refractive index dispersion on epi-film thickness measurement.

Plasma cleaning of silicon surface is investigated in real-time by attenuated total internal Fourier transform infrared (ATR-FT-IR) technique. By monitoring the vibrational modes of Si-H, H-SiO, O-H, and C-H, a successful cleaning process using a remote microwave plasma and a RF plasma is found. The cleaning process is critically depend on the flux ratio of the neutrals to that of the ionic species. A high flow rate of hydrogen gas and a low RF power plasma sputtering are required to remove silicon oxide. The results demonstrate the power of real-time monitoring for new process development and understanding.

A new emission Fourier transform infrared (E/FT-IR) technique for film thickness measurements is characterized and evaluated. Its capabilities and usefulness have been explored. For real-time process monitoring, we found that the real-time growth rate measured by the E/FT-IR is responsive to variations of process parameter(s) (e.g.temperature, pressure, and gas composition). For real-time epi-film thickness control, two control algorithm were used: 1) first past the post (FPP) method; 2) linear forecasting. A closed-loop precise epi-film thickness end-point control is demonstrated. Additionally, by real-time monitoring of the incubation time and growth rate, we are able to obtain qualitative information about the effectiveness of the predeposition wafer cleaning process. Using the optimized conditions, we have demonstrated the growth of defect free epitaxial silicon films.

Thesis Supervisor: **Dr.Rafael Reif**
Title: **Director, Microsystems Technology Laboratories**
Professor of Electrical Engineering and Computer Science

Acknowledgments

First of all, I would like to thank my thesis advisor, Professor Rafael Reif, for his guidance, encouragement, and support through out the course of this work. He provided me with many invaluable opportunities: 1) challenges of the research project which sharpened my technical skills, 2) exposures and interactions with people in industry which broadened my viewpoint, 3) recommendations for award and recognition which boosted my confidence and motivation. I thank him deeply for all these. In addition, he has always been a very considerate and generous person perceived not only by myself but also by many of his students. He always thinks what is the best for his student. I am very fortunate to have him as my thesis advisor, teacher, mentor, and idol.

The completion of this thesis would not be possible without the contributions of many colleagues. In the early days, Fuzhong Yu and I brain stormed for ideas, debated for decisions, struggled through many months of painful ground-breaking reactor design and construction work. He deserves a half of the success and failure of the epi-reactor. Moreover, I want to thank Fuzhong Yu and Isabel Yang who have made significant contributions in characterizing the FT-IR for film thickness measurements. Furthermore, I would like to thank Hyoun-Woo Kim for his expertise in XTEM analysis and Weize Chen for taking over the responsibility of the reactor. Octavio Marenzi, Philip Sheu, Prof. Emanuel Sachs, and Prof. Duane Boning are acknowledged for implementing the process control loop. I am also grateful to Prof. Duane Boning for his critical review of this thesis. In addition, I would like to acknowledge collaboration with Dr. B. Choi and Prof. M. Fliks in refractive index measurements, and Dr. Rick Gottscho and Dr. Eray Aydil of AT&T Bell Laboratories in ATR-FT-IR experiments. I want to thank Dr. Paul Langer of AT&T Bell Laboratories for supplying some of the epi wafers. Specially thanks goes to two visiting Professors from China: Dr. Zhizhen Ye of Zhejiang University and Dr. Shoushan Fan of Tsinghua University. MTL staff Joe Walsh and Paul McGrath, and TRL staff Octavio Hurtado and Joe DiMaria also deserve special thanks for technical assistance in the lab. I would like to thank Kate Paterson, Sue Peterson, and Carolyn Zaccaria for administrative assistance. A lot of very special thanks goes to Carolyn for her help whenever I needed. I would like to thank all other members in Prof.Reif's group for sharing labs, offices, ideas, discussions, etc. They are: Dr.Sergio Ajuria, Alexander Cherkassky, Dan Connelly, Chock Gan, Dr. Syun-Ming Jang, Dr. Jaegab Lee, Ken Liao, Dr. T. Miyata, Dr. Patrice Parris, Dr. Curtis Tsai, Julie Tsai, Dr. Noriyoshi Yamauchi, Dr. Tri-Rung Yew and Dr. Euijoon Yoon. In addition, I want to thank my MIT friends who made my graduate student life easier, they are: Vei-Han Chan, Andy Guo, Charles Hsu, Albert Hu, Xiaoping Jiang, Sheng Liu, Lung-Han Peng, Che-Chih Tsao, Paul Yu, and Qi Zhao.

SEMATECH and AT&T Bell Laboratories are gratefully acknowledged for funding this project. I am also grateful for the AT&T Bell Laboratories Doctoral Fellowship support during the last three years of my graduate studies.

Finally, I want to specially thank many relatives and friends outside of MIT for their love, friendship, encouragement, and emotional support. They are too numerous to name. I like to especially thank my uncle Po Chou and aunt Ming-Ze Chou, without them I would not be able to come to the USA. I would like to thank my three lovely sisters for their understanding and for sharing the family responsibility that the oldest and the only brother left behind and neglected. Special thanks goes to my sister Wujin for proof reading this thesis. Lastly, I would like to give my biggest "thank you" to my parents for their love, care, and support throughout my life.

I am dedicating this work to my grandmother for her love and care embedded deep in my heart, and to my grandfather, a traditional Chinese peasant, whose values of life have influenced and enriched mine.

Contents

1 Introduction **11**

1.1 Motivation 11

1.2 Thesis Objective 15

1.3 Thesis Organization 16

2 Sensors & Processes in Semiconductor Manufacturing **22**

2.1 Sensors 22

2.1.1 Real-time Characterization Techniques 23

2.1.2 *in-situ* Characterization Techniques 32

2.1.3 *ex-situ* Characterization Techniques 34

2.2 Identification of CVD Processes and Critical Process Parameters . . . 36

2.3 Summary 40

3 FT-IR Theoretical Background **42**

3.1 Principle of FT-IR 42
3.1.1 Theory of Fourier Transformation 43
3.1.2 Spatial Fourier Transformation using Michelson Interferometer 44
3.2 Reflection and Transmission IR Spectroscopy 49
3.3 ATR-FT-IR 51
3.4 E/FT-IR 53
3.4.1 Thermal Radiation 53
3.5 Epi-film Thickness Measurements by R/FT-IR and E/FT-IR 57

4 Refractive Index of Silicon **65**

4.1 Introduction 65
4.2 Expenmental - Reflectance Measurements 67
4.3 Data Analysis 68
4.4 Reflective Index of Silicon as a Function of Wavelength, Sample Temperature, and Dopant Concentration 70
4.4.1 Experimental Results 70
4.4.2 Effect of Dopant Concentration 76
4.4.3 Effect of Temperature 78
4.5 Effect of Refractive Index Dispersion on Film Thickness Measurements 81
4.6 Summary 84

5 ATR-FT-IR Monitoring of Plasma Cleaning **86**

5.1 Introduction 86

5.2 Experimental 87

5.3 Results and Discussions 89

5.4 Summary 100

6 Silicon Epitaxy Equipment and Process **103**

6.1 The Multi-chamber Single-wafer Chemical Vapor Deposition Reactor 103

6.1.1 Description of System Components 104

6.1.2 System Summary 107

6.2 Low Temperature Silicon Epitaxy 108

7 Applications of E/FT-IR **112**

7.1 Introduction 112

7.2 Thermal Radiation Measurements by E/FT-IR 113

7.3 Characterization of E/FT-IR for Film Thickness Measurements . . . 119

7.3.1 Limitations of FT-IR 120

7.3.2 Robustness of the E/FT-IR technique 123

7.3.3 Comparison of E/FT-IR and R/FT-IR for Film Thickness Measurement 132

7.4 Real-time Applications of E/FT-IR in Silicon Epitaxy 134

7.4.1 E/FT-IR Implementation 135

7.4.2 E/FT-IR Demonstration 136

7.4.3 E/FT-IR in Process Research 138

7.4.4 E/FT-IR in Monitoring and Control of Silicon Epitaxy 146

7.4.5 E/FT-IR in ECR Hydrogen Plasma Predeposition Wafer Cleaning Process Optimization 150

7.5 Summary 156

8 Summary and Future Recommendations **161**

8.1 Summary 161

8.2 Other Applications of E/FT-IR 163

8.3 Future Road Map 167

List of Figures

1.1 World-wide Silicon Epi Wafer Use [5] 13

1.2 Framework categorizing the tasks in this thesis 17

2.1 A comparison of eight different thermometry techniques capable of real-time temperature measurements [31] 28

2.2 A block diagram of various semiconductor device fabrication processes and the useful sensors [29] 37

2.3 Hierarchy of sensors in semiconductor manufacturing [29] 40

3.1 Schematic of a scanning Michelson interferometer inside the FT-IR spectrometer 45

3.2 (a) Interferogram of the ceramic infrared source (b) The corresponding processed interferograms – IR source spectrum after taking the Fourier transform of the interferogram in (a). 48

3.3 Calculated blackbody radiation spectra from Planck's radiation law. . 55

3.4 Comparison of (a) infrared reflection and (b) infrared emission ray-tracing diagram from a substrate and an epilayer for film thickness measurements. 59

3.5 (a) A typical measured FT-IR interferogram of a lightly doped epi-layer on a heavily doped substrate, (b) Comparison of experimentally measured R/FT-IR and E/FT-IR interferograms. 64

4.1 Schematic of the high temperature sample holder. 68

4.2 IR reflectance of several silicon samples with different resistivity. . . . 71

4.3 Refractive index calculated from the corresponding reflectance data shown above. 71

4.4 Refractive index of silicon as a function of dopant concentration for several wavelengths. 72

4.5 Temperature dependence of (a) the reflectance measurements, (b) the refractive index calculated from the reflectance data for a n-type sample with 0.004-0.005 Ω-cm resistivity. 74

4.6 Temperature dependence of (a) the reflectance measurements, (b) the refractive index calculated from the reflectance data for a p-type sample with 0.03 Ω-cm resistivity. 75

4.7 Calculated refractive index of silicon as a function of dopant concentration and wavelength. 77

4.8 Comparison of calculated and measured refractive index of silicon. . . 79

4.9 Reflectance of a lightly doped epi-film on a heavily doped substrate. . 82

4.10 Comparison of simulated interferograms using (a) a constant refractive index, (b) measured refractive index. 84

5.1 Schematic illustration of apparatus used for hybrid microwave-RF plasma cleaning of Si with real-time monitoring by ATR-FT-IR. 88

5.2 ATR-FT-IR spectrum (4 cm^{-1}, 1000 scans averaged) showing presence of H-SiO when samples are treated with only the effluent of a microwave discharge of H_2. 90

5.3 Real-time variations in (a) Si-H (integrated from 2000 to 2200 cm^{-1}), (b) O-H (integrated from 3000-3700 cm^{-1}) stretching absorptions as microwave and RF powers are sequentially turned on and off. 91

5.4 ATR-FT-IR spectra at different times during the treatment of Figure 5.3 93

5.5 ATR-FT-IR spectrum showing the effect of excessive ion bombardment. The large absorption peak at 2100 cm^{-1} is attributed to a-Si:H formed as a result of plasma damage. 95

5.6 Si <100> ATR-FT-IR transmission spectrum relative to untreated sample. The dashed curve corresponds to a process that was too rich in ion energy flux relative to the neutral atom flux (10 W RF power, 10 sccm H_2). The solid curve corresponds to an optimized process (3 W RF power, 50 sccm H_2) resulting in oxide removal and Si-H formation. Other conditions were 1 Torr and 140 W microwave power. 96

5.7 A comparison of two experiments performed under the same conditions, the result demonstrates the repeatability of the process. 98

5.8 Comparison of H_2 plasma treatment with HF dip. While both treatments remove oxides and produce Si-H, the plasma treatment is more effective in reducing hydrocarbon contamination. 99

6.1 Schematic of the horizontal cross section of the MS-CVD system . . . 105

7.1 Schematic of the E/FT-IR setup used to perform the thermal radiation measurements 114

7.2 Blackbody curves collected for: a) shiny aluminum mirror, b) 10-20 Ω-cm silicon substrate, c) 0.01-0.02 Ω-cm silicon substrate, d) 0.004-0.005 Ω-cm substrate, and e) carbon lamp black powder. 115

7.3 Comparison of the a) transmittance and b) emittance spectra collected for the same lightly doped silicon sample directly overlaid on same %T scale. Emittance spectrum is collected at 200 °C. 118

7.4 Emittance spectrum acquired at 250 °C for a heavily doped substrate (0.01 Ω-cm) with a lightly doped epi-layer. 119

7.5 Repeatability of the E/FT-IR technique for epi-film thickness measurements 127

7.6 Reproducibility of the E/FT-IR technique for epi-film thickness measurements 128

7.7 Schematic diagram of the setup for investigating the effect of wafer rotation on FT-IR film thickness measurements 130

7.8 Correlation of high temperature E/FT-IR measured values with room temperature R/FT-IR measured values [66] 134

7.9 A drawing of the E/FT-IR setup 136

7.10 Real-time thickness monitoring during a thermal CVD process 138

7.11 Growth rates of silicon as a function of temperature. 140

7.12 Real-time in-situ monitoring of growth rates for growth kinetic studies 141

7.13 Real-time in-situ monitoring of growth on various substrates 143

7.14 Real-time in-situ monitoring of process variations in a) temperature, b) gas composition 147

7.15 Precise closed-loop end-point control using real-time epi-film thickness data 149

7.16 Real-time in-situ monitoring of growth incubation time and growth rate during a CVD process 151

7.17 XTEM picture of (a) a Poly-Si film, (b) a defective epi-film, (c) a defect free epi-film. 153

7.18 XTEM picture of epi-film grown after hydrogen plasma cleaning with (a) -50 Vdc bias, (b) 0 Vdc bias. 155

7.19 (a) Real-time in-situ film thickness monitoring during a CVD process after optimized hydrogen plasma predeposition cleaning; (b). XTEM picture of the corresponding defect free epi-film. 157

8.1 Real time monitoring of an oxidation process using the E/FT-IR . . . 165

8.2 Semiconductor Industry Association (SIA) process and equipment control roadmap 168

List of Tables

2.1 A comparison of different film thickness measurement techniques . . . 41

6.1 Silicon epitaxy process conditions for both plasma cleaning and deposition 111

7.1 Effect of wafer rotation on the repeatability of epi-film thickness measurement 131

7.2 Summary of incubation time for VLPCVD at 800 °C[94] 144

7.3 Summary of plasma cleaning conditions and growth rate results. . . 152

Chapter 1

Introduction

1.1 Motivation

For nearly three decades, drastic improvements have been made to reduce critical lithographic dimensions. Manufacturing of current and future high density and small dimensional devices (e.g. a chip of 1 billion devices with minimum geometry of 0.15 μm) demands new fabrication equipment capable of producing ICs with low contamination level, high throughput and high yield. Over the past, the equipment industry has responded with a progression of tools: single process systems with loadlocks, loadlock systems with pre-clean process, and passivation capabilities. Recently, collaboration between SEMATECH, equipment manufacturers, and integrated circuit (IC) manufacturers conceptualized the idea of integrated processing using cluster tools. A cluster tool is defined as a system which integrates multiple but independently controlled (smart) vacuum chambers or modules around a central wafer handler [1]. Each of the chambers or modules is capable of performing one or more distinct functions or processes (e.g. etching, deposition) [1]. One of the enabling technologies for realizing cluster-tool based fabrication is the availability of real-time *in situ* sensors and

the integration of sensors, processes, equipment models and controllers. The major advantages of the cluster tool is summarized in the following:

- It reduces contamination which in turn increases productivity, yield and reliability of integrated circuit (IC) manufacturing.
- It reduces the number of process steps required by avoiding unnecessary cleaning steps between successive processes which are needed in conventional stand-alone equipment. Therefore throughput can be increased [2].
- It lowers cost by occupying 80% less clean room floor-space and also reduces equipment cost [3].
- It increases the equipment lifetime, because the system can be upgraded module by module.
- It utilizes a single-wafer process which allows higher process flexibility.

From the economical point of view, the market for reduced volume high margin application specific integrated circuits (ASIC) is growing rapidly [4]. Single-wafer flexible fabrication is more cost-effective for meeting the demands of ASIC markets. Computer-aided manufacturing with monitoring and controlling devices working in real-time to fine-tune processes as they occur, is a key to the realization of cluster tools and to the realization of flexible manufacturing in general.

On the processing side, shrinking device size demands for low temperature processes to minimize both vertical and lateral diffusion, and to reduce autodoping. Some novel processes, such as strained SiGe hetero-epitaxy and dielectric isolation for multi-level metals, require low temperature processing. Low temperature epitaxy is essential for the next generation of ICs [5] [6] [7] [8]. In the early 1990s, we see that accelerated use of epi has occurred through out the whole world (see Figure 1.1).

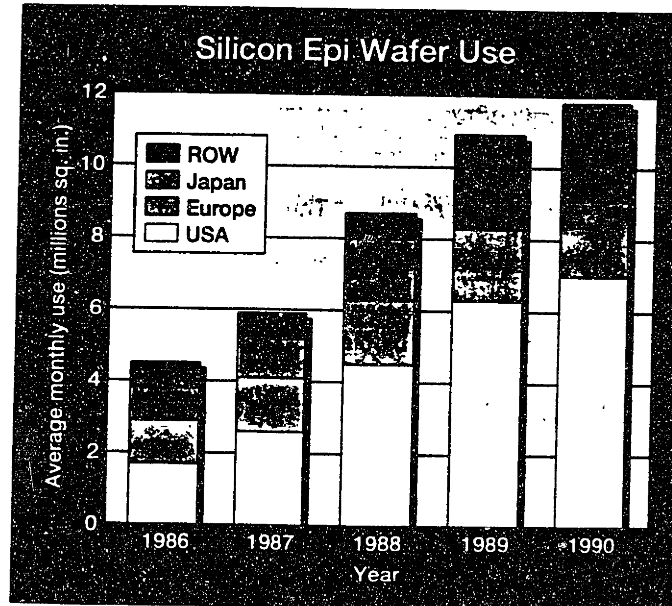

Figure 1.1: World-wide Silicon Epi Wafer Use [5]

For example, designers have used epi layers in many advanced CMOS ICs, including high pin-count ASICs, microprocessors and advanced DRAMs [5]. The epi needs for device technology are summarized in the following:

- **Metal oxide semiconductor (MOS).** PMOS needs p-type epi (5 to 15 μm) with resistivities of 5 to 10 Ω-cm. NMOS needs n-type epi (10 to 20 μm) with 5 to 10 Ω-cm resistivities.

- **Bipolar digital.** Epi for bipolar digital applications typically range from 0.5-3.0 μm thick, with the higher speed devices using the thinnest layers. The layers are n-type (usually arsenic doped) with 0.3-2 Ω-cm resistivities.

- **Bipolar linear and Power devices.** Epi-layer thickness vary from 10 μm for low voltage operational amplifiers to 100 μm for high voltage devices. The resistivities for these layers are usually n-type and cover the range of 1-100 Ω-cm for low and high voltage devices, respectively.

- **BiCMOS**. The high speed BiCMOS market will be the most rapidly growing one and therefore will show the greatest change in epi specifications. Epi thickness for BiCMOS devices (0.5 to 3.0 μm) are similar to those for bipolar devices. Resistivity requirements vary widely over the range of 1-20 Ω-cm and may be either p-type or n-type.

- **Heterojunction bipolar**. Silicon-germanium heterojunction bipolar transistor (HBT) technology should move into production in the near future. An agreement between IBM and Analog Devices for the joint design, manufacturing, and marketing of a radio-frequency and mixed-signal SiGe BiCMOS integrated circuit (IC), was announced at the recent (December 1993) International Electron Devices Meeting (IEDM) [9]. Their SiGe BiCMOS IC, fabricated by integrating SiGe HBT with digital CMOS, may lead to single-chip, digital telephones. The deposition of Si-Ge alloys for heterojunction bipolar application requires extremely tight control of the growth rate and germanium composition. Additionally, low temperature processing (less than 800 °C) is a must.

Clearly, the epi-film thickness will decrease with time, so that autodoping and solid state diffusion can not be tolerated. These trends are confirmed in the recent Semiconductor Technology Workshop Working group report by the Semiconductor Industry Association (SIA) [10]. The SIA report selected *in-situ* doping of silicon as one of the critical success factors in film deposition, and low temperature CVD silicon is recommended as a possible solution. The SIA roadmap forecasted an epi-layer thickness requirement of 2 μm with variability of 3% in 1995. Moreover, it also forecasted an epi-layer thickness requirement of 1 μm in 1998. Today's epi development work revolves around low-temperature processing, addressing problems associated with autodoping, and dopant migration associated with epi deposition.

The trend is clear: thinner and better controlled epitaxial layers will be required in the future. The ability to probe semiconductor surfaces under a variety of

process conditions is important because it enables us to monitor the process *in situ* and in real-time. We have thus chosen to study *in situ* monitoring and feedback control of a low temperature silicon epitaxy process in a cluster tool compatible equipment. The motivation of this project is to increase flexibility in semiconductor manufacturing with the following goals:

- Design and build an epitaxial system that is consistent with cluster tools concept, so that it can be severed as a test bed for sensor demonstrations.
- Explore new *in situ* sensors and demonstrate their application in process monitoring, control and optimization.

1.2 Thesis Objective

This section outlines the areas of this thesis research. The objective is to explore and demonstrate the application of sensors in various stages of a semiconductor manufacturing process development. For this research, a Fourier transform infrared spectrometer (FT-IR) is selected as a test vehicle, a low temperature silicon epitaxy process is selected as a test environment, and a silicon epitaxial chemical vapor deposition (CVD) reactor is selected as a test bed.

An FT-IR spectrometer can be used in many different ways to measure: 1) transmission, 2) reflection, 3) emission, and 4) attenuated total internal light reflection. The following is a brief summary of their applications:

In the *ex-situ* or on-line mode, FT-IR can be used to measure impurity (e.g. carbon and oxygen) concentrations by infrared transmission or reflection absorption spectroscopy. The FT-IR can also be used to measure film thickness and thickness uniformity, and refractive index by infrared interferometry and reflection, respectively.

The thickness and thickness uniformity measurements may be used for on-line quality control as well as run-by-run statistical process control [11]. The refractive index data may be used to increase the accuracy of the film thickness measurements.

In the *in-situ* real time mode, the FT-IR can be used to monitor surface chemistry during plasma cleaning processes, using an attenuated total internal reflection (ATR-FT-IR) technique. Although the ATR-FT-IR technique is not suitable for manufacturing application, it may be used for rapid process research, development, and optimization. Real-time monitoring of surface chemistry also gives insight to the understanding of the process and reaction kinetics. Moreover, the FT-IR can be used to measure impurity concentration by infrared emission spectroscopy. It can also be used to measure film thickness during the process by infrared emission interferometry. The real-time film thickness measurements allow us to observe incubation times and to obtain deposition rates. A qualitative evaluation of film quality can be accomplished by monitoring the incubation time. Furthermore, real-time growth rates may be fed into process models and these growth rate data will give insights to the understanding of the growth kinetics. For manufacturing applications, real-time thickness data may be used for real-time process monitoring and control, as well as end-point process termination.

This thesis is centered on the applications of FT-IR spectroscopy in the context of silicon epitaxy. A summary of the thesis framework is illustrated in the following block diagram (Figure 1.2).

1.3 Thesis Organization

In Chapter 2, a review of sensors and chemical vapor deposition (CVD) processes is given. The sensors, described in Section 2.1, are classified as real-time, *in-situ*,

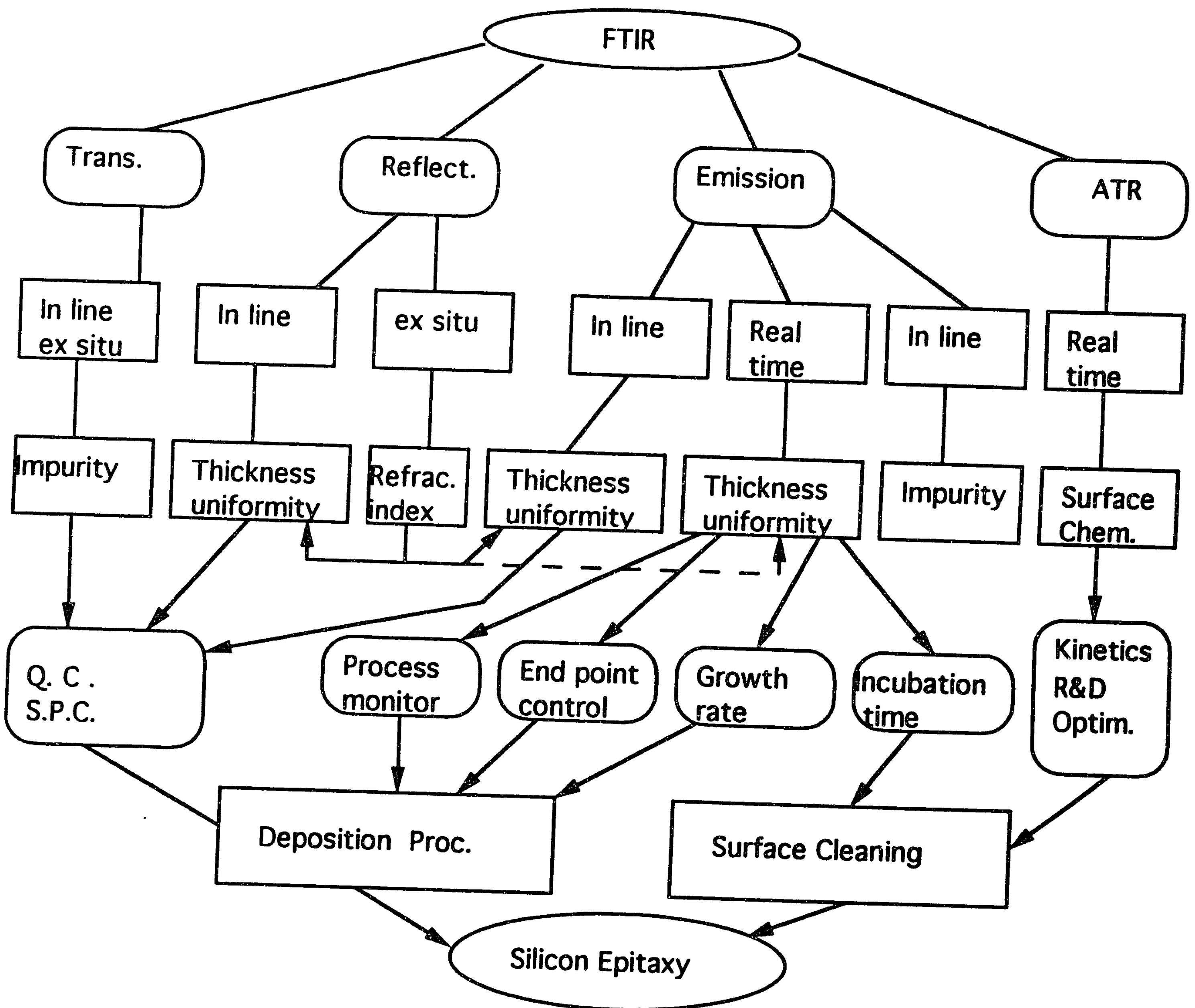

Figure 1.2: Framework categorizing the tasks in this thesis

and *ex-situ* types. Real-time means during process; *in-situ* means inside the process equipment; *ex-situ* means outside the process equipment. They are divided in three categories. The first category of sensors consist primarily of optical based sensors that have the capability of real-time *in-situ* applications. The second category of sensors consist primarily of electron or x-ray based sensors that can be utilized for *in-situ* applications but not for real-time applications. The last category of sensors is usually destructive and requires sample preparation. They can only be performed in dedicated equipment. In Section 2.2, some of the CVD processes are reviewed and critical process parameters are identified. The processes are: a) CVD metal, b) CVD dielectrics, c) CVD amorphous and polycrystalline silicon, and d) CVD epitaxial silicon. The critical parameters for each of these processes are determined by various considerations such as their impact on the overall device performance and manufacturing yield. Finally, a summary is given in Section 2.3.

The theoretical background of Fourier Transform Infrared Spectroscopy (FT-IR) is presented in Chapter 3. There are several different ways that FT-IR can be used. It can be used in reflection and transmission mode (generally referred to as FT-IR); it can be used in attenuated total internal reflection mode (ATR-FT-IR); and it can also be used in emission mode (E/FT-IR). First, the basic principles of Fourier transformation and Michelson Interferometer are described in Section 3.1. In Section 3.2, the principle of reflection and transmission FT-IR is described. In Section 3.3, the principle of ATR-FT-IR is described. In Section 3.4, the principle of E/FT-IR is described. Finally in Section 3.5, fundamentals of epi-film thickness measurements using both R/FT-IR and E/FT-IR is presented in detail.

In Chapter 4, the effects of refractive index dispersion on epi-film thickness measurement is examined. This is an example of using the reflection FT-IR to obtain critical parameters (in this case the refractive index) for epi-film thickness measurement. A brief introduction for this work is presented in Section 4.1. The experimen-

tal procedures and the apparatus for refractive index measurements using a Fourier Transform Infrared Spectrometer is described in Section 4.2. In Section 4.3, data analysis procedures and refractive index calculation based on measurement data are presented. In Section 4.4, the experimental results as well as theoretical calculation of the refractive index are compared. The effect of dopant concentration and wafer temperature on the refractive index of silicon is analyzed in detail. In Section 4.5, a simulation of the interferogram using a constant index is compared with that using the experimentally measured refractive indices. The comparison clearly shows that the spectral dispersion of the refractive index cannot be neglected for epi-film thickness measurement. Finally, a summary for this Chapter is provided in Section 4.6.

In Chapter 5, a study of silicon surface cleaning using hydrogen based plasma is presented. The cleaning process is monitored in real-time using the ATR-FT-IR technique. This monitoring is an example of using ATR-FT-IR for process development. The following questions are addressed in this chapter: 1) can a silicon surface be cleaned using atomic hydrogen generated from a remote microwave plasma (with no ion bombardment)? 2) what is happening on the silicon surface during plasma cleaning and what is the role of ions? and 3) can we use the ATR-FT-IR technique for end-point detection of the cleaning process? Section 5.1 is a brief introduction to this work. The experimental apparatus is described in Section 5.2. In Section 5.3, real-time monitoring results are presented and explanations of those experimental observations are provided. The answers to the above questions, based on experimental evidences, are summarized in Section 5.4

A description of the multi-chamber single-wafer chemical vapor deposition (MS-CVD) reactor and low temperature silicon epitaxy is given in Chapter 6. The reactor design is consistent with the cluster tool concept. A detailed description of the MS-CVD system is given in Section 6.1. The MS-CVD system is designed with a

total of five chambers. Four of the chambers have been installed, and the fifth one is reserved for future expansion. The four chambers are named: Load Lock, Analysis, CVD, and Electron Cyclotron Resonance (ECR). All chambers are constructed using chemically polished 304 stainless steel. Excluding the Load Lock chamber, the others are designed to achieve UHV. In Section 6.2, a low temperature silicon epitaxy process is presented. The process consists of two steps: 1) pre-deposition wafer cleaning, and 2) deposition. Wafer cleaning is done *in-situ* by plasma, specifically, ECR hydrogen plasma. A discussion of ECR hydrogen plasma is also given in this section.

In Chapter 7, several applications of emission FT-IR and their results are presented. E/FT-IR is well suited for monitoring high temperature processes. A brief introduction is given in Section 7.1. An example of using E/FT-IR for thermal radiation measurement is presented in Section 7.2. The results lead to a better understanding of the radiative properties of silicon which is important for subsequent film thickness measurement using E/FT-IR. In Section 7.3, the characteristics of E/FT-IR for film thickness measurement is presented. Limitations, robustness, and comparisons to conventional FT-IR technique are reported in detail. Issues such as E/FT-IR's repeatability, reproducibility, and the effect of wafer rotation are evaluated. In Section 7.4, the application of E/FT-IR for real-time silicon epitaxy process monitoring and control is presented. The experiments are carried out in the MS-CVD reactor. The E/FT-IR implementation for real-time application is described in Section 7.4.1. The application of real time E/FT-IR in studying kinetics of low temperature and low pressure epitaxial silicon CVD process is presented in Section 7.4.2. In Section 7.4.3, silicon epi-film thickness is monitored in real-time using E/FT-IR. The results are fed-back for precise epi-film thickness control. The application of E/FT-IR for effective monitoring of epi-film thickness, growth rate and incubation time is demonstrated. Monitoring of silicon epitaxy is accomplished by observing growth rate changes due to changes in process parameters (e.g. temperature, gas composition). A closed-loop film thickness control based on real-time E/FT-IR data is demonstrated. In Section

7.4.4, an application of E/FT-IR for optimizing the predeposition hydrogen plasma cleaning process is illustrated. By monitoring the growth rate and incubation time following the plasma cleaning, effectiveness of the cleaning process can be assessed indirectly. Consequently, many time consuming and costly post-deposition material characterization steps can be eliminated. Thus, plasma cleaning process optimization time is shortened and post-deposition material characterization cost is reduced. Finally, a summary of this Chapter is provided in Section 7.6.

In Chapter 8, the conclusions of this thesis are summarized, including major results from several different applications of the FT-IR and their implications in semiconductor manufacturing. Future recommendations are provided based on these conclusions. Finally, the future role of sensors in semiconductor manufacturing is outlined according to the SIA road map.

Chapter 2

Sensors & Processes in Semiconductor Manufacturing

2.1 Sensors

Realizing the importance of sensors in monitoring and control of semiconductor processes, especially in the emerging single-wafer cluster tool manufacturing environment, We will summarize several different types of sensors that we have encountered within the past several years, as well as some of the sensors we evaluated in the beginning of this thesis research. This is by no means a complete survey of the sensor field, but it serves the purpose of giving the reader a general perspective. In reviewing these sensors, we provide references, and when possible, identify pioneer(s) of that particular field for the reader to probe further.

We have classified the different types of sensors into three categories: 1) the real-time sensors, 2) *in-situ* sensors, and 3) *ex-situ* sensors. Real-time sensors can make measurements during process; *in-situ* sensors can make measurements in be-

tween processes within the process equipment, but can not make measurements during process; *ex-situ* sensors can only take measurements ouside the process equipment. All these sensors are important for semiconductor manufacturing. For real-time sensors, the measurement environment is uncontrollable (determined by a particular process), their availability is limited and they tend to be process specific. Real-time sensors can provide information about a process as it occurs, therefore enabling adaptive process control. On the other hand, *in-situ* sensors can provide pre-process and/or post-process measurements which are useful for run-by-run control. In general, real-time sensors can often be used as *in-situ* sensors, they are also referred to as real-time *in-situ* sensors. Finally, because *ex-situ* sensors are dedicated to a particular measurement, they provide the benchmark information for other types of sensors and for sensor calibration. The first category of sensors consist primary of optical based sensors that have the capability of real-time *in-situ* applications. The second category of sensors consist primary of electron or x-ray based sensors that can be utilized for *in-situ* applications, but not for real-time applications. The last category of sensors is destructive and requires sample preparation. It can only be used *ex-situ* in dedicated equipment. A brief description of some sensors in each category is given next.

2.1.1 Real-time Characterization Techniques

In the last few years, optical characterization techniques for process and materials have grown tremendously. Because these techniques are non-contacting, non-invasive, and requires no sample preparation, they are well suited for real-time *in-situ* process monitoring. In this section, we review some of the optical characterization techniques, and give examples of problems they address and solutions they contribute.

Photoluminascence and Laser Induced Fluorescence

Photoluminascence (PL) is the re-emission of optical radiation as a result of

optical excitation by a laser with typically higher photon energy. Physical properties of the sample can be monitored from its photoluminascence spectrum. For example, PL intensity is sensitive to changes in surface recombination velocity and band bending. R.A. Gottscho and his group demonstrated the application of PL for real-time *in-situ* monitoring of GaAs surface cleaning and passivation using plasmas [12]. The passivation treatment reduces the surface antisite defect density that pins the Fermi level near midgap; as a result the PL intensity increases. In that work, PL is used to obtain an in depth understanding of the cleaning and passivation mechanism and can be used to optimize those conditions. A similar optical technique is the Laser Induced Fluorescence Spectroscopy (LIF). It is generally applied to characterize gas species (e.g. plasma). It has been used to measure radical and charged particle densities and velocity distributions, gas temperatures, and electric fields in plasmas. High sensitivity plus good spatial and temporal resolutions make LIF a very versatile technique. R.A. Gottscho and his group have proven LIF to be a useful and effective optical technique for real-time *in-situ* plasma diagnostics [13].

Photoreflectance and Reflectance Difference Spectroscopy

Photoreflectance is based on the idea of modulation spectroscopy. Instead of directly measuring an optical spectrum, the derivative with respect to some parameter (e.g. electric field) is evaluated. In Photoreflectance, the sample structure (e.g. bandgap, surface states, quantized states) is modulated by photo-excited electron/hole pairs which are created by a pump beam chopped by a mechanical chopper or acousto-optic modulator. The corresponding normalized change in the optical properties is measured by another probe beam. F.H. Pollak led the team that demonstrated the application of photoreflectance in the determination of substrate temperature (GaAs, InP), and alloy composition (GaAlAs, InGaAs) during growth at elevated temperatures. The team also evaluated interfacial quality of a strained layer $In_{0.2}Ga_{0.8}As/GaAs$ single quantum well, measured the bandgap energy

in real-time, and studied the Fermi level pinning and Schottky barrier formation [14]. Over 50 publications on this subject have been produced by this group during the past several years (1987-93). A similar reflectance measurement technique named Reflectance Difference Spectroscopy (RDS) measures the difference between the near-normal-incidence reflectances of light polarized along the two principle axes of the sample (e.g. GaAs) in the plane of its surface. New capabilities for surface analysis are being provided by RDS, which utilizes intrinsic material symmetries to suppress ordinarily dominant bulk contributions. D.E. Aspnes and his group has made significant contributions to the field of RDS [15].

Optical Emissions

Optical emission spectroscopy (OES) detects light emitted by plasma, the characteristic frequencies of the light emission serve as "fingerprints" of certain gases. Furthermore, the emission intensity is related to the concentration of those emitting species. Processes can be monitored by sensing the amplitude or amplitude-ratio changes of particular emission lines. Selection of appropriate lines can be made by considering the chemistry of the process to be monitored. OES has been applied widely in monitoring and control of plasma etching processes [16]. For example, etching of polysilicon by CF_4/O_2 plasma can be monitored by the F - 704 nm peak; plasma etching of aluminum by chlorine chemistry can be monitored by the Al - 308.2 nm peak [17]; oxide etching can be monitored by a CO line at 483.5 nm or 519.8 nm [18]. OES has also been applied in monitoring and control of plasma deposition processes [19]. An examination of the commercial equipment available suggests that a substantial effort has been made for *in-situ* monitoring and control of plasma processes. OES instruments, ranging from simple photocell to full emission spectrometers employing microprocessor control, are finding their way into commercial etching tools. OES is embedded in commercially available Lam etchers (model 490, 590, and 690) for automatic etch endpoint-detection and control. Currently, on-going efforts are being made

using advance control techniques (e.g. neural network) to take full advantage of OES data [20, 21]. As the technology continues to evolve, its potential for real-time process monitoring and control in manufacturing will be used to advantage. Ultimately, this technique could go beyond end-point detection by providing immediate feedback for adaptive process control.

Mass Spectroscopy

The mass spectrometer monitors the concentration of process gases directly. When gases enter the spectrometer they are ionized. The ionized molecular fragments, each with a specific mass-to-charge ratio, pass through a magnetic field and give rise to identifiable peaks in the mass/charge spectrum. The intensity of the peak reflects the relative abundance of the ion producing the signal. Real-time monitoring of the peak(s) for product(s) or reactant(s) allows one to detect changes due to process fluctuations. In addition, real-time measurement of the by-product(s) and reactant(s) allows one to understand the kinetics of the process, which is important for process modeling. Although the mass spectrometer is a potentially powerful analytical tool, several of its inherent limitations makes it less desirable for real-time applications. For example, the need to maintain a high vacuum housing for the detector, and the need to integrate the detector head with a vacuum system makes the technique somewhat inflexible. This is especially true since the detector head must be cleaned periodically after being contaminated. Nonetheless, the mass spectrometer with a microsampling technique is used in process monitoring and control [22, 23]. When it overcomes some of its limitations, then mass spectroscopy may become as popular as OES.

Raman Scattering Spectrosopy

Raman Spectroscopy is a form of inelastic light scattering which studies the interaction of light with lattice vibrations or electronic excitations. The identifiable features of Raman spectra are the number of peaks, their shifts, linewidths and inten-

sities, and the polarization dependence of the peaks. For example, composition can be analyzed from the types of peaks and their shifts. Local temperatures can be determined from Raman peak shifts and widths. The identification of crystallinity (e.g. single, poly, or amorphous) and measurement of grain sizes can be made from Raman linewidths, shifts and polarization properties. Similarly, damage can be identified and assessed. The magnitude and direction of localized stresses can be measured by looking at Raman shifts and the peak splittings. Also, in some semiconductors, doping levels can be measured by looking at altered or new features in the Raman spectra. Although Raman analysis has been used mostly *ex-situ* after processing, progress is being made for *in-situ* measurements [24]. Raman spectroscopy has been used to study ion implantation damage, the structure of polysilicon, silicon-on-insulator (SOI) substrates, and mechanical damage. It has also been used to analyze the composition and stress of various silicide films, TiN, and SiGe films. Some limitations of Raman spectroscopy are its cost, speed, and lateral resolution.

Temperature Measurements and Pyrometry

Process temperature is one of the most critical parameters that must be monitored and controlled accurately. This area has indeed been actively pursued by many investigators. Laser polorometry and optical diffraction thermometry [25] have been proposed for *in situ* temperature measurement. They suffer from such problems as multiple scattering, stress in the windows, stability of the laser, detector linearity, and the angles of incidence and reflection. Surface acoustic wave speed has been proposed to measure temperature [27]. However, it has yet to be proven at high temperature and parameters such as surface topology and material variations, have not been fully investigated to date. An infrared laser interferometric thermometry is reported by V.M. Donnelly for wafer temperature measurements during heating and cooling [30]. The technique circumvents many of the problems associated with pyrometry. It is based on optical interference resulting from reflections off the front

and back surfaces of a wafer that is polished on both sides. This technique has been used for temperature measurements between room temperature and 600 °C during etching and deposition. Temperature changes of 0.2 K are easily detected. Table 2.1 summarizes eight different temperature measurement techniques [31]. The reader can refer to [31] for a detailed description of all these techniques.

Name	mfg. cost	remote sensing	precision	dependence on processing	range	response time	reliability
Optical pyrometry	$2,000	easily implemented	±10-50°C	changes in emissivity	500-1600K	300ms-10s	well established
Raman scattering	$50,000-$70,000	Not possible	±50°C	unknown	77K-1500K	1sec-10sec	no info
IR Laser Interferometry	$3,800	Very flexible	± 3°C	Empirically corrected	300K-900K	300 ms or greater	no info
Optical diffraction thermometry	$30,000-$50,000	Up to 40 cm	± 2°C	Almost none	290K-1000K	1 sec	no info
Photo-acoustic thermometry	not known	not known	± 1°C in principle	not known	not known	not known	not known
Optical Fiber thermometry	$13,000-$30,000	Fiber optics	0.05%	measures emissivity	500°C-1900°C	20-1000 ms	no info
Dual wavelength pyrometry	$3,875	Fiber optics	± 0.8°C	Compensates for emissivity changes	700K-1100K	200 ms	no info
Ellipsometric pyrometry	$15,000-$30,000	Similar to pyrometry	± 1°C	Compensates for emissivity changes	500K-2500K	10 ms	no info

Figure 2.1: A comparison of eight different thermometry techniques capable of real-time temperature measurements [31].

Pyrometers are most commonly used for *in situ* non-contact temperature measurements [28]. However, the major problem is that emissivity is changing during CVD and its value is unknown. The emissivity of Si is often taken as 0.7, however, it may vary from 0.3 to 0.9 for wafers with various films deposited on them. A commonly made mistake is that a pyrometer with two or more wavelengths can permit the emissivity to be calculated. In truth, this is not the case and it works only when an accurate model of the emissivity is available which is almost always not the case.

Because the emissivity of the wafer depends on its backside surface roughness, the substrate dopant concentration, and the materials/thicknesses of the films on its surfaces. Furthermore, wafer processing may involve films being deposited on or etched from its surface, or other structure changes at its surfaces. Consequently, the optical properties of the wafer may change with time according to the materials and thickness of the various films involved in the process. To overcome these problems, M.M. Moslehi reported an emissivity-assisted pyrometry-based temperature sensor [29]. This technique uses a pulsed CO laser with 5.35 μm wavelength, and a set of three detectors which are arranged to measure the incident, reflected, and transmitted laser beam intensities. These three measurements provide the reflectance and transmittance of the wafer at 5.35 μm, which are then used to extract emissivity in real-time. The real-time emissivity measurements are fed to the process control computer which extracts the true wafer temperature from the pyrometer signal.

Laser Interferometry

Laser interferometry is the simplest real-time *in-situ* film thickness monitoring technique [32, 33]. This technique monitors the intensity of a laser beam reflected from a film and the substrate as a function of film thickness. As the film is etched or deposited, the changing film thickness causes the intensity to pass through maxima and minima corresponding to points of constructive and destructive interference. Film thickness can be calculated from the periodicity of the intensity oscillation by knowing the refractive index of the film and the laser wavelength. This is used extensively for end-point detection in plasma etching because the oscillation intensity becomes a constant when the film is completely etched. The limitation of this technique is that it can only measure relative changes in film thickness.

NanoSpec

NanoSpec is based on reflection spectrophotometry which employs the princi-

ple of optical interferometry to measure film thickness. White light is first reflected from the film and substrate, then it is reflected again from a diffraction grating before it reaches the detector. This grating disperses the white light into its component wavelengths over the rage of 390 to 800 nm. During a scan, the grating rotates so that all wavelengths of the dispersed light reaches the detector in sequence from short to long wavelengths. A reference substrate is used to eliminate the instrumental effects so that optical properties (e.g. thickness) of the film can be measured accurately. Currently, NanoSpec is mostly used in *ex-situ* mode for film thickness measurement, even though it does have some potential for real-time *in-situ* applications.

Ellipsometry

Ellipsometry measures the changes in the polarization and phase of a light beam, upon reflection from a sample surface [34]. It measures the complex reflectivity of a material which can be used to extract its physical parameters (e.g. film thickness, refractive index, and composition). Ellipsometry is used extensively to measure the thickness of dielectric films (e.g. SiO_2 and Si_3N_4) which are commonly used in the semiconductor industry. Traditionally, it was used to measure samples with only one layer of unknown film on silicon substrate. In recent years, multilayer structures have been studied using variable angle ellipsometry and/or spectroscopic ellipsometry. The application of ellipsometry, variable angle ellipsometry, spectroscopic ellipsometry, and variable angle spectroscopic ellipsometry for real-time *in-situ* semiconductor process monitoring has been extensively investigated by several groups.

J.A. Woollam leads a group using all these different ellipsometric techniques which studied a variety of materials during etching and deposition [35]. A literature search by the author's name turned out over 30 publications on this subject during the past several years (1987-93). A broad spectrum of applications of different types of ellipsometry, especially the variable angle type, can be learned from his publications. However; his work is limited to real-time *in-situ* monitoring; no attempt was

made for real-time process control. In contrast, another group led by D.E. Aspnes focused on using spectroscopic ellipsometry during molecular beam epitaxy (MBE), and organometallic chemical vapor deposition (OMCVD) growth of GaAs and related compounds for process monitoring and process control [36]. A literature search by the author's name turned out over 30 publications on this subject area during the past several years (1987-93). The most impressive achievement is the real-time closed-loop control of epitaxial $Al_xGa_{1-x}As$ composition [37]. A variety of structures, e.g. a 200 Å parabolic quantum well structure, are fabricated by varying x continuously with respect to thickness according to any given input function. The composition x is monitored and feedback controlled in real-time using spectroscopic ellipsometry. The application of spectroscopic ellipsometry in chemical vapor deposition (CVD) of amorphous silicon and SiGe, as well as carbon based thin films (e.g. SiC, Diamond), and other types of amorphous thin films has been investigated extensively by a group under R.W. Collins [38]. He also authored and coauthored over 30 publications in this area during the same time period. The applications of spectroscopic ellipsometry in rapid thermal chemical vapor deposition (RTCVD) of silicon and SiO_2, as well as hydrogen plasma cleaning of SiO_2 (by ion beam or electron cyclotron resonance (ECR) plasma) has been investigated extensively by a group under K.A. Irene [39]. His group has also published over 30 papers in this area since 1988. The real-time, closed-loop control of silicon based material etching and deposition process, using spectroscopic ellipsometry, has been demonstrated under the microelectronics manufacturing science and technology (MMST) program by a group in Texas Instruments Inc. [40, 41]. In this work, a CIM database is established along with a control architecture. A generic client-server interface is defined for sensors in machine control. This is the first closed-loop control implementation, based on an *in-situ* sensor (spectroscopic ellipsometry), demonstrated in a minifactory environment. This encouraging effort signified a trend toward moving real-time *in-situ* sensors from research laboratories and universities to factory floors.

2.1.2 *in-situ* Characterization Techniques

The techniques described in this section are primarily electron or x-ray based with the exception of optical microscopy. Stringent requirement of high vacuum or even ultrahigh vacuum limits their ability for real-time applications. Some of these techniques may still be used in real-time, for example, during molecular beam epitaxy (MBE) growth when process pressure is below 10^{-5} Torr. However, most semiconductor processes take place above 1 mTorr, and these techniques can only be used for *in-situ* characterization.

Visual inspection of wafers using optical microscopy is the simplest and most widely used monitoring technique. However, its usefulness in metrology cannot be overestimated. With the addition of a near infra-red sensitive camera, the capability of the microscope can be extended considerably. In the IR region where silicon is transparent, inspection of wafers in transmission for flaws in absorbing layers and substrates is made possible [42]. In failure analysis, emission from latch-up sites is easily detected and pin-pointed. For monitoring silicon epitaxy, Nomarski Optical Microscopy is proven to be useful. Differential interference contrast of Nomarski microscopy is a simple and versatile tool for the observation of surface morphological variation of the epilayer. Using the dark/bright field imaging techniques, the quality of the epi-layer can be roughly estimated. In general, the shape, size, and density of the observed growth pits can be characterized to reflect the success or failure of the epitaxial growth. A smooth morphology implies good film.

Another very common technique is Scanning Electron Microscopy (SEM). SEM provides better lateral (with minimum resolution of 20 to 40 $\AA$) resolution and greater field depth for examining the surface morphology of epilayers since its magnification can be increased up to 200K times. Furthermore, it can be used to identify the nuclei clusters or polycrystalline from single crystalline. The polycrys-

talline grain size can also be measured using SEM. The convenience of operation and ease of sample preparation help to make SEM a valuable diagnostic tool for gaining a wealth of information quickly.

Reflection High Energy Electron Diffraction (RHEED) is also a commonly used technique for in-line process monitoring [43]. A RHEED diffraction pattern allows one to quickly determine if the film is single crystalline or polycrystalline. It is used in real-time during MBE processes, where RHEED oscillation (periodic oscillations in specular beam intensity) is often observed. From the periodicity of the oscillation, the film thickness can be monitored to atomic scale. Low Energy Electron Diffraction (LEED) is another surface characterization technique similar to RHEED, except it uses low energy electrons. RHEED can probe surface morphology and crystallographic structure, but it does not give direct information about the chemical nature of the surface. A variation of RHEED named reflection electron energy loss spectroscopy (RHEELS), is used to directly probe surface composition (and potentially detailed surface chemistry) *in-situ* [44]. RHEELS involves the spectral analysis of RHEED electrons to examine the concentrations of surface contaminants during a low temperature *in-situ* cleaning process [45], and for compositional analysis of Ge_xSi_{1-x} alloys during growth by MBE [44]. Consequently, using this *in-situ* technique, simultaneous structural and chemical information can be obtained from the surface due to the complementary nature of RHEELS and RHEED.

Auger Electron Spectroscopy (AES) is a surface sensitive measurement technique. For this technique, a focused electron beam is directed upon a sample which interacts with the solid to produce Auger electrons, secondary electrons, and x-rays. The kinetic energy of the ejected Auger electron is measured to identify the atom from which it originated. Auger electrons originate from within 5 to 50 $\AA$ of the top surface layer making AES a surface sensitive technique, especially sensitive to contaminants such as C, N, and O [46]. AES is ideally suited for *in-situ* identifica-

tion and quantification of elemental surface impurities and their concentrations before and after pre-deposition wafer cleaning. Similarly, X-ray Photoelectron Spectroscopy (XPS) is a method for analyzing solid surfaces. XPS measures the kinetic energy of photoelectrons (x-ray) to identify and quantify elemental composition of impurities within the top 20 Å of the sample surface.

X-ray diffraction (XRD) depends on the interference phenomena occurring when x-rays interact with the sample. The diffracted x-ray intensities can be measured as a function of the angle of incidence. The resulting spectrum is generally unique for all materials, and thus can serve as a fingerprint for material identification. XRD is one of the few techniques that can measure the position of individual atoms. Double-Crystal X-ray Diffractometry (DCD) is another extremely powerful tool for rapid and nondestructive examination of the layer thickness, compositions, and strains in epitaxial layers.

2.1.3 *ex-situ* Characterization Techniques

The techniques described in this section are primarily ion or electron based. Often, sample preparation is required, and sometimes the techniques can be destructive. Therefore, they cannot be applied to either real-time or *in-situ* characterization. However, *ex-situ* characterizations can be used to verify real-time or *in-situ* results because *ex-situ* techniques are well characterized and have been used extensively over the past several decades.

Ion Channeling/Rutherford Backscattering Spectrometry (RBS): In RBS, a high energy beam of collimated helium ions is used to probe a sample. Impinged ions suffer nuclear collisions inside the sample and are backscattered. By analyzing the energy distribution of those ions reflected out of the sample, information on film thickness and structural quality can be obtained. For RBS, helium ions

are singly charged and the ion energy is 2 MeV. A well collimated beam of He^+ ions is accelerated toward the sample along its normal direction and the backscattered ions are detected by a detector at near normal incidence. The evaluation of film quality has also been carried out using the He^+ beam at a low-index direction of silicon (channeling direction, <100> in this study) so that most of the beam is steered by the atomic potentials along the aligned direction. Disorder in the epi-layers (on the order of 0.1 Å) can disrupt the channel and cause an increase in backscattering yield with respect to a perfect crystal. Therefore, the quality of the epi-layer can be determined by the ratio of the channeling yield to the random yield which is obtained by averaging the backscattered yield from all directions. The measured ratio, χ_{min}, indicates the quality of the epi-layer. For perfect Si, χ_{min} is about 2.9% depending on the collimation of the beam and the channeling direction. RBS is especially well suited as an absolute standard for other analytical techniques.

Secondary Ion Mass Spectrometry (SIMS): SIMS uses a primary ion beam to sputter the surface of a solid sample (e.g. an epitaxial layer is eroded by the sputtering process). The secondary ions thus generated are detected (with ppm to ppb detection limits) and analyzed according to their mass. Mass spectra, depth profiles, and elemental images can be obtained. Hence, the relative abundance of the sputtered species provides a direct measurement of the composition of the removed layer. Impurities (e.g. C, O, N) profiles, and dopant profiles (e.g. B, P, As, Sb) can be measured using a Cs^+ ion beam. Conversion from ion counts to concentration can be accomplished by using a sensitivity factor derived from analysis of the standard. The depth scales can be calibrated by measuring the analytical crater depth with a Dektak stylus profilometer. SIMS can be applied to characterize almost every process step including: substrate dopant levels, wafer cleans, film (dielectric, metal, and epi) depositions, and plating on packaging materials.

Transmission Electron Microscopy (TEM): Cross-sectional transmission electron microscopy (XTEM) is used extensively to characterize the structural quality of the epitaxial layer(s) and the interfaces between different layers. To optimize the growth conditions, the results of XTEM is extremely valuable. XTEM is carried out using the electron beam oriented parallel to the growth plane, such that the direct observation of the substrate, epitaxial layer(s), and interface(s) is possible. Plan-view TEM can be used for the study of thermal stability as it provides the top view of the interface(s) and allows for the direct observation of misfit dislocations.

Spreading Resistance Profile (SRP): SRP is used for measuring the thickness of diffused layers or epitaxial layers, and for establishing the impurity profile for these structures. To make a spreading resistance measurement, a known current is applied between two probes, and a voltage drop is measured across these probes to obtain a spreading resistance. To determine dopant profiles of diffused or epitaxial layers, measurements are performed on an angle lapped wafer. Knowing the angle of the taper gives the depth as a function of distance from the surface. Elaborate correction techniques and correction factors have been developed to convert this spreading resistance into carrier concentration. An ASTM standard has been developed for conducting SRP measurements [47], and the reader is referred to reference [47] for details.

2.2 Identification of CVD Processes and Critical Process Parameters

The fabrication process of an integrated circuit requires the performance of several hundred steps. A review of all these processes is beyond the scope of this thesis. However, the interested reader is referred to a comprehensive review by M.M. Moslehi

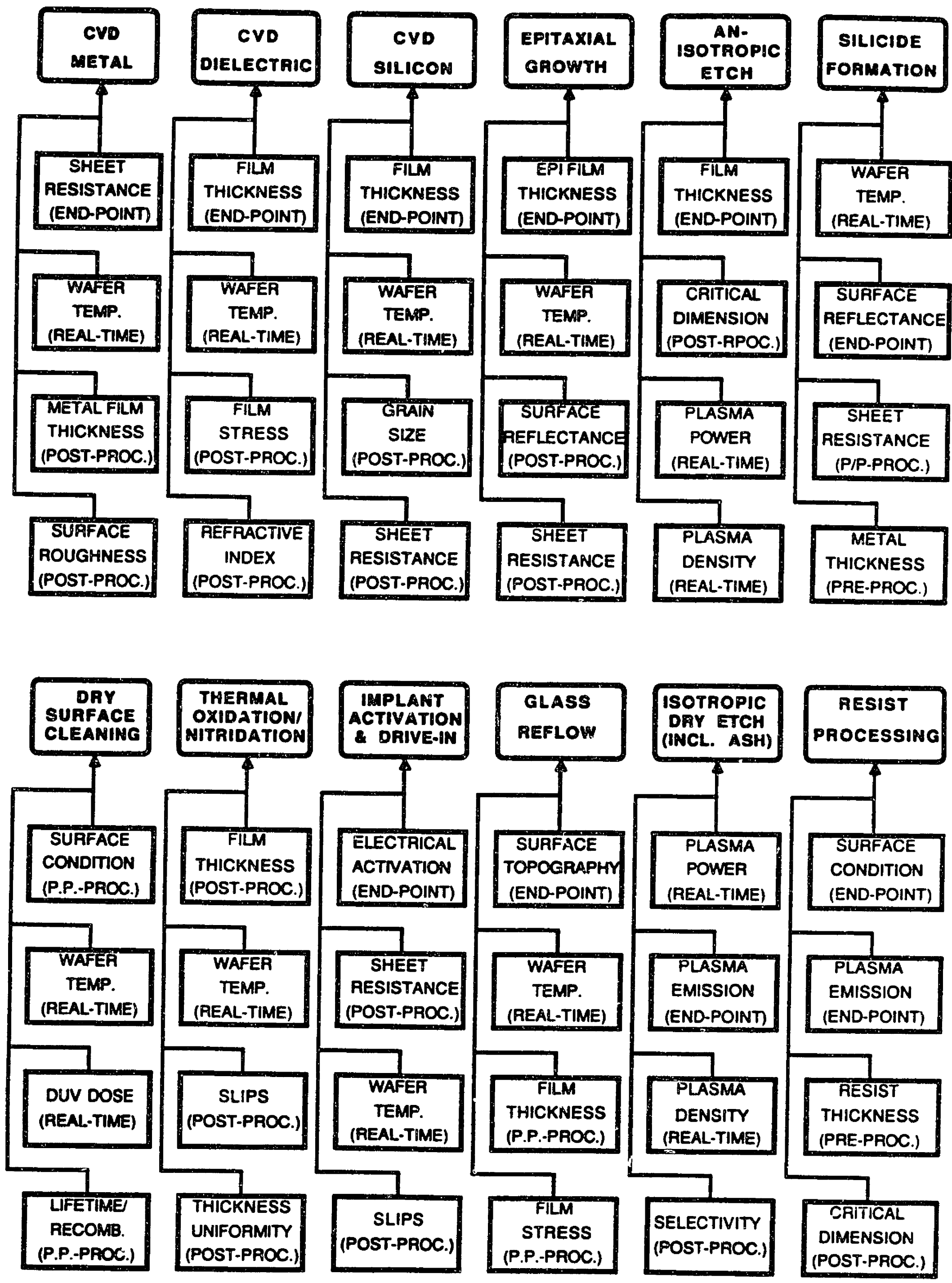

Figure 2.2: A block diagram of various semiconductor device fabrication processes and the useful sensors [27].

[29]. Figure 2.2 identifies useful *in-situ* sensors for process control in various device fabrication processes. Only chemical vapor deposition (CVD) processes are reviewed here.

There are many CVD processes required to fabricate semiconductor devices. They are: a) CVD metal, b) CVD dielectrics, c) CVD amorphous and polycrystalline silicon, and d) CVD epitaxial silicon. The critical parameters for each of these processes are determined by various considerations such as their impact on the overall device performance and manufacturing yield.

a) For metal CVD processes such as tungsten CVD, a temperature sensor is needed for real-time wafer temperature control. Precise control of wafer temperature and its uniformity in the CVD tungsten temperature range (300 °C- 550 °C) is a critical requirement in this process due to its impact on the deposition rate and process uniformity. Another useful sensor is a noninvasive sheet-resistance sensor for real-time monitoring of tungsten sheet-resistance during the CVD process. This sensor will provide the process endpoint information and will help to reduce the process parameter spread. The other two important process sensors for *in situ* monitoring are the metal film thickness sensor and the surface roughness sensors.

b) For dielectrics for CMOS gate formation by oxidation and nitridation processes, thickness, growth temperature, and uniformity of gate dielectrics are the main critical process parameters that can influence the overall device performance and manufacturing yield. As a result, one important sensor is the real-time multipoint temperature sensor for closed-loop temperature control that improves process repeatability. Another useful sensor is an ellipsometer for the measurement of gate dielectric thickness and refractive index. This sensor may reduce the overall gate dielectric thickness spread via real-time and/or delayed (next wafer) feedback control.

c) For amorphous and poly-silicon CVD processes, again, film thickness, growth

temperature and uniformity are the main critical process parameters. In addition, sheet resistance, surface roughness, and crystalline grain size sensors are also very important. Useful sensors, such as ellipsometer, nanospectrometer, reflected high energy electron diffraction (RHEED) spectrometer, fourier transform infrared (FTIR) spectrometer, and x-ray diffraction, can be used to monitor the process in real-time or *in situ*.

d) For epitaxial silicon CVD process, film thickness, growth temperature, uniformity, film resistivity, selectivity, crystalline quality, and end-point detection during pre-deposition wafer cleaning, are the critical process parameters. The epitaxial film thickness is a critical parameter that must be accurately measured and controlled. For example, it is necessary to ensure that outdiffusion and autodoping during device processing do not consume the entire epitaxial film. In addition, several bipolar transistor device parameters, such as breakdown voltage, junction capacitance, transistor gain, and high frequency performance, are dependent on the epi-layer thickness. For real-time epi-film thickness monitoring, an emission Fourier transform infrared technique (E/FT-IR) is shown in this thesis to be effective and easy to implement (see Chapter 7 for details). It may potentially be used to monitor other parameters as well. Its applications for materials characterization and process monitoring are the subjects of this thesis research. Moreover, other useful sensors including the reflected high energy electron diffraction (RHEED) spectrometer, conventional FT-IR spectrometer, and x-ray diffraction, may be used for *in situ* process monitoring. Notice that ellipsometry and nanospectrometry can only be used to measure the thickness of a thin film on a substrate which is of a different material. Hence, they are not applicable to measure thickness of a single crystalline (epi) silicon film on a silicon substrate (see Table 2.1 for a comparison of different film thickness measurement techniques). Therefore, infrared techniques like FTIR and EFTIR were the only choices.

2.3 Summary

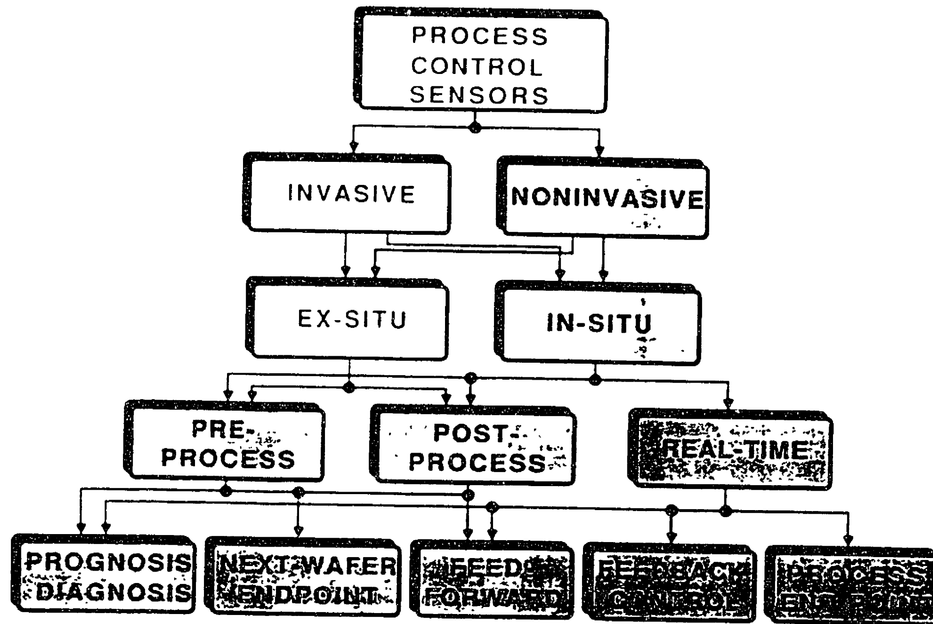

Figure 2.3: Hierarchy of sensors in semiconductor manufacturing [29].

Obviously, there is no single sensor that can monitor all the above mentioned CVD processes and their corresponding critical parameters. In some cases, however, one sensor may be applied to monitor several processes. This reduces the complexity of process monitoring and control, and at the same time reduces sensor development time. On the other hand, if several sensors may be applied to monitor one single critical parameter, then careful evaluation must be taken to select one or two sensors. Multiple sensors enable cross calibration (or checking) for better reliability, however, signal processing can become complicated. There are still some critical process parameters lacking sufficient sensors. Much work needs to be done in exploring and demonstrating novel sensor ideas and concepts. As the number of sensors increases for each process, computer algorithms need to be developed for the efficient and correct handling of multiple sensor signals (also known as sensor fusion), which further

Methods	Wavelength (μm)	Minimum Thickness(μm)	Precision (μm)	Limitation
IR Laser Interferometry	10 5	0.70 0.36	unknown unknown	can not be used to measure absolute film thickness
FT-IR	2.5-25	0.3	0.01	can not measure very thin films (<0.3μm)
NanoSpec.	0.4-0.8	0.05	<0.01	not applicable to epi-film
Ellipsometry	0.632	0.005	<0.005	not applicable to epi-film

Table 2.1: A comparison of different film thickness measurement techniques

make the appropriate decisions for feedback and/or feed-forward process control. Figure 2.3 summarizes the hierarchy of sensors in semiconductor manufacturing process monitoring and control.

Table 2.1 summarizes several different film thickness measurement techniques described in Section 2.1.1. Based on Table 2.1, we have selected the FT-IR technique for real-time monitoring of silicon epitaxial film thicknesses. The focus of this thesis is to show how one can apply the FTIR spectrometer to gather important optical data *ex-situ*, and to develop, optimize, and monitor predeposition cleaning and silicon epitaxy processes *in-situ* and in real time.

Chapter 3

FT-IR Theoretical Background

The theoretical background of the FT-IR instrument and various FT-IR techniques are presented in this chapter. First, the basic principles of Fourier transformation and Michelson interferometer are presented. This gives the reader an understanding of the FT-IR instrument. Next, the principles of various individual measurement techniques, such as reflection and transmission FT-IR, ATR-FT-IR, and E/FT-IR, is described. Finally, the fundamentals of epi-film thickness measurements using both R/FT-IR and E/FT-IR is presented in detail.

3.1 Principle of FT-IR

In this section, we will go through the details of the spatial Fourier transformation using the Michelson interferometer. First, we will analyze the scanning Michelson interferometer to derive a mathematical expression. From this expression, a linear system model will be constructed and the transfer function of the system will be found.

3.1.1 Theory of Fourier Transformation

The Fourier transform is often treated as an operation that converts a function of time (t) into a function of frequency (f). It is a widely used technique in signal processing and analysis of electric circuits and systems [48] [49]. A proof of Fourier's theorems can be found in [50]. Here, we will apply Fourier methods to the problem of interferometry. The Fourier transform of a function $i(t)$ can be found by:

$$I(f) = \int_{-\infty}^{+\infty} i(t)e^{-j2\pi ft}dt \tag{3.1}$$

and the inverse Fourier transform of I(f) is:

$$i(t) = \int_{-\infty}^{+\infty} I(f)e^{j2\pi ft}df \tag{3.2}$$

If a real function has even symmetry, its transform is real and is equal to the cosine transform. In addition, the same transformation apples in frequency-time ($f-t$) space as well as in wavenumber-displacement ($k-x$) space. Therefore, equation (3.1) and (3.2) can be re-written as:

$$I(k) = \int_{-\infty}^{+\infty} i(x)\cos(kx)dx \tag{3.3}$$

$$i(x) = \frac{1}{2\pi}\int_{-\infty}^{+\infty} I(k)\cos(kx)dk \tag{3.4}$$

Since we are dealing with transformations between k and x, we will call these spatial transformations.

3.1.2 Spatial Fourier Transformation using Michelson Interferometer

Intuitive Approach

In order to understand how the Michelson Interferometer works, we begin by consider a monochromatic light source for simplicity. Figure 3.1 shows a schematic of a Michelson Interferometer. When the movable mirror and the fixed mirror are equidistant from the beam splitter, the two beams interfere constructively. When the movable mirror moves a distance 1/4 λ, the phase change is now 1/2 λ, resulting in destructive interference. A further displacement of the mirror by 1/4 λ will again produce constructive interference. Therefore, a mathematical representation of the detected light intensity by the detector as a function of the movable mirror displacement $i(x)$ is given by [51] :

$$i(x) = I(k)\cos kx \tag{3.5}$$

where the wavenumber k is equal to $2\pi/\lambda$.

Equation (3.5) represents the interference pattern (or interferogram) of a single wavelength laser. However, if the source is a broad-band (or polychromatic) source, the detected intensity will be a summation of the source radiation over the entire k-space. Equation (3.5) becomes:

$$i(x) \approx \sum_k I(k)\cos kx \approx \int_{-\infty}^{+\infty} I(k)\cos kx dk \tag{3.6}$$

where x is the displacement of the movable mirror. Equation (3.6) tells us that the measured interferogram $i(x)$ is equivalent to an inverse spatial Fourier transform of

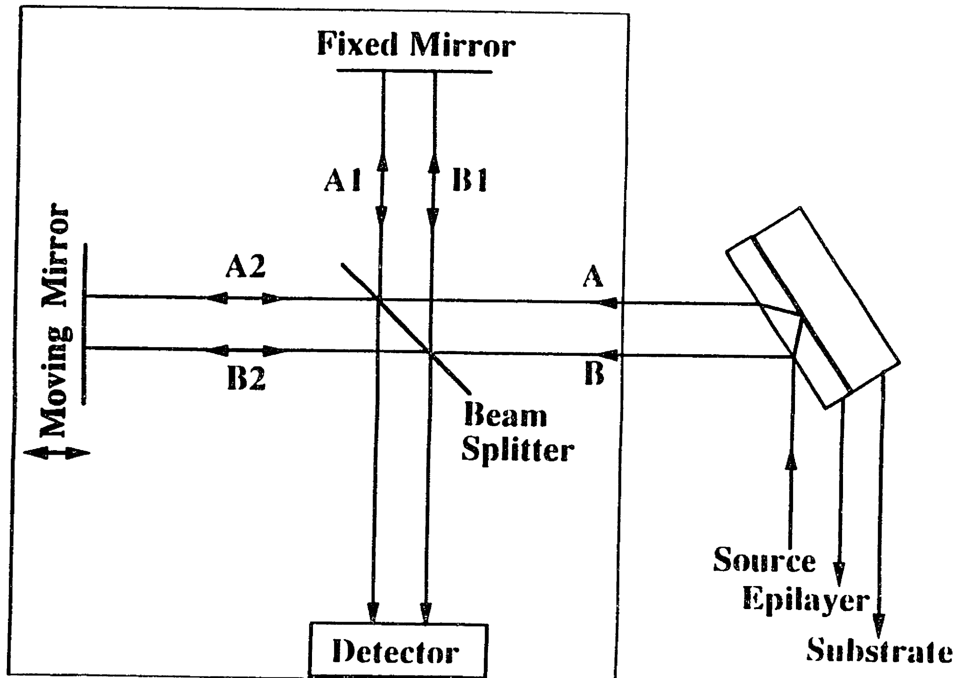

Figure 3.1: Schematic of a scanning Michelson interferometer inside the FT-IR spectrometer

the source spectrum. A Fourier transform can then be performed using a computer to obtain the radiation spectrum ($I(k)$) of the source.

Mathematical Approach

For the same monochromatic light source, its electric field (E_s) can be written as:

$$E_s = E_o e^{-jkz} \tag{3.7}$$

where E_o is the magnitude of the electric field. When this wave impinges at the beam splitter, it splits into two beams and each beam has a magnitude of $E_o/2$ (assume an ideal beam splitter is used). These two beams will be reflected back by the mirrors and finally arriving at the detector. The electric field arrived at the detector can be represented by:

$$E_D = E_1 + E_2 = \frac{E_o}{2}e^{-jk(x-2L_1)} + \frac{E_o}{2}e^{-jk(x-2L_2)} \tag{3.8}$$

where L_1 and L_2 are the distance between the beam splitter and two mirrors. In reality, what is being detected is the light intensity which can be calculated if the electric field is known. Using the electric field expression in equation (3.8), we find its intensity (I_D) to be:

$$\begin{aligned} I_D &= \langle E_D \bullet E_D^* \rangle = E_1E_1^* + E_1E_2^* + E_1^*E_2 + E_2E_2^* \\ &= \frac{1}{4}(E_o^2 + E_o^2e^{+jk(2L_1-2L_2)} + E_o^2e^{-jk(2L_1-2L_2)} + E_o^2) \end{aligned} \tag{3.9}$$

After simplification I_D becomes:

$$I_D = \frac{1}{2}I_s(1 + \cos k(2L_1 - 2L_2)) \tag{3.10}$$

where $I_s = E_o^2$. However, in a scanning Michelson interferometer, L_2 varies by the mirror movements. Let us use the variable x to denote the mirror position, and the reference point x=0 is defined when $L_1 = L_2$. Therefore equation(3.10) can be rewritten as:

$$H(k) = \frac{I_D}{I_s} = \frac{1}{2}(1 + \cos kx) \tag{3.11}$$

where H(k) is defined as the transfer function of the linear system model of the Michelson interferometer for a monochromatic source with wavenumber k. A block diagram of this is shown:

$$I_s(k) \longrightarrow \boxed{\text{H(k)}} \longrightarrow I_D(k)$$

Furthermore, if the source is a broad-band source. The detected intensity at every point in x will be a summation of the detected signal over the entire k-space.

$$\begin{aligned}
i(x) &= \sum_k I_s(k)H(k) = \int_{-\infty}^{+\infty} I_s(k)H(k)dk \\
&= \int_{-\infty}^{+\infty} I_s(k)dk + \int_{-\infty}^{+\infty} I_s(k)\cos kxdk \\
&= Constant + \int_{-\infty}^{+\infty} I_s(k)\cos kxdk \qquad (3.12)
\end{aligned}$$

Notice that the first term in equation(3.12) is constant with mirror position and only contributes to the background, therefore it can be neglected. Consequently, the resulted equation is similar to Equation 3.6, and $i(x)$ is the interferogram measured using a Scanning Michelson Interferometer.

IR spectroscopic information can be obtained from the interferogram by performing a Fourier transformation. For example, Figure 3.2(a) shows the measured raw interferogram of the glow bar ceramic IR source. Figure 3.2(b) shows the corresponding IR radiation spectrum after taking a Fourier transform. The noise and absorption bands in the spectrum are characteristic of the spectrometer itself (e.g. moisture in the ambient, optical elements, detector, etc.). The instrument contribution can be easily eliminated by spectral subtraction. This is widely used in IR spectroscopy, and is described in more detail in the next section.

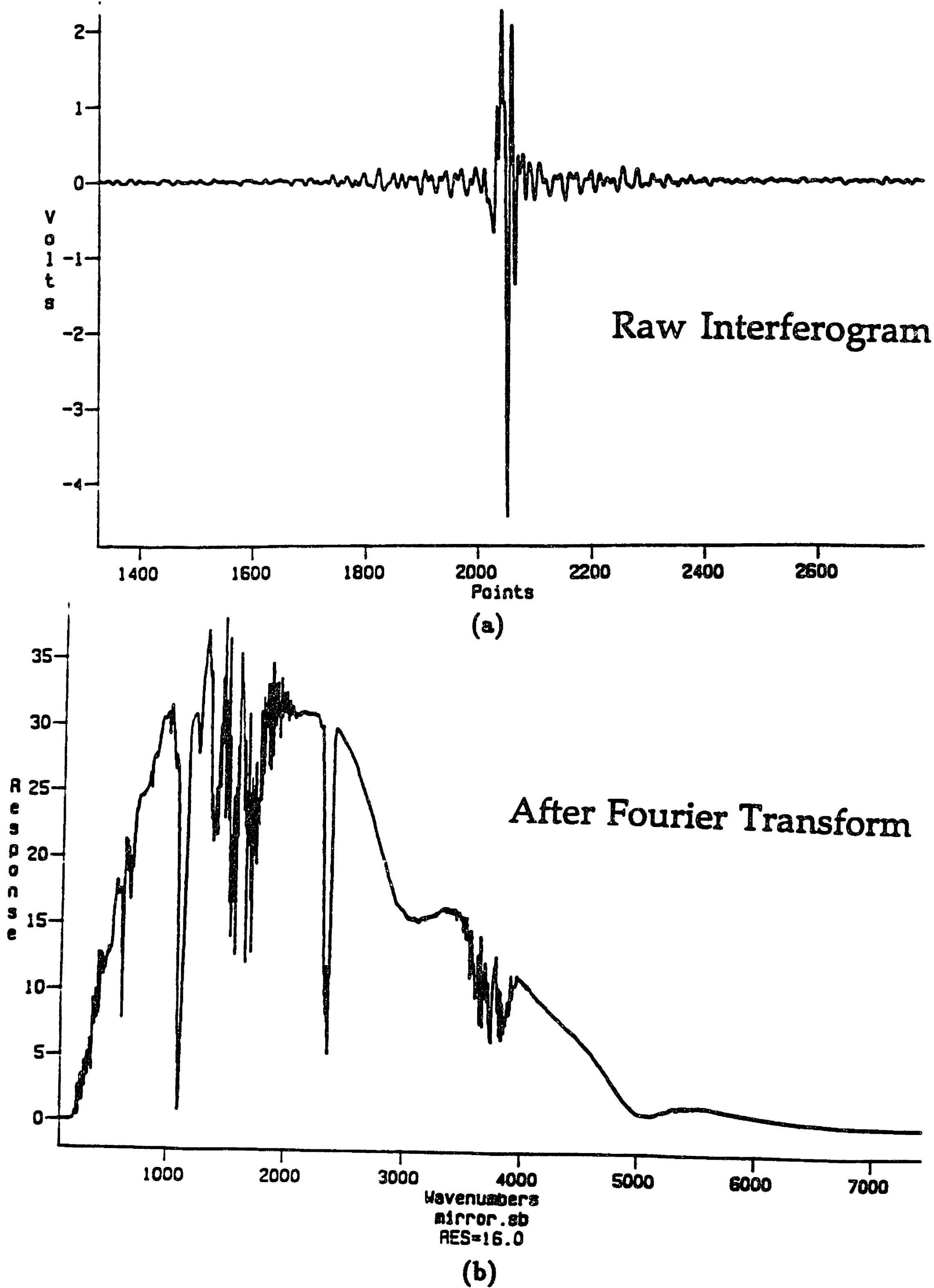

Figure 3.2: (a) Interferogram of the ceramic infrared source (b) The corresponding processed interferograms – IR source spectrum after taking the Fourier transform of the interferogram in (a).

3.2 Reflection and Transmission IR Spectroscopy

The most traditional form of IR spectroscopy is the linear absorption measurement of IR radiation after its interaction with a surface layer (e.g. Oxide, Nitride, BPSG). When a beam of light is reflected or transmitted from a material, its intensity is reduced at certain wavelengths due to absorption by chemical substances. For a transparent sample (e.g. lightly doped silicon), a transmission technique is often used. For a opaque sample (e.g. heavily doped silicon) where transmission is impossible, the reflection technique is often used. The wavelengths at which absorption occurs are the "fingerprint" of the corresponding chemical substances. The intensity of spectral bands in a FT-IR spectrum is proportional to the concentration of each substance (or impurity in the sample). Thus, absorption spectroscopy is useful for identifying impurities and measuring impurity concentrations. For both reflection and transmission, the sample spectrum ($I(\nu)$) is ratioed against a reference spectrum ($I_o(\nu)$). The absorbance as defined by Beer's law, which relates band intensity to concentration:

$$A(\nu) = -log_{10}\tau(\nu) = a(\nu)bc \tag{3.13}$$

where $\tau(\nu) = I(\nu)/I_o(\nu)$ and $a(\nu)$ are the transmittance and absorptivity at frequency ν, respectively, b is the pathlength, and c is the concentration of the absorbing species.

After obtaining the absorbance spectrum, spectral subtraction can be used for confirmation of the identity of a sample. If a reference spectrum is subtracted from a sample spectrum, and the difference is zero, it is clear that the two spectra are of the same compound. Quality control can also be performed using absorbance subtraction spectrometry. If a standard spectrum for a product of know composition is recorded, it can be used as a reference. The difference spectra will show positive or negative

bands, indicating an excess or deficiency of particular components. Tolerance limits can be set on these deviations from the standard, and the product can be rejected or accepted. The absorbance subtraction operation forms the basis of many commercial quantitative infrared systems.

A demonstration of using IR absorption spectroscopy to enhance dielectric film quality control was reported in [52]. In this work, the author studied phosphosilicate glass (PSG), borosilicate glass (BSG), and borophosphosilicate glass (BPSG) films deposited by low pressure chemical vapor deposition (LPCVD) and atmospheric pressure chemical vapor deposition (APCVD) [53]. Absorption bands of phosphorus doubly bonded with oxygen (P=O) at 1316 cm^{-1}, with Si-O at either 818 or 1080 cm^{-1}, and boron-oxygen (B-O) at 1370 cm^{-1}, were monitored *in-situ*. The authors obtained satisfactory results using IR spectroscopy to monitor and control PSG and BPSG deposition processes.

IR absorption spectroscopy is often used to identify impurities (e.g. carbon and oxygen) and measure their concentrations in silicon substrates. This analysis can also be used to infer oxygen precipitation rates. Since FT-IR detects interstitial oxygen, a reduction in the oxygen concentration after thermal cycling can be interpreted as a measure of precipitation. The presence of interstitial oxygen in silicon causes absorption of IR radiation at 1106 cm^{-1} and substitutional carbon causes absorption at 607 cm^{-1}. The detection limits at room temperature are $2.5x10^{15}$ cm^{-3} for oxygen, $5x10^{15}$ cm^{-3} for carbon, and $2x10^{14}$ cm^{-3} for nitrogen. Details of the measurement procedure can be found in the ASTM Standards [54].

3.3 ATR-FT-IR

In many applications, it is difficult to obtain useful information by reflection (external) and/or transmission absorption measurements from a sample with a very thin film. To amplify the weak absorption, it is necessary to let the IR beam traverse the film many times. A number of experiments have demonstrated that the attenuated total internal reflection (ATR-FT-IR) technique can be employed with advantage to identify and study thin film and adsorbed molecules [55, 56, 58]. Moreover, Chabal estimated that the ATR technique gives one to two orders of magnitude better signal to noise ratio than external reflections [58]. With the increasing interest in processing and understanding of semiconductor surfaces and surface reactions, the ATR-FT-IR technique has been used extensively. However, ATR-FT-IR spectroscopy is not possible for heavily doped samples and for samples at elevated temperatures above 750 K, due to absorption by dopants and thermally generated free carriers, respectively. This leaves external reflection or transmission the only alternative. A detailed review of the principles and applications of ATR-FT-IR can be found in Harrick's book [59]. A brief review of the theory is given in this section.

If the refractive indices of the sample (n_2) is greater than its surrounding medium (air in this case, $n_1 = 1$), and the angle of incidence exceeds the critical angle, the sample will act as a waveguide. At each of the points of total internal reflection, the intensity of the field drops exponentially with distance z from the reflection surface or interface:

$$I = I_o e^{-z/D} \tag{3.14}$$

This electric field is called an evanescent wave, coupled with molecular dipoles according to the usual selection rules for IR spectroscopy. The corresponding optical

absorption is measured in the reflected beam. The coupling of dipoles to the electric field takes place at every point of internal reflection, resulting in an enhanced signal to noise ratio. Thus this technique has a very high surface sensitivity. It has been reported that the ATR-FT-IR technique can monitor less than 1% of a monolayer coverage of SiH stretch mode [60]. The penetration depth D is defined as the depth where the intensity of the wave has dropped to 1/e of its value at the interface. D is a linear function of wavelength and is also dependent on the value of n_1/n_2 and the angle of incidence, Θ . This relationship is given by:

$$D = \frac{\lambda}{2\pi(sin^2\Theta - (n_1/n_2)^2)^{\frac{1}{2}}} \tag{3.15}$$

Since lightly doped silicon is transparent in IR, we were able to directly use silicon as the ATR crystal. Moreover, the refractive index of silicon (n=3.42) is relatively high, thus the critical angle for air/silicon interface is small and can be calculated by :

$$\Theta_c = sin^{-1}(1/3.42) = 17^o \tag{3.16}$$

Real-time monitoring of hydrogen plasma cleaning of the silicon surface by ATR-FT-IR is described in Chapter 5. These samples are both side polished rectangular pieces (5 cm x 2 cm x 0.05 cm) of seminsulating <100> orientation silicon, which are beveled 45° on both sides in order for multiple reflections to occur. Infrared radiation enters the input bevel at normal incidence and hits the bottom sample surface at 45°. Since 45° is greater than the critical angle for total internal reflection, the IR beam is trapped in the silicon sample. Thus the beam traverses the sample undergoing multiple internal reflections at the surface. The number of reflections from one of the surfaces is given by L/2d, where L is the length of the sample and d is the thickness. Using the dimensions of our sample, we estimate that infrared

beam undergoes 50 internal reflections from each surface during its traversal of the sample. Detailed experimental setup and results of ATR-FT-IR studies is described in Chapter 5.

3.4 E/FT-IR

To understand the principle of emission Fourier transform infrared spectroscopy (E/FT-IR), it is essential to understand the source of IR radiation. Blackbody radiation is treated by Planck's radiation law. IR radiation from a semiconductor is then treated based on the understanding of Blackbody radiation.

3.4.1 Thermal Radiation

Although we refer to blackbody radiation as "classical", its mathematical formulation is based upon quantum properties of electromagnetic radiation. Blackbody radiation is incoherent in the sense that there are an infinite set of optical frequencies present and the phase of each constituent frequency is a random function of the direction of propagation. In contrast, coherent radiation obtained from a laser can be treated as monochromatic with uniform phase. Planck's radiation law is derived in detail in Chapter 1 of [61]. Its derivation is omitted here. The blackbody radiation spectrum can be obtained using Planck's theory [62]:

$$\rho(T,\nu)d\nu = \frac{8\pi\nu^2}{c^3}\frac{h\nu}{e^{h\nu/kT}-1}d\nu \tag{3.17}$$

where T, ν, h, k are sample temperature, optical frequency, Planck's constant and Boltzmann's constant, respectively.

Figure 3.3 shows the calculated Planck radiation spectrum of a blackbody at several different temperatures. The radiation peak location is given by Wien's displacement law:

$$\lambda_{max}T = const = 2.898x10^{-3}m - K \tag{3.18}$$

where T is temperature in degree K; and λ_{max} is the wavelength at which the emission intensity is a maximum. For the sun, its temperature is at about 5700 K, its peak radiation is at $\lambda_{max} = 0.51$ μm. Therefore most thermal bodies with temperature far less than the sun's temperature emits radiation in the infrared region. Thus, a thermal radiation source is ideally suited for infrared spectroscopy. E/FT-IR is particularly important for semiconductor samples at high temperatures since ATR-FT-IR cannot be used due to the free carrier absorption problem [58]. The silicon samples are transparent in the IR region from 1 micron to 7 microns at room temperature. If we treat the heavily doped silicon substrate radiation as blackbody radiation using the above Wien's displacement law, we find that for a wafer temperature of 200 °C, the corresponding λ_m is 5.8 microns; for a wafer temperature of 800 °C, the corresponding λ_m is 2.8 microns. This falls well within the region that is transparent to silicon (1 micron to 7 micron). These simple calculations assure us that radiation emitted from the heated substrate can be transmitted through the silicon film, and can be collected and subsequently analyzed.

Theoretically, the emission spectrum from a semiconductor can also be calculated based on Planck's theory. If the free carrier absorption coefficient κ is known, the emission from a semiconductor can be found [62]:

$$P(T,\nu) = \frac{c}{4\pi}n^2(\nu)\kappa(\nu)\rho(T,\nu) \tag{3.19}$$

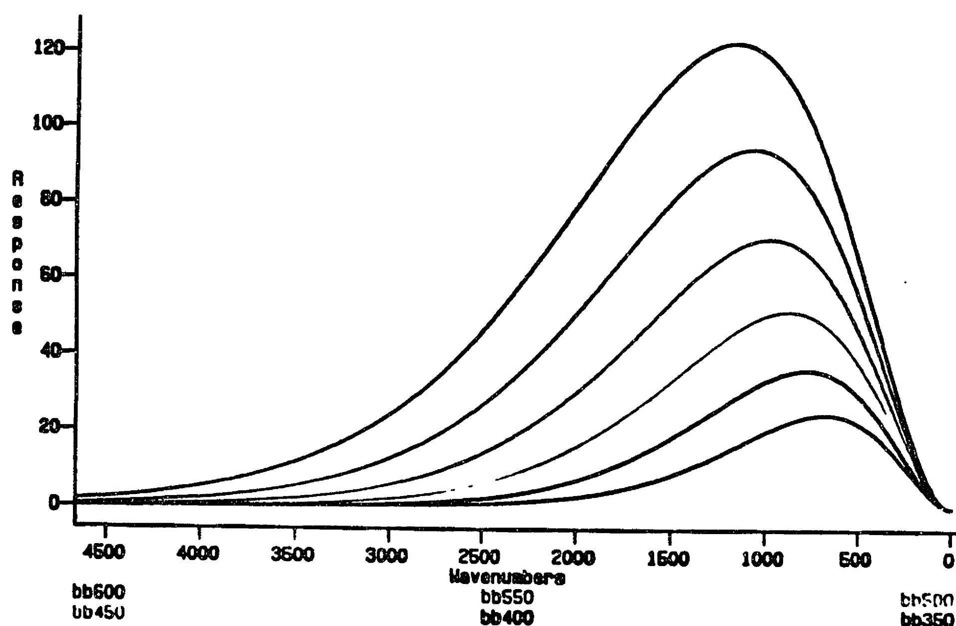

Figure 3.3: Calculated blackbody radiation spectra from Planck's radiation law.

where n is the refractive index of the sample. Clearly, the radiation intensity is directly proportional to the absorption coefficient.

The emittance of the sample can be obtained by the ratio of its emission profile versus that of a blackbody. Since the radiation collected by the detector is comprised of contributions from the surrounding media and from the spectrometer itself, spectral compensation is required to acquire the emission spectrum solely due to the sample. This correction becomes extremely important when attempting to acquire spectra of samples at temperatures near room temperature or samples exhibiting low emissivity. Calculation of the corrected emittance (ϵ) is accomplished according to Eq.(3) [63] :

$$\epsilon(T) = \frac{\rho_s - \rho_{bg}}{\rho_{bb} - \rho_{bg}} \tag{3.20}$$

Where ρ_s is the emission spectrum of the sample, ρ_{bb} is the reference blackbody radiation spectrum, and ρ_{bg} is the background emission spectrum from the

surroundings.

The details of thermal radiation measurement by E/FT-IR is described in Chapter 7. The emission spectrum for a heavily doped (0.004-0.005 Ω-cm) substrate resembles that of a blackbody. One reason for this is that when a substrate is heavily doped, there are numerous free carriers (on the order of 10^{19} cm^{-3} in this substrate). Since these carriers are not bound, no associated resonance exists; therefore, only a broad band absorption with a subsequent broad band emission is observed. The strong absorption and re-emission from these carriers dominate the emission spectrum. Furthermore, the vibrational bands corresponding to lattice phonons and impurity molecules are not observable.

The spectrum for a lightly doped (10-20 Ω -cm) substrate where the dopant concentration is on the order of 10^{15} cm^{-3}, exhibits less free carrier effect than the heavily doped sample. The energy is absorbed partially by lattice phonons and partially by free carriers; consequently, re-emission by these phonons appears at some well defined resonance frequencies, and the re-emission from the free carriers simply contribute to the broad band spectral offset. The *in-situ* infrared emission spectrum of the lightly doped silicon wafer is very similar to its *ex situ* transmission spectrum at room temperature, although the spectrum is inverted. This similarity makes possible the analysis of E/FT-IR spectra by using existing spectral libraries. The silicon lattice phonon bands are observed at 609cm^{-1}, 736 cm^{-1}, and 885 cm^{-1}, in addition to bands associated with impurities (Si-O) at 1102 cm^{-1}. By performing a complete spectral analysis such as this [64], the oxygen concentration within the bulk of the silicon substrate can be found from the E/FT-IR data.

We have also measured the emittance of a heavily doped substrate with a lightly doped epi-layer. The overall spectrum consists of contributions from the substrate emission, the epi-film emission, and re-absorption of the subtracted emission by the overlaying epi-film. For simplicity, we neglect here the emission and absorp-

tion within the lightly doped epitaxial silicon film, and consider only the emission from the substrate. At the substrate/epi-film interface, part of the radiation from the substrate is reflected and part is transmitted. The part that is transmitted will travel through the epi-film reaching the epi-film/air interface where part of the radiation is emitted and part of it is reflected. When the reflected beam arrives at the epi-film/substrate interface, another reflection takes place, and the reflected beam will again travel through the epi-film and emit at the surface of the film. These two emitted beams interfere with each other, causing the appearance of a cosine wave (interference pattern) superimposed upon the emission spectrum. They are exactly $2dn_f\cos\Theta$ out of phase, where d is the film thickness, n_f is the film refractive index, and Θ is the angle of emission from the surface norm. A detailed theoretical treatment of epi-film thickness measurements by R/FT-IR and E/FT-IR will be given in the next section.

In summary, the experimental measurement of thermal radiation using E/FT-IR confirms that radiation intensity of silicon is indeed directly proportional to its absorption coefficient. For film thickness measurement using E/FT-IR, the heavily doped substrate is the source of IR emission. When the substrate is lightly doped, E/FT-IR can be used to identify impurities and measure their concentrations.

3.5 Epi-film Thickness Measurements by R/FT-IR and E/FT-IR

Using the simple model for the Michelson Interferometer derived in section 1, the interferogram of a single layer of film on a substrate resulting from IR reflection or emission will be derived next.

A lightly doped film with refractive index n_1, and a thickness d, on a heavily

doped substrate with refractive index n_2, is selected for the thickness measurement. For simplicity, we will neglect the multiple reflections in the film.

In room temperature reflection mode, an external source $I(k)$ strikes the surface of the film. At the ambient-film interface, part of this beam is reflected as beam E_{A_r}, while the remainder is transmitted into the film, traverses the film, then it is reflected at the substrate-film interface, and finally, emerges from the film as beam E_{B_r} (as shown in Figure 3.4(a)).

In the emission mode, the wafer is kept at an elevated temperature (T). IR radiation is emitted by the heavily doped substrate (as proved experimentally in the last section). It travels through the film, and arrives at the surface. At the film-ambient interface, part of the beam is emitted as beam E_{A_e}, while the remainder is reflected towards the substrate. The reflected beam traverses the film and once again reflected by the film-substrate interface, then emerges from the film as beam E_{B_e}. A ray tracing diagram for the emission mode is shown in Figure 3.4(b).

Therefore, the light entering the Michelson Interferometer can be decomposed as:

$$E_r(k) = E_{A_r}(k) + E_{B_r}(k) \tag{3.21}$$

$$E_e(k) = E_{A_e}(k) + E_{B_e}(k) \tag{3.22}$$

where the subscripts r, e denote reflection mode and emission mode, respectively. Moreover, the Fresnel reflection coefficient for normal incidence from substance l (with refractive n_l) to substance m (with refractive n_m) is [65] :

$$R_{l,m}(k) = \frac{n_m(k) - n_l(k)}{n_m(k) + n_l(k)} \tag{3.23}$$

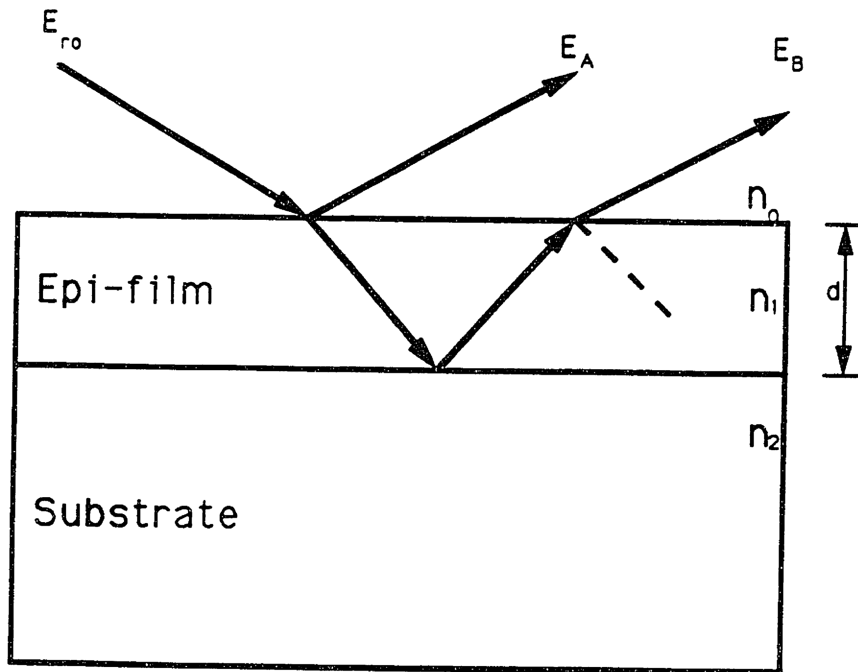

(a)

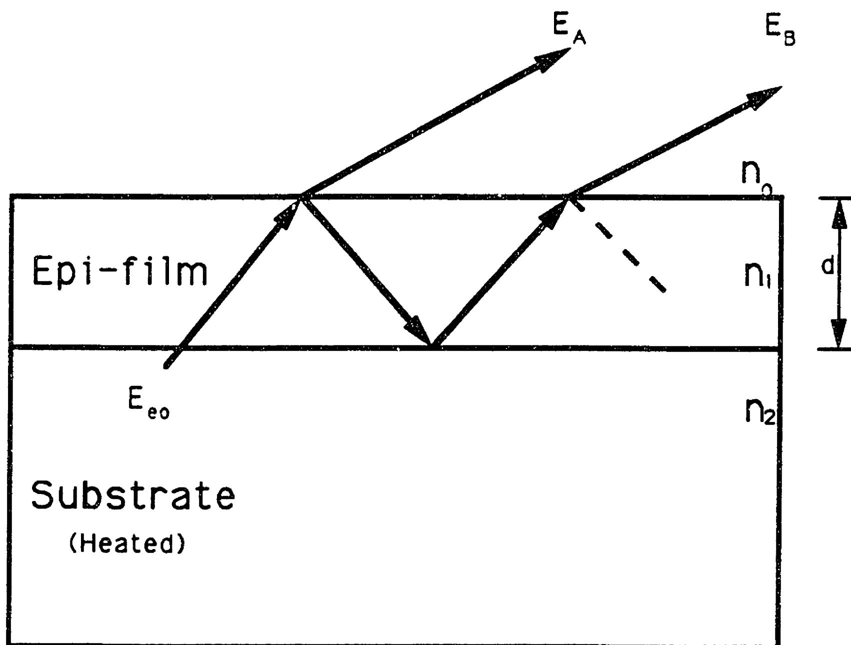

(b)

Figure 3.4: Comparison of (a) infrared reflection and (b) infrared emission ray-tracing diagram from a substrate and an epilayer for film thickness measurements.

and the corresponding Fresnel coefficient for transmission is:

$$T_{l,m}(k) = \frac{2n_m(k)}{n_l(k) + n_m(k)} \tag{3.24}$$

Futhermore, we can express E_B and E_A in terms of the incident light E_o using those Fresnel reflection and transmission coefficients:

$$E_{A_r} = R_{0,1}E_{ro} \tag{3.25}$$

$$E_{B_r} = T_{0,1}R_{1,2}T_{1,0}e^{-\alpha\Delta - jk\Delta}E_{ro} \tag{3.26}$$

where α is the absorption coefficient; $\Delta = 2dn_1\cos\Theta$; $R_{l,m}$ and $T_{l,m}$ are the Fresnel reflection and transmission coefficients, respectively.

$$E_r(k) = R_{0,1}E_{ro} + T_{0,1}R_{1,2}T_{1,0}e^{-\alpha\Delta - jk\Delta}E_{ro} \tag{3.27}$$

In order to use the linear system model derived earlier, we want to calculate intensity (I_r) using Equation(3.27) and Equation(3.9). The result is:

$$I_r(k) = I_{A_r} + I_{B_r} + 2\sqrt{I_{A_r}I_{B_r}}\cos k\Delta \tag{3.28}$$

where

$$I_{A_r} = \langle E_{A_r} \bullet E_{A_r}^* \rangle = R_{0,1}^2 I_{ro} \tag{3.29}$$

$$I_{B_r} = \langle E_{B_r} \bullet E_{B_r}^* \rangle = T_{0,1}^2 R_{1,2}^2 T_{1,0}^2 e^{-2\alpha\Delta} I_{ro} \tag{3.30}$$

The purpose here is to understand the principle of the FT-IR thickness measurement technique. Our focus is on the phase difference of the light beams. The

magnitude depends on the absorption coefficient and the refractive index (n) of the materials. However, these properties are a complex function of temperature, dopant concentration of the film, and substrate, etc. which will not be considered here. In addition, there is a constant phase shift at each interface which will also contribute to its magnitude. A more comprehensive model that takes into account all these factors will be introduced later. For simplicity, we can rewrite equation (3.28) using C_1 and C_2 as constants:

$$I_r(k) = C_{1r}I_{ro}(k) + C_{2r}I_{ro}(k) + 2\sqrt{C_{1r}C_{2r}I_{ro}(k)}\cos k\Delta \tag{3.31}$$

For the emission mode:

$$E_e(k) = T_{2,1}T_{1,0}e^{-0.5\alpha\Delta - j0.5k\Delta}E_{eo} + T_{2,1}R_{1,0}R_{1,2}T_{1,0}e^{-1.5\alpha\Delta - j1.5k\Delta}E_{eo} \tag{3.32}$$

Similarly we can calculate the intensity using Equation(3.32) and Equation(3.9) which yields:

$$I_e(k) = I_{A_e} + I_{B_e} - 2\sqrt{I_{A_e}I_{B_e}}\cos k\Delta \tag{3.33}$$

where

$$I_{A_e} = T_{2,1}^2 T_{1,0}^2 e^{-\alpha\Delta} I_{eo} \tag{3.34}$$

$$I_{B_e} = T_{2,1}^2 R_{1,0}^2 R_{1,2}^2 T_{1,0}^2 e^{-3\alpha\Delta} I_{eo} \tag{3.35}$$

Notice the "-" sign in equation(3.33), because n_0 is less than n_1, $R_{1,0}$ is negative.

Following the same procedures as in reflection mode, we can obtain an expression for the emission mode:

$$I_e(k) = C_{1e}I_{eo}(k) + C_{2e}I_{eo}(k) - 2\sqrt{C_{1e}C_{2e}}I_{eo}(k)\cos k\Delta \tag{3.36}$$

Now, we can simply treat $I_r(k)$ (Eq.(3.31)) or $I_e(k)$ (Eq.(3.36)) as an input to our linear system model to find the corresponding reflection or emission interferogram. The interferogram for reflection can be expressed as:

$$\begin{aligned} i_r(x) &= \sum_k I_r(k)H(k) \\ &= Constant + \int_{-\infty}^{+\infty} C_{1r}I_{ro}(k)\cos kx dk + \int_{-\infty}^{+\infty} C_{2r}I_{ro}(k)\cos kx dk \\ &+ \int_{-\infty}^{+\infty} \sqrt{C_{1r}C_{2r}}I_{ro}(k)\cos k\Delta \cos kx dk \\ &= Const. + C_{1r}i_{ro}(x) + C_{2r}i_{ro}(x) + C_{3r}i_{ro}(x-\Delta) + C_{3r}i_{ro}(x+\Delta) \end{aligned} \tag{3.37}$$

where $C_{3r} = \frac{1}{2\pi}\sqrt{C_{1r}C_{2r}}$

Similarly, for the emission mode:

$$i_e(x) = Constant + C_{1e}i_{eo}(x) + C_{2e}i_{eo}(x) - C_{3e}i_{eo}(x-\Delta) - C_{3e}i_{eo}(x+\Delta) \tag{3.38}$$

where $C_{3e} = \frac{1}{2\pi}\sqrt{C_{1e}C_{2e}}$

Now we have found the expressions for the interferograms. The constant term is a DC offset which can be ignored. The second and the third terms are just inverse Fourier transforms of $I_o(k)$ multiplying some constants, then the sum of the two is named as our center burst. The last two terms come from an inverse Fourier transform of $I_o(k)$ convolved with the inverse Fourier transform of a cosine function. The convolution yielding two side bursts. Figure 3.5(a) is a typical experimental interferogram measured using the Michelson interferometer. The experimental results

agree with our theoretical calculations: there is one center burst plus two side bursts in an interferogram. Figure 3.5(b) is a comparison of an interferogram measured in the reflection mode, with an interferogram measured in the emission mode. The side bursts of the emission mode look like those of the reflection mode, except that they are phase shifted by 180°. This is expected because the sign change in equation(37) and equation(38) introduces the phase change. However, the locations of the side bursts for both emission and reflection mode are the same. This indicates that the film thickness measurements using either reflection or emission FT-IR yields the same results. This has been confirmed for film thickness measurements from 1 μm to 20μm [66].

Film thickness can also be obtained from the reflection or emission spectrum in k-space by taking a mathematical Fourier transform of the interferogram. A typical measured reflection spectrum is shown in Figure 4.9, and an emission spectrum is shown in Figure 7.4. Although film thickness measurement can be obtained either from the interferogram or the IR spectrum, we often use the interferogram. There are several advantages for using interferogram: 1) it is relatively easy to locate the peak by a computer (it comes with the Digilab FT-IR software package), in contrast, curve fitting must be used when using the spectrum; 2) the interferogram is directly measured by the FT-IR spectrometer; no computation is required, therefore time for taking the fourier transformation is saved. In addition, the digital fast Fourier transformation may introduce noise or error in the spectrum. Consequently, all our real-time *in-situ* film thickness measurements by E/FT-IR use the interferogram.

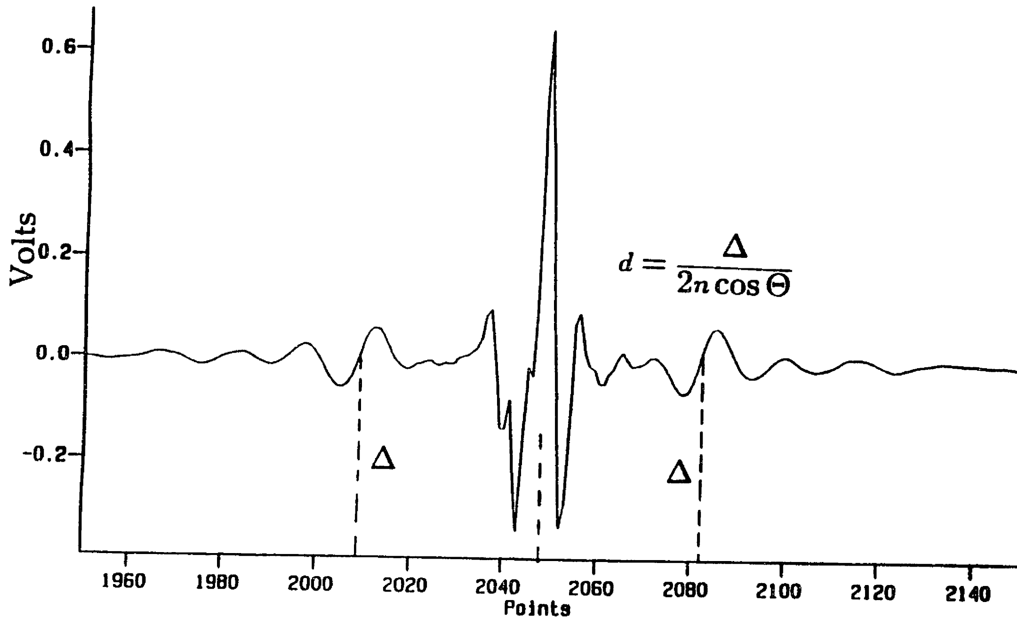

(a)

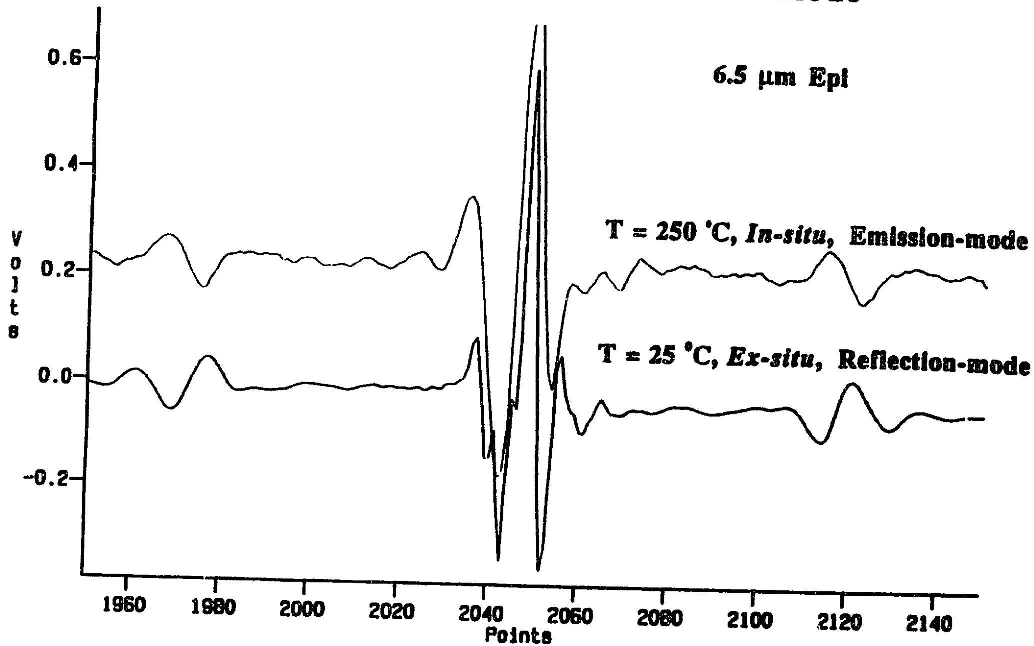

(b)

Figure 3.5: (a) A typical measured FT-IR interferogram of a lightly doped epi-layer on a heavily doped substrate, (b) Comparison of experimentally measured R/FT-IR and E/FT-IR interferograms.

Chapter 4

Refractive Index of Silicon

4.1 Introduction

Epitaxial silicon films are the building materials for DRAM, MOS, and BJT devices. The epitaxial film thickness is a critical parameter that must be accurately measured and controlled. For example, it is necessary to ensure that outdiffusion and autodoping during device processing do not consume the entire epitaxial film. In addition, several bipolar transistor device parameters, such as breakdown voltage, junction capacitance, transistor gain, and high frequency performance, depend on the epi-layer thickness. CMOS latch-up, breakdown voltage, snap-back voltage, and drive-in time are also related to the epi-layer thickness. For epi film thickness measurements, Fourier transform infrared (FT-IR) instruments are widely used in the semiconductor industry [67] [66]. There are many commercially available FTIR instruments which are nondestructive, fast and automatic [67]. Most of these instruments have very good repeatability, reproducibility, and high precision (~0.01 μm). However, the accuracies of the FTIR instruments are questionable and they carry a minimum thickness limitation (~ 0.3 μm). Over the past three decades, many investigators have studied

issues of phase shift, due to the reflection from air-film and film-substrate interfaces, and the infuence of the phase shift on the accuracy of epi-film thickness measurement [68] [69]. Severin [68] concluded that the accuracy of FT-IR measurements can be obtained only by calibration.

Currently, in addition to the phase shift, epi-film thickness measurements using an FT-IR assume a constant refractive index for the epitaxial silicon film. However, the refractive index of silicon is a complex function of temperature, dopant concentration, and wavelength. The interferogram as measured by FT-IR instrument has included all these variations. If one can decouple the effect of changing refractive index, less calibration and better accuracy in epi-film thickness measurements may be achieved. This chapter presents the procedures and results of experimental refractive index measurements, then a theoretical analysis is performed to examine the effect of refractive index dispersion on epi-film thickness measurement.

Using an FT-IR spectrometer, we measured silicon reflectance as a function of dopant concentration, temperature, and wavelength. The refractive index is then calculated from the reflectance measurement. Using the theory and model which were developed in [70], and assuming a constant refractive index or using the measured refractive indexes, we can calculate the resulting interferogram. By comparing the outcome of our theoretical calculation using a constant epi-film refractive index, with the outcome that uses the experimentally measured refractive index, we can clearly see the effect of refractive index on the calculated interferogram. Our results show that the spectral dispersion of the refractive index cannot be neglected for epi-film thickness measurement. Furthermore, when the measurement is done in real-time *in-situ* mode, the temperature dependence of the sample optical properties must also be taken into account for the thickness measurement.

4.2 Experimental - Reflectance Measurements

The high-temperature optical properties of the film and substrate are measured using a Digilab 60A Fourier transform infrared (FT-IR) spectrometer and a high-temperature sample holder. The spectrometer, shown schematically in [71], possesses a wavelength range from 2.5 μm to 25 μm, and is equipped with a specially designed high-temperature sample holder. It uses a room temperature DTGS (deuterate triglycine sulfate) detector, and a wide band glow bar IR source. The special high temperature sample holder is installed in the sample compartment of the spectrometer.

The schematic of the high-temperature sample holder is shown in Fig.4.1. Two cartridge heaters embedded in the copper block are used to heat the sample from room temperature to 800 K. The sample temperature is monitored by a thermocouple attached to the copper block close to the sample. The pressure inside the sample compartment is kept below 1 mTorr to reduce the heat loss to the wall by conduction and convection, and to avoid oxidation of the sample during measurements. The beam from the IR source is reflected by an elliptical mirror, and focused on the sample surface through a hemispherical window. The hemispherical window made of KRS-5 (Thallium Bromoiodide) is used to seal the sample compartment. The window is heated by radiation during measurement, and the transmittance of the window changes with temperature. When the sample reflectance is measured at different temperatures, the measurements are influenced by the window transmittance. The window effects must be taken into account when interpreting the measured sample reflectance. The sample temperature can be kept at a constant temperature up to 800 K during each measurement. For each spectrum, 2000 scans with 4 cm^{-1} resolution are collected and an average is taken to reduce the noise effects.

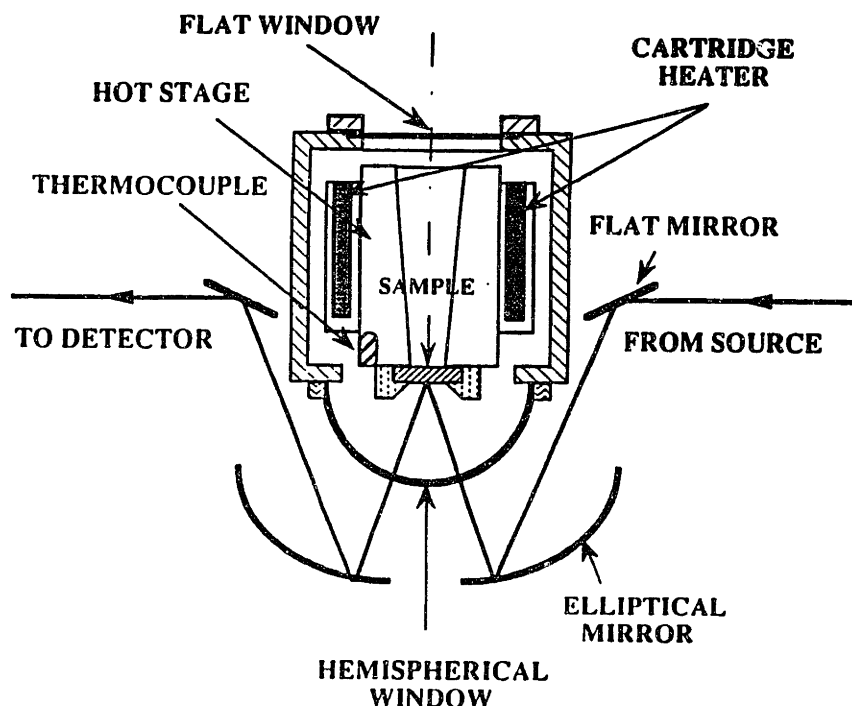

Figure 4.1: Schematic of the high temperature sample holder.

4.3 Data Analysis

Calculation of Reflectance

The measured spectrum is influenced by the system characteristics of the FT-IR spectrometer. As the beam propagates from the source to the detector, its intensity is modified by the window transmission and the sample reflection. The final spectrum is also affected by the detector responsivity. When the sample temperature is increased, the window and detector characteristics also change due to the temperature variation. The window temperature is observed to be 333 K when the sample temperature is 800 K. The temperature-induced transmittance variation of the KRS-5 window must be compensated for. Considering the system variations with temperature, the measured spectrum can be expressed by

$$S_s(T) = CT_w(T)R_s(T)Q_d(T) \tag{4.1}$$

where T_w is the hemispherical window transmittance, R_s is the substrate reflectance, and Q_d is the detector responsivity. The constant C is only dependent on the source power and is assumed to be independent of the sample temperature. The ratio of the high-temperature and room-temperature spectra is

$$\frac{S_s(T)}{S_s(300K)} = \frac{T_w(T)}{T_w(300)} \frac{Q_d(T)}{Q_d(300K)} \frac{R_s(T)}{R_s(300K)} \tag{4.2}$$

The first two terms of the right hand side must be known in order to determine the sample reflectance, $R_s(T)$. Using a gold reference mirror, the ratio of spectra is measured, which is given as

$$\frac{S_r(T)}{S_r(300K)} = \frac{T_w(T)}{T_w(300)} \frac{Q_d(T)}{Q_d(300K)} \frac{R_r(T)}{R_r(300K)} \tag{4.3}$$

where the subscript, r, denotes the property of the gold reference mirror. The reflectance of metals can be predicted by the Drude model [72]. If the Drude model is used to predict the gold reflectivity at the wavelength of 10 μm, Rr is 0.996 at 300 K, and 0.989 at 800 K. If this small variation is neglected, the sample reflectance at temperature T is obtained from equations (4.2) and (4.3),

$$R_s(T) = R_s(300K) \frac{S_s(T)}{S_s(300K)} \frac{S_r(300K)}{S_r(T)} \tag{4.4}$$

Both reflectances of the bare substrate and the film-substrate composite at high temperatures are measured in this way.

Calculation of refractive index

The reflectance at normal incident for a single reflection is a function of refractive index n and the absorption (or extinction) coefficient κ:

$$R = \frac{(n-1)^2 + \kappa^2}{(n+1)^2 + \kappa^2} \tag{4.5}$$

The relationship between the dielectric constant and the optical constants is given by:

$$\epsilon = n^2 - \kappa^2 \tag{4.6}$$

On the long wavelength side of the intrinsic absorption edge, there exists a frequency region where $(n-1)^2 \gg \kappa^2$. Consequently, from equation (4.5) and (4.6), the real part of the dielectric constant in this region can be approximated by:

$$\epsilon = (\frac{1+\sqrt{R}}{1-\sqrt{R}})^2 \tag{4.7}$$

Solving equation (4.5) and (4.6) for n and κ in this region, we get [73] :

$$n = \frac{1}{2}[(\frac{(1+R)}{1-R}) + \sqrt{(\frac{1+R}{1-R})^2 + 2(\epsilon - 1)}] \tag{4.8}$$

Using equation (4.7) and (4.8), refractive index of silicon can be calculated from the IR reflectance data.

4.4 Reflective Index of Silicon as a Function of Wavelength, Sample Temperature, and Dopant Concentration

4.4.1 Experimental Results

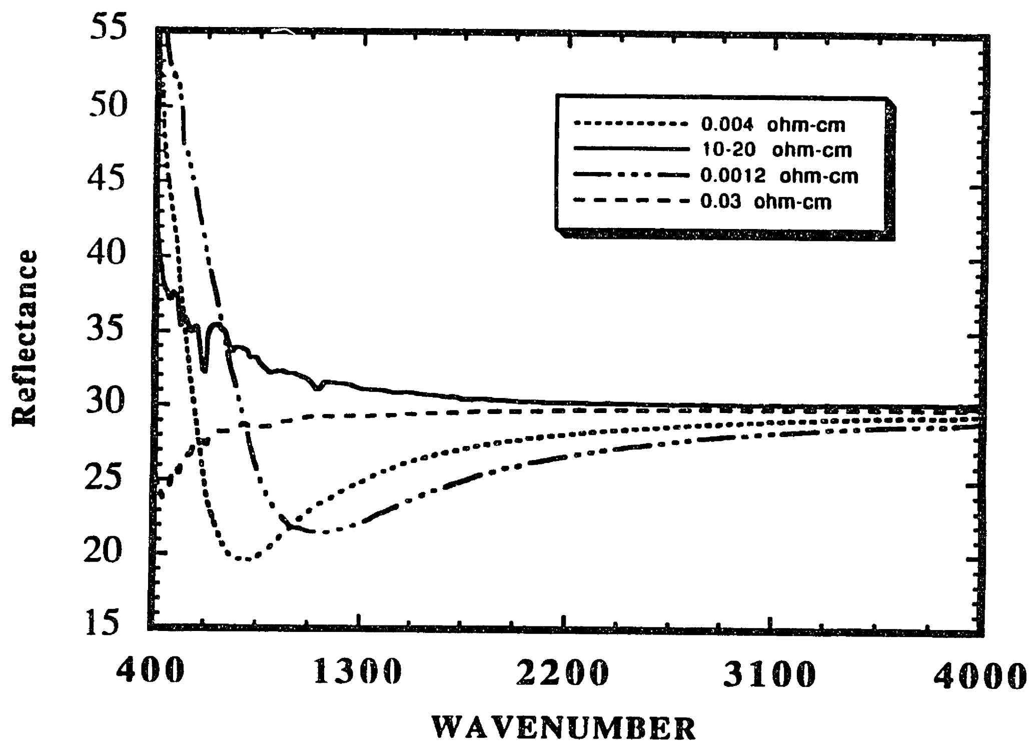

Figure 4.2: IR reflectance of several silicon samples with different resistivity.

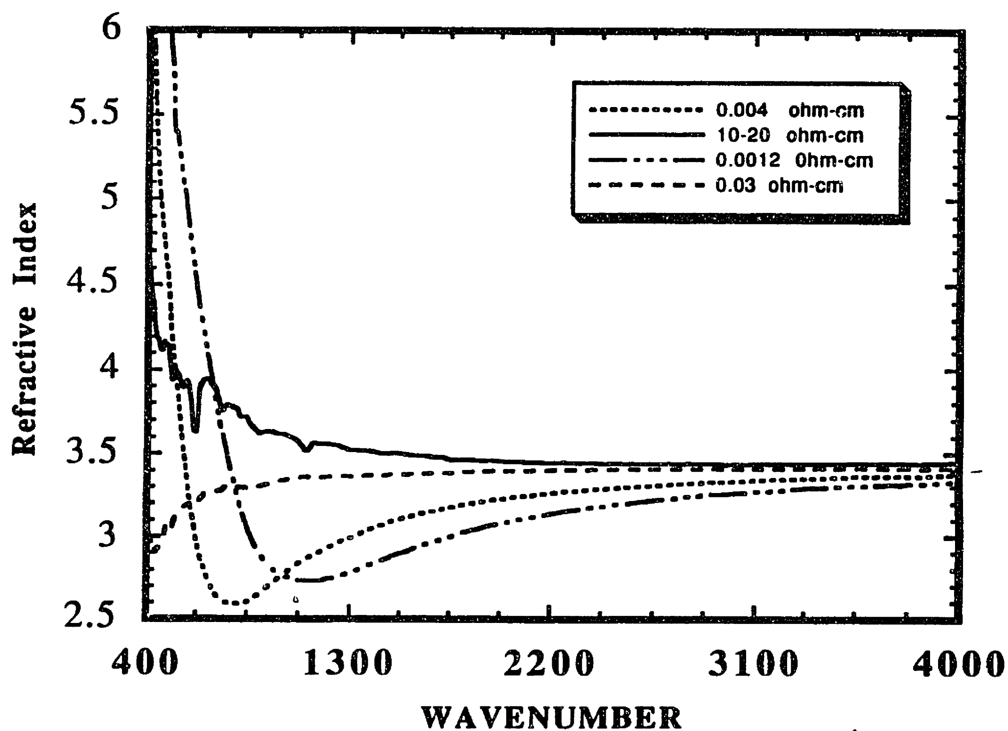

Figure 4.3: Refractive index calculated from the corresponding reflectance data shown above.

Room temperature reflectance measurements were performed. Figure 4.2 shows the wavelength dependence of the silicon samples' reflectance with resistivity of 0.001, 0.004, 0.03, and 15 $\Omega - cm$ (values obtained from spreading sheet resistance profile measurement) as indicated on the figure. Figure 4.3 shows the calculated refractive index using equations (4.7) and (4.8) from the measured reflectance data shown in Figure 4.2 directly without any adjustment. The refractive index of a lightly doped sample is nearly independent of wavelength, dispersion occurs only at lower wavenumber side of the spectra. The magnitude of the refractive index obtained this way are in close agreement with the nominal refractive index of silicon ($n = 3.42$). However, the refractive index of a heavily doped sample is a strong function of wavelength. The reflectance minima is the result of free carrier absorption also known as plasma absorption. The location of the minima (or plasma absorption frequency) can be calculated using equation (4.14).

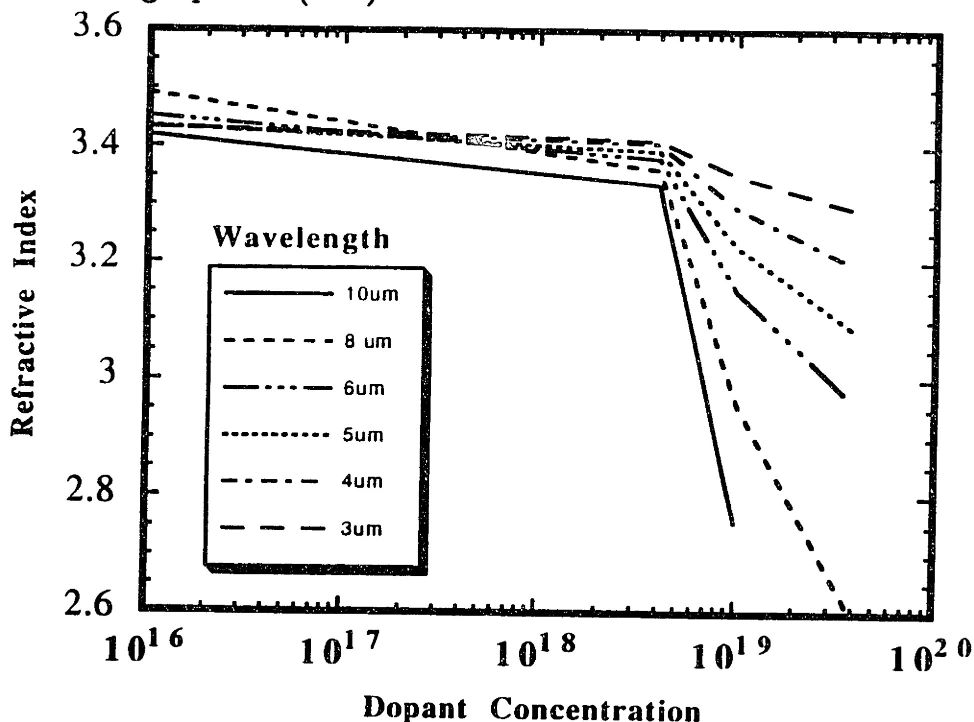

Figure 4.4: Refractive index of silicon as a function of dopant concentration for several wavelengths.

Figure 4.4 shows the refractive index of silicon as a function of dopant concen-

tration for several wavelengths. Clearly, as the wavelength increases, the functional dependence of refractive index on dopant concentration becomes stronger. This is because the free carrier absorption has a bigger effect on the longer wavelength side of the infrared spectrum. On the other hand, at the shorter wavelength side, the dominant absorption is the band to band absorption. Our measurement data agree with that in Sze [123]. The refractive index of lightly doped silicon (with dopant concentration below 10^{18} cm^{-3}) is relatively constant. However, for heavily doped silicon (with dopant concentration above $10^{18}cm^{-3}$), its refractive index depends strongly on the dopant concentration.

Figure 4.5(b) and Figure 4.6(b) show the temperature dependence of the refractive index calculated from the reflectance measurement 4.5(a) and Figure 4.6(a). The sample in Figure 4.5 is n-type with 0.004-0.005 Ω-cm resistivity as determined using SRP. The sample in Figure 4.6 is p-type with 0.03 Ω-cm resistivity as determined using spreading sheet resistance probe (SRP). For each spectrum, the sample temperature was fixed at a temperature of 473, 573, 673, 713, 733, 753, and 773 K while the reflectance spectrum was taken. The reflectance spectra were compensated using equation (4.4) to remove the effect of the instrument. Figure 4.5(b) and Fig. 4.6(b) were then calculated using equations (4.7) and (4.8) from those compensated reflectance spectra 4.5(a) and Fig. 4.6(a). From Figure 4.5(b) and Fig.4.6(b), we observe that refractive index of silicon is inversely proportional to temperature at the long wavelength side of the spectrum. We believe that the temperature dependence of free carrier absorption is the dominating factor, although more detailed experimental and theoretical studies must be performed to analyze this carefully.

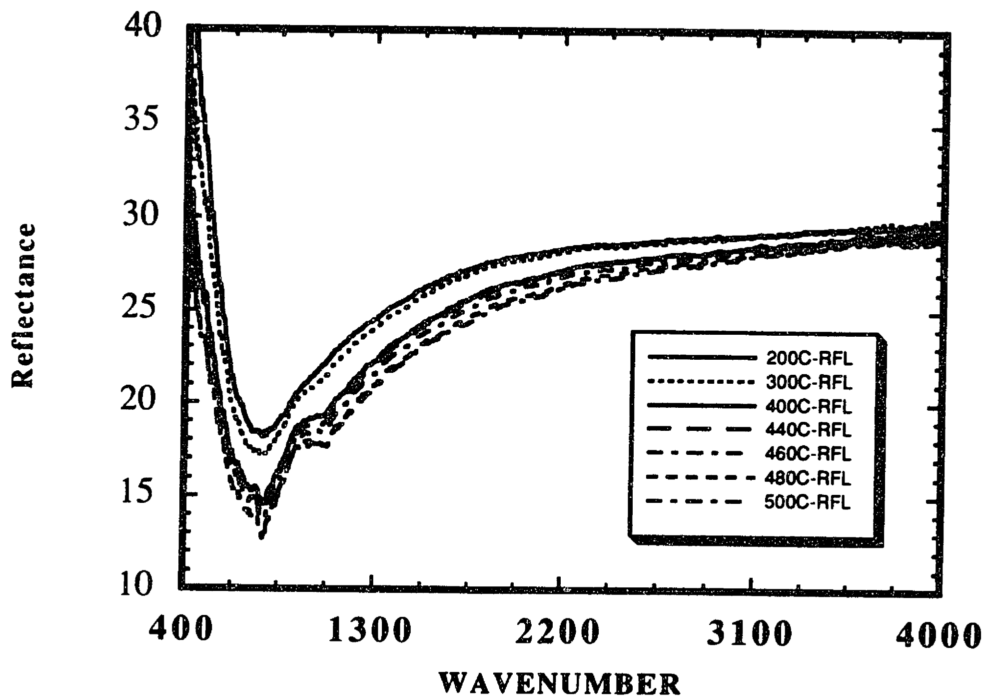

(a)

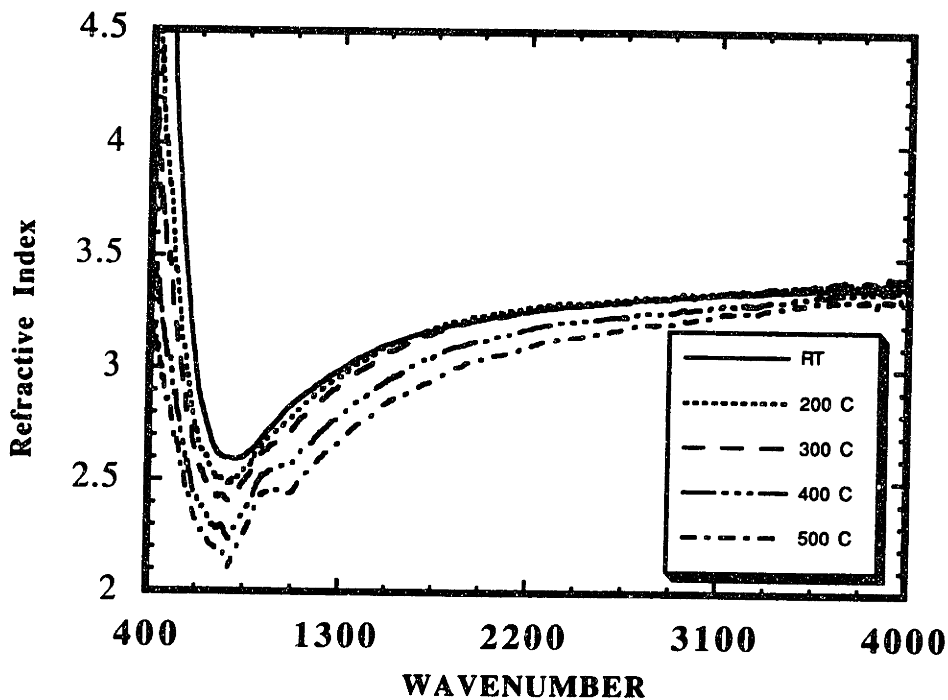

(b)

Figure 4.5: Temperature dependence of (a) the reflectance measurements, (b) the refractive index calculated from the reflectance data for a n-type sample with 0.004-0.005 Ω-cm resistivity.

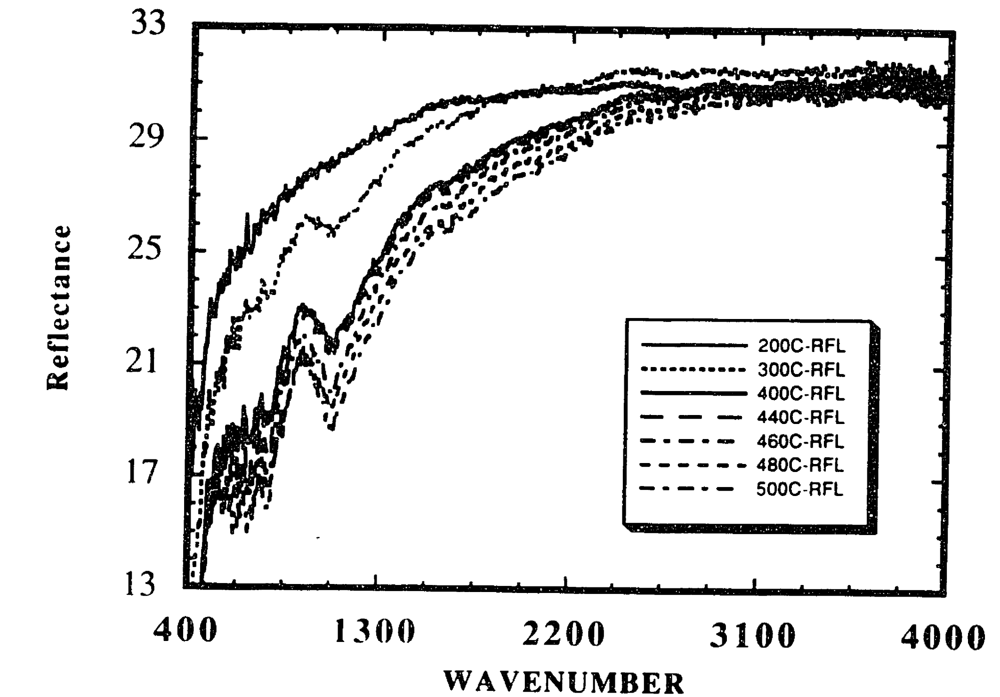

(a)

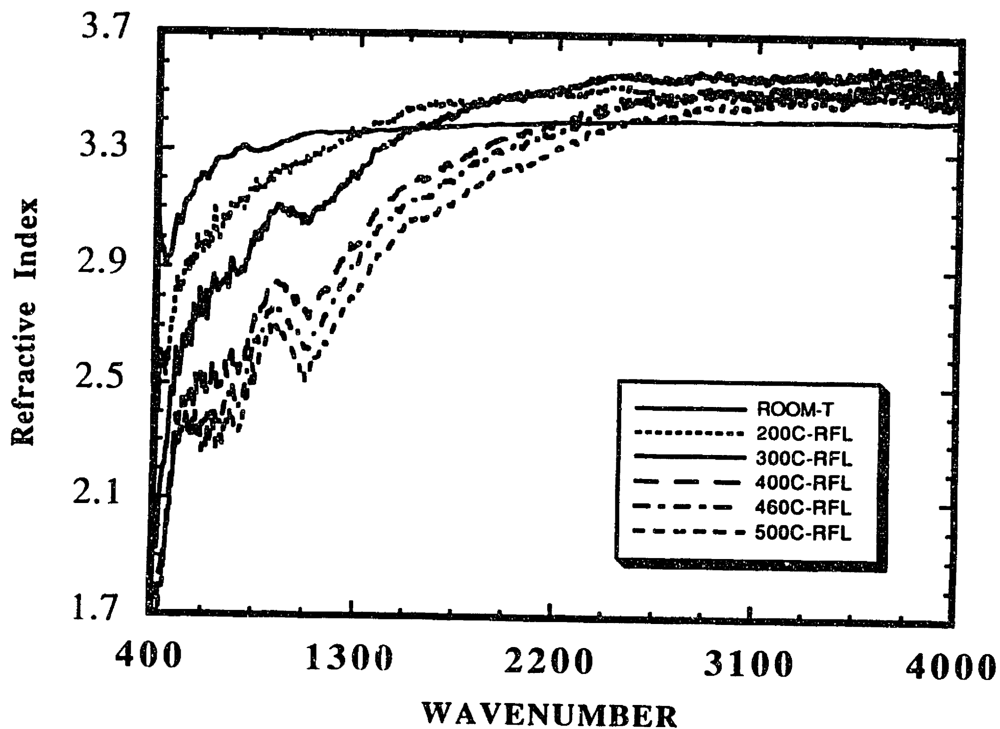

(b)

Figure 4.6: Temperature dependence of (a) the reflectance measurements, (b) the refractive index calculated from the reflectance data for a p-type sample with 0.03 Ω-cm resistivity.

4.4.2 Effect of Dopant Concentration

From classical dispersion theory of solid, the solid is considered as an assembly of oscillators. The solution of the equation of motion giving that [62]:

$$n^2 - k^2 - \epsilon^* = \frac{Ne^2}{m^* \epsilon_o} \frac{\omega_o^2 - \omega^2}{(\omega_o^2 - \omega^2)^2 + \omega^2 g^2} \tag{4.9}$$

$$2nk\omega = \frac{Ne^2}{m^* \epsilon_o} \frac{g\omega}{(\omega_o^2 - \omega^2)^2 + \omega^2 g^2} \tag{4.10}$$

where $\epsilon^* = 1$ when dealing with the fundamental electronic absorption band and $\epsilon^* = n_o^2$ (where n_o is the constant refractive index at wavelengths well above the absorption edge) when dealing with an infrared absorption band; ω_o is the resonant frequency of the oscillator; N is the dopant concentration; e is the electronics charge; m^* is the effective mass; and the damping coefficient (g) is:

$$g = \frac{e}{m^* \mu} \tag{4.11}$$

Assuming a heavily doped semiconductor behaves like a metal, absorption is dominated by free electrons at long wavelengths. In this case, we can use the free electron approximation, where $\omega_o = 0$ since electrons were not bound. The simplified equation is given as:

$$n^2 - k^2 - \epsilon^* = -\frac{\epsilon^* \omega_p^2}{\omega^2 + g^2} \tag{4.12}$$

$$2nk\omega = \frac{\epsilon^* g \omega_p^2}{\omega^2 + g^2} \tag{4.13}$$

where the plasma frequency (ω_p) can be calculated by:

$$\omega_p = \sqrt{\frac{Ne^2}{\epsilon^* \epsilon_o m^*}} \tag{4.14}$$

As expected from theory, the reflection minima moves toward higher wavenumber as the sample resistivity decreases.

Solving the two equations, we found that:

$$n^2 = \frac{\epsilon^*}{2}[(1 - \frac{\omega_p^2}{\omega^2 + g^2}) \pm \sqrt{(1 - \frac{\omega_p^2}{\omega^2 + g^2})^2 + (\frac{g\omega_p^2}{\omega(\omega^2 + g^2)})^2}] \tag{4.15}$$

Figure 4.7 shows the simulated results. The parameters used in the calculation are as follows: e=1.6x10^{-19}C ; c=3x10^8 m/s; m_o=9.11x10^{-31} kg; ϵ_o=8.85x10^{-12} F/m; ϵ^*=11.8.

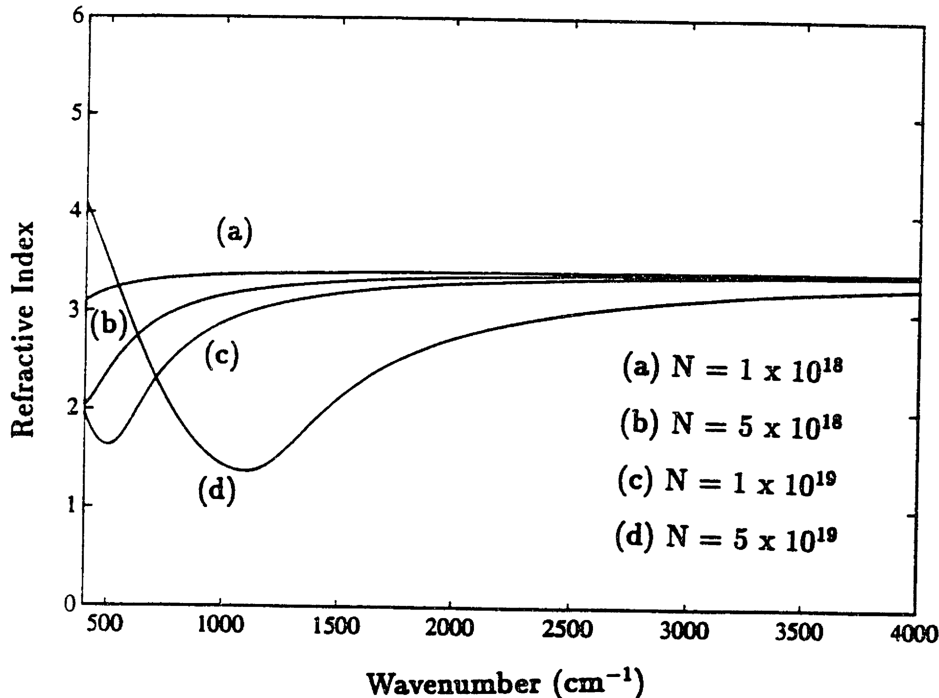

Figure 4.7: Calculated refractive index of silicon as a function of dopant concentration and wavelength.

The effective mass for electron [75]:

$$m_n^* = \frac{3}{\frac{1}{m_l} + \frac{2}{m_t}} \tag{4.16}$$

where m_t=0.19 m_o; m_l=0.98 m_o [76];

The effective mass for hole [75] [77]:

$$m_p^* = \frac{m_{lh}^{3/2} + m_{hh}^{3/2}}{m_{lh}^{1/2} + m_{hh}^{1/2}} \tag{4.17}$$

where m_{lh}=0.16 m_o; m_{hh}=0.49 m_o [76];

In general, the calculated refractive index of silicon as a function of dopant concentration qualitatively agrees with that observed through our experimental measurements. Using the same constants, Figure 4.8 shows a comparison of the calculated refractive index with the experimentally measured refractive index. The sample was n-type with dopant concentration of 2x10^{19} cm^{-3} as determined by SRP. In our calculation, first, N was adjusted to match the reflectance minimum, then mobility μ was adjusted to match the magnitude of the refractive index around the reflectance minimum. The calculated refractive index using N = 2.5x10^{19} cm^{-3} and μ=45 cm^2/V-s was shown in Figure 4.8.

4.4.3 Effect of Temperature

Refractive index is a critical optical parameter for optical measurements. The trend in process integration and the use of cluster tools [78] generated the need to perform real-time and *in-situ* measurements at process temperatures [66]. In this section, we will investigate the temperature dependence of refractive index of silicon.

As pointed out earlier, free carrier absorption has a bigger effect on the longer wavelength side of the infrared spectrum. On the other hand, at the shorter wavelength side, the dominant absorption is the band to band absorption. In this extreme,

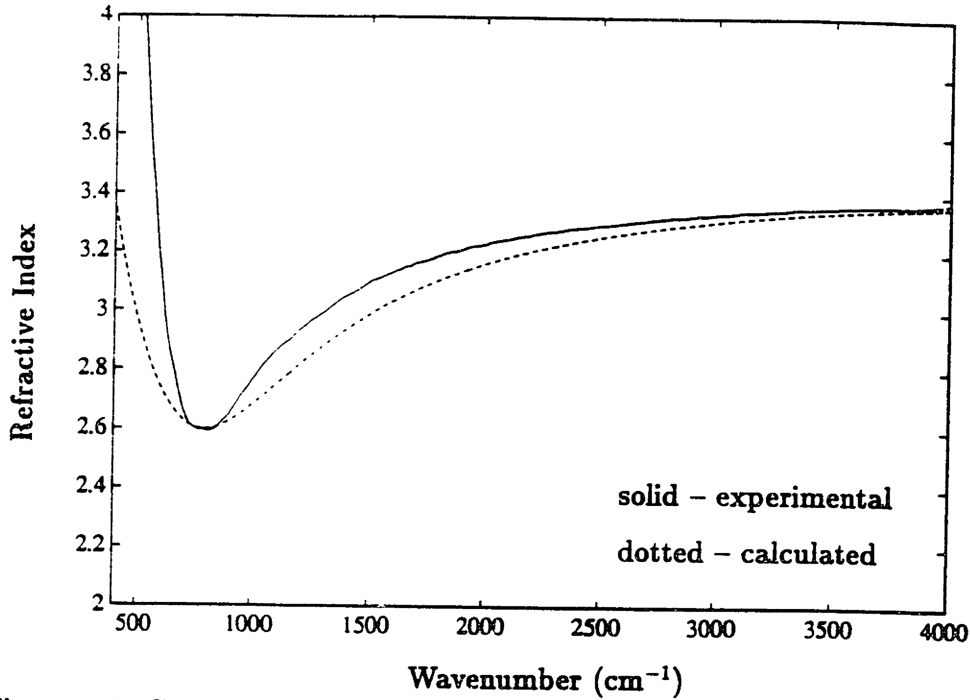

Figure 4.8: Comparison of calculated and measured refractive index of silicon.

the refractive index variation is dictated by the band-gap temperature dependence as was indeed observed by Lukes in [79] for only two wavelengths 1.5 and 1.3 μm. He did a theoretical analysis leading to an expression for temperature dependence of the refractive index (for short wavelengths, e.g. 1.5 and 1.3 μm) [79]:

$$\frac{dn}{dT} = -\frac{n^2-1}{2n}\beta - \frac{1}{n}\frac{Ne^2}{\pi m}\frac{\omega_o}{(\omega_o^2-\omega^2)^2}\frac{d\omega_o}{dT} \tag{4.18}$$

where β is the thermal expansion coefficient of silicon. From the above equation, we see that: $\frac{dn}{dT} \propto -\frac{d\omega_o}{dT}$. For semiconductors, the resonance frequency depends on the band-gap energy: $\frac{d\omega_o}{dT} = \frac{1}{h}\frac{dE_g}{dT}$. Therefore, $\frac{dn}{dT} \propto -\frac{dE_g}{dT}$. Since the bandgap of silicon is inversely proportional to temperature, this explains why the refractive index of silicon is directly proportional to temperature for short wavelengths.

In this work, we observed that the refractive index of silicon is inversely proportional to temperature (Fig. 4.5 & 4.6). In order to explain this theoretically,

we must go back to the more general solution for the refractive index temperature dependence [80] [81] :

$$\begin{aligned}\frac{dn}{dT} &= C\frac{1}{n^2+k^2}\{\frac{\omega_o}{(\omega_o^2-\omega^2)^2+g^2\omega^2}(n-\frac{\omega_o^2-\omega^2}{(\omega_o^2-\omega^2)^2+g^2\omega^2}[n(\omega_o^2-\omega^2)+kg\omega])\frac{d\omega_o}{dT}\\ &+ \frac{1}{(\omega_o^2-\omega^2)^2+g^2\omega^2}\beta[n(\omega_o^2-\omega^2)+kg\omega]\\ &+ \frac{\omega}{[(\omega_o^2-\omega^2)^2+g^2\omega^2]^2}\{-n(\omega_o^2-\omega^2)g\omega+\frac{k}{2}[(\omega_o^2-\omega^2)^2-g^2\omega^2]\}\frac{dg}{dT}\} \qquad (4.19)\end{aligned}$$

Assuming that a heavily doped semiconductor behaves like a metal, we can use the free electron approximation, where $\omega_o = 0$, since electrons were not bound. In addition, assuming that the dominant absorption is caused by free carriers in the long wavelength side of the spectrum, then the band-to-band absorption would be insignificant. Therefore we can ignore the temperature dependence of the band gap energy. With these assumptions we arrive at the following expression:

$$\begin{aligned}\frac{dn}{dT} &= C\frac{1}{n^2+k^2}\frac{1}{\omega^4+g^2\omega^2}(\beta[-n\omega^2+kg\omega]\\ &+ \frac{\omega^3}{\omega^4+g^2\omega^2}[n\omega g+\frac{k}{2}(\omega^2-g^2)]\frac{dg}{dT}) \qquad (4.20)\end{aligned}$$

In the mid infrared region where ω is small, $g > 2w\frac{n}{k}$, therefore: $\frac{dn}{dT} \propto -\frac{dg}{dT}$. The fact that the plasma absorption minimum does not change with temperature suggests that the carrier concentration (N) and effective mass is relatively insensitive to changes in temperature. With the assumptions that the effective mass of silicon is not a strong function of temperature, and the temperature effect on intrinsic carrier concentration is insignificant comparing to the extrinsic carrier (dopant) concentration in the sample, within the temperature rang of our interest, we find that: $\frac{dg}{dT} \propto -\frac{d\mu}{dT}$. Consequently, we find the refractive index temperature dependence to be:

$$\frac{dn}{dT} \propto \frac{d\mu}{dT} \tag{4.21}$$

Equation (4.21) tells us that the temperature dependence of n is directly proportional to the temperature dependence of mobility (μ). It has been reported that μ is inversely proportional to temperature for both electrons [82] and holes [83], consequently, the refractive index of silicon is inversely proportional to temperature for long wavelengths. Our observation is consistent with the conclusion drawn from our theoretical analysis.

4.5 Effect of Refractive Index Dispersion on Film Thickness Measurements

The film thickness measurements rely on the changes in the refractive index of silicon in the infrared region [70]. As shown in Figure 4.4, the maximum refractive index change occurs around the plasma absorption edge in the heavily doped substrate. The dominant portion of the spectrum where the interference occurs is at the longer wavelength region. This is indeed what we observed. Figure 4.9 shows the interference fringes of a lightly doped epi-film on a heavily doped substrate, the fringes have the maximum magnitude in that region of the spectrum. Although the film thickness can be calculated from the period of these fringes, we usually use the interferogram directly from the FT-IR without performing the Fourier transform. Our real-time *in-situ* epi-film thickness monitoring results were obtained from the interferogram.

The fundamentals of epi-film thickness measurements using FT-IR were reported previously [70], and we are going to simply use the results here. We have shown in [70], that the difference between reflection and emission FTIR is a 180° phase change in the sidebursts [70], consequently, we will just analyze the case of

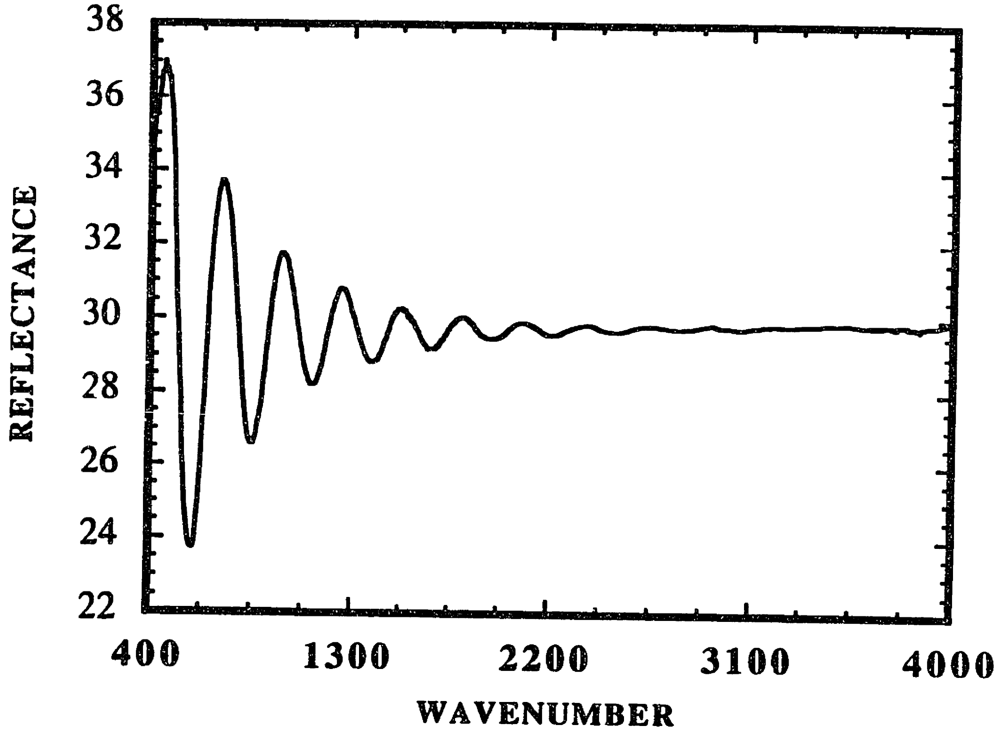

Figure 4.9: Reflectance of a lightly doped epi-film on a heavily doped substrate.

reflection FT-IR here. The side burst in an experimentally measured interferogram can be represented theoretically by [70] :

$$I_r = R_{0,1}T_{0,1}R_{1,2}T_{1,0}e^{-\alpha\Delta}I_o \cos k\Delta \tag{4.22}$$

where α is the absorption coefficient; $\Delta = 2dn_1 \cos\Theta$; d and n_1 are the epi-layer thickness and refractive index, respectively; Θ is the angle of incidence; I_o is the IR source intensity; $R_{l,m}$ is the Fresnel reflection coefficient for normal incidence from substance l (with refractive n_l) to substance m (with refractive n_m) [65]; and $T_{l,m}$ is the corresponding Fresnel coefficient for transmission.

With the understanding that refractive index of silicon changes with dopant concentration, we now can study the effect of refractive index variation on the epi-film thickness measurements. Using equation (4.22) and a computation tool like Matlab, we are able to calculate the interferogram. The position of the sidebursts in an inter-

ferogram determines the thickness of the epi-film, and the sideburst can be obtained theoretically by taking an inverse Fourier transform of equation (4.22). For the study of interference effects, we have made the following assumptions and simplifications: 1) considering only one reflection, and assuming the epi-film is perfectly transparent to IR; 2) assuming an abrupt interface between the epi-film and substrate and neglected phase change at the interface; 3) treating the infrared source as an ideal black body radiation source using Planck's radiation law; and 4) restricting wavelength region in mid-IR (2.5 - 25 μm).

We carried out the computation with these assumptions. Figure 4.10 shows the result of our simulation. Fig.4.10(a) shows the resulting interferogram using a constant refractive index of 3.42, and Fig.4.10(b) shows the resulting interferogram using the measured refractive index of a lightly doped material. For both (a) and (b), we used the same refractive indexes for the 0.004 Ω-cm material. Clearly, the dispersion in the refractive index distorts the interferogram in two ways: 1) it introduces noise in the interferogram; and 2) it introduces error to the film thickness measurement when the assumed refractive index is different than the actual refractive index. To overcome this problem, three possible approaches may be taken. 1) Introduction of a thick initial epi-layer with known refractive index or film thickness (ex-situ measured); depositing on top of that, accurate measurement may be achieved using the refractive index of the existing thick epi-layer (need to take into account of the temperature effect) to get deposited thin film thickness. This may be a solution if the deposited film is much thinner compared to the initial thick epi-film. This was the approach we took to measure epi-film thickness *in situ* and in real-time [84]. 2) Calibration runs under the same process condition to find the effective refractive index. As suggested by [68], this approach is commonly used in general industrial practice. 3) Theoretically simulate the interferogram. This is a very complex problem. Historically, there have been several schools of thoughts attacking this problem by doing phase corrections [68] [69] and by curve fitting the sample reflectance [85]. These

approaches were mostly problem specific, and were not generally adopted by FT-IR instrument manufacturers. More comprehensive theoretical as well as experimental work is needed to develop a generic model.

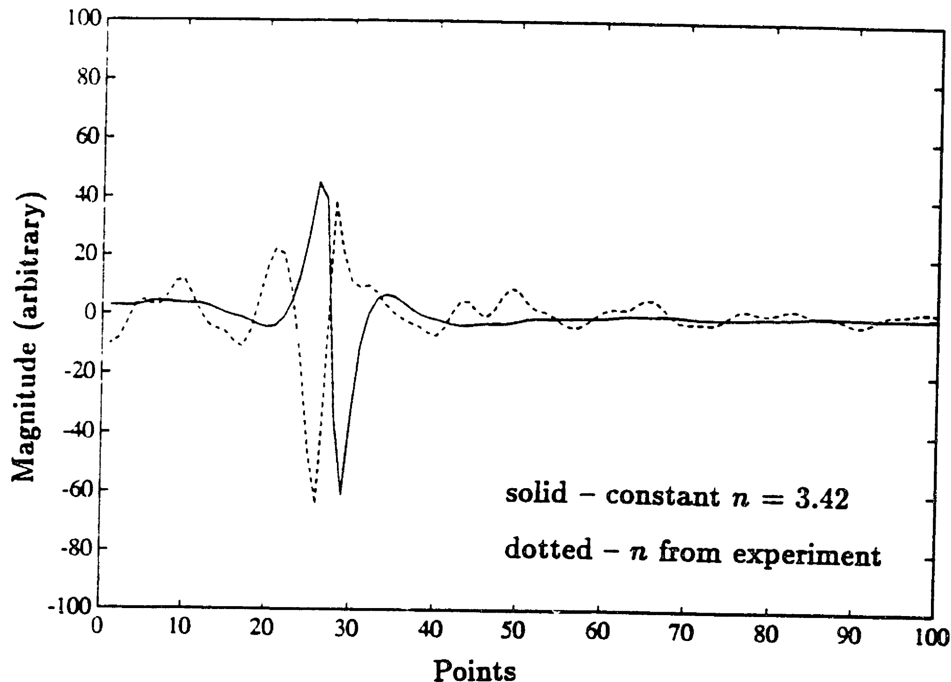

Figure 4.10: Comparison of simulated interferograms using (a) a constant refractive index, (b) measured refractive index.

4.6 Summary

The refractive index of silicon is a critical parameter for film thickness measurement. Experiments have been carried out to measure the refractive index of silicon as a function of sample doping concentration, IR wavelength, and sample temperature. As expected, we observed a strong dependence of refractive index as a function of substrate doping concentration. This allows us to create an optical interface in the IR spectral region by growing a lightly doped epi-film on a heavily doped substrate. Moreover, we observed that the refractive index of heavily doped silicon also varies

significantly with wavelength. Furthermore, we observed that refractive index of silicon decreases with increasing wafer temperature. By comparing the outcome of our theoretical calculations using a constant epi-film refractive index with the outcome that uses the experimentally measured refractive index, we can clearly see the effect of refractive index dispersion on the calculated interferogram. Our results show that the spectral dispersion of the refractive index can not be neglected for epi-film thickness measurement. Furthermore, when the measurement is done in real-time *in-situ* mode, the temperature dependence of the sample optical properties must also be taken into account for the film thickness measurement.

Chapter 5

ATR-FT-IR Monitoring of Plasma Cleaning

5.1 Introduction

Silicon surface cleaning is a critical process in semiconductor manufacturing. There have been many wet and dry cleaning techniques reported. For example, the silicon surface can be terminated with hydrogen by simply dipping the sample in HF solution [57]. However, from a manufacturing point of view, a dry process is preferred for the following reason: A dry process can be integrated with cluster tools, and it can also be done on oxide patterned wafers. Consequently, there are numerous reported works on silicon dry cleaning processes. One school of thought is to clean silicon using HF vapor [86]; another is to clean silicon using plasmas, e.g. an argon plasma sputtering [87] [88], a hydrogen plasma etching [96], or a mixture of argon and hydrogen plasma cleaning [97]. It has also been reported that a hydrogen terminated silicon surface can be obtained from a hydrogen plasma treatment where the surface possesses the same characteristics as that of a wet HF dip [98].

However, the mechanism of hydrogen plasma cleaning is not clear. Our objective here is to study the hydrogen cleaning process using *in-situ* real-time attenuated total internal reflection Fourier transform infrared spectroscopy (ATR-FTIR). The ATR-FTIR technique is highly surface sensitive. It has been reported that the ATR-FTIR technique can monitor less than 1% of a monolayer coverage of SiH stretch mode [60]. The principles and applications of ATR-FTIR technique have been reviewed and summarized elsewhere [55]. Our goal here is to apply this technique to investigate silicon surface cleaning using ammonia and hydrogen plasma.

The following questions will be addressed in this chapter: 1) can a silicon surface be cleaned using atomic hydrogen generated from a remote microwave plasma (with no ion bombardments)? 2) what is happening on the surface during plasma cleaning and what is the role of ions? and 3) can we use the ATR-FTIR technique for end-point detection of the cleaning process?

5.2 Experimental

Figure 5.1 shows the schematic of the experimental apparatus. The reactor used in this study has been previously described [102]. It consisted of a six-way Pyrex cross within which the wafer to be cleaned is placed on a platen that can be either RF or dc biased. The reactor base pressure is $2x10^{-7}$ Torr. The H_2 gas purified using a Pd catalyst is introduced through a quartz tube inside an Evenson-type microwave cavity. The quartz has a 90 degree bend that minimizes radiation to the sample. A remote plasma is sustained inside the quartz tube by a microwave generator at 140 Watts power and 2.45 GHz frequency. Radicals produced in the plasma travel about 28 cm before reaching the sample. At pressures above 0.2 Torr and no bias applied to the electrode, no current can be detected (with an in-series electrometer) and no glow is seen above the sample. Thus with only the microwave plasma on, only reactive

neutrals such as H are transported to the Si surface and the sample does not receive ion bombardment. With sufficient RF bias, however, a local discharge through the microwave-plasma-effluent is produced immediately above the wafer. In this case the sample surface is bombarded with ions in addition to the H atoms.

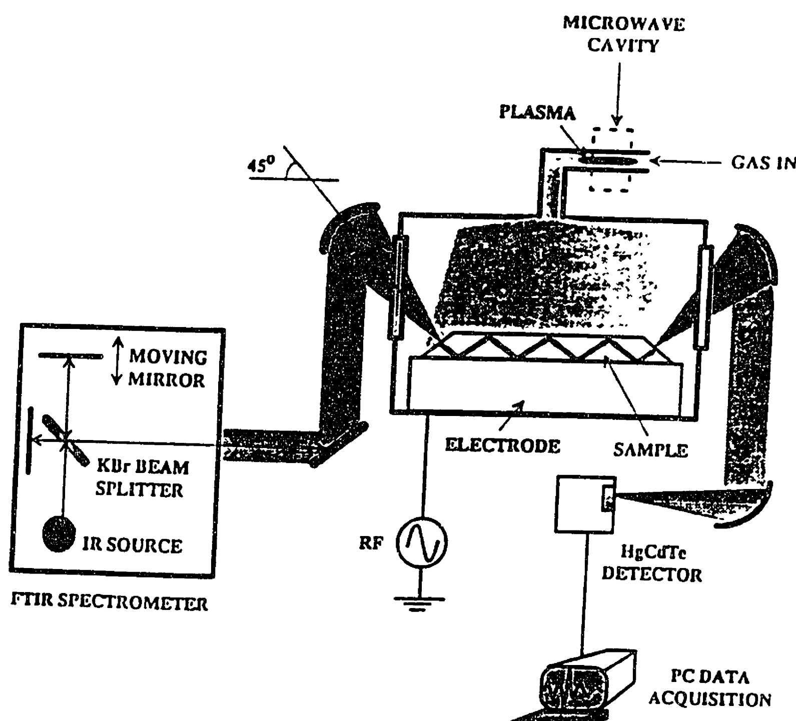

Figure 5.1: Schematic illustration of apparatus used for hybrid microwave-RF plasma cleaning of Si with real-time monitoring by ATR-FT-IR.

The samples are rectangular pieces (5 cm x 2 cm x 0.05 cm) of seminsulating <100> orientation silicon, which are beveled 45° on two opposing sides to facilitate IR coupling. The *in-situ* ATR-FTIR setup includes a Nicolet 510P FTIR spectrometer and a set of optics to bring the modulated IR beam to the reactor. After 50 internal reflections, the IR beam is collected by another mirror set-up and directed to a liquid nitrogen cooled MCT detector. An AT&T personal computer was used for data acquisition. For rapid real-time data collection, 50 scans at a resolution of 16 cm^{-1} were averaged to provide a real-time resolution of about 30 seconds. Changes in IR transmission are recorded by referencing the real-time spectra to the transmission

spectrum of a native oxide-contaminated sample prior to plasma treatement. Thus, an increase in transmission corresponds to a decrease in the surface concentration of a species, while a decrease in transmission corresponds to an increase in the species concentration.

5.3 Results and Discussions

It has been shown that both ammonia and hydrogen microwave plasma are efficient sources of atomic hydrogen [99]. For both ammonia and hydrogen microwave plasma treatment, Si-H vibrations have not been not observed for up to 20 min of treatment at room temperature, and at 300 °C. This result indicates that SiO_2 has not been removed by atomic hydrogen. In the room temperature hydrogen plasma treatment, an absorption peak around 2260 cm^{-1} was observed (Fig 5.2). It increases with increasing plasma exposure time and is consistent with the Si-H vibrational mode in H-SiO_2 at 2256 cm^{-1} (Fig 5.2) [100]. This absorption is also close to the Si-H stretching found in amorphous SiO_2 at 2280 cm^{-1} . The smaller absorption at 2200 cm^{-1} is close to SiH_2 stretching at 2220 cm^{-1} with two oxygen atoms in the backbonds (H_2SiO_2). Hereon we refer to the absorption features near 2260 cm^{-1} generically as H-SiO. The other features evident in Fig. 5.2 are assigned to O-H stretches at 3400 cm^{-1} and C-H stretches of the hydrocarbons on the surface at 2917 and at 2850 cm^{-1} which are all being removed from the surface. Infrared absorption by O-H from physisorbed water appears as a broad feature spanning the region from 3000 to 3700 cm^{-1} and is accompanied by the H_2O scissor mode at 1670 cm^{-1}. While water only adsorbs dissociatively onto clean Si (100) surfaces, it can physisorb on oxide surfaces terminated with OH. Infrared absorption of O-H from SiOH produced from dissociative adsorption of water is at 3660 cm^{-1}, and can be shifted to higher wavelengths and broadened as a result of hydrogen bonding. As a result, O-H stretch

from water and SiOH overlap and form a broad peak. Indeed, other experiments (see below) show a broad increase in transmission from 3000 to 3700 cm^{-1}, attributed to SiOH and water removal when the surface is clean from native oxide. Thus we conclude that atomic hydrogen reacts with the native oxide to form a HSiO layer that stays on the surface; and SiO_2 can not be removed using atomic hydrogen alone. To remove SiO_2 at low temperature additional energy must be supplied, so we create a weak RF plasma above the sample to provide an ion flux that complements the flux of atomic hydrogen from the upstream microwave plasma.

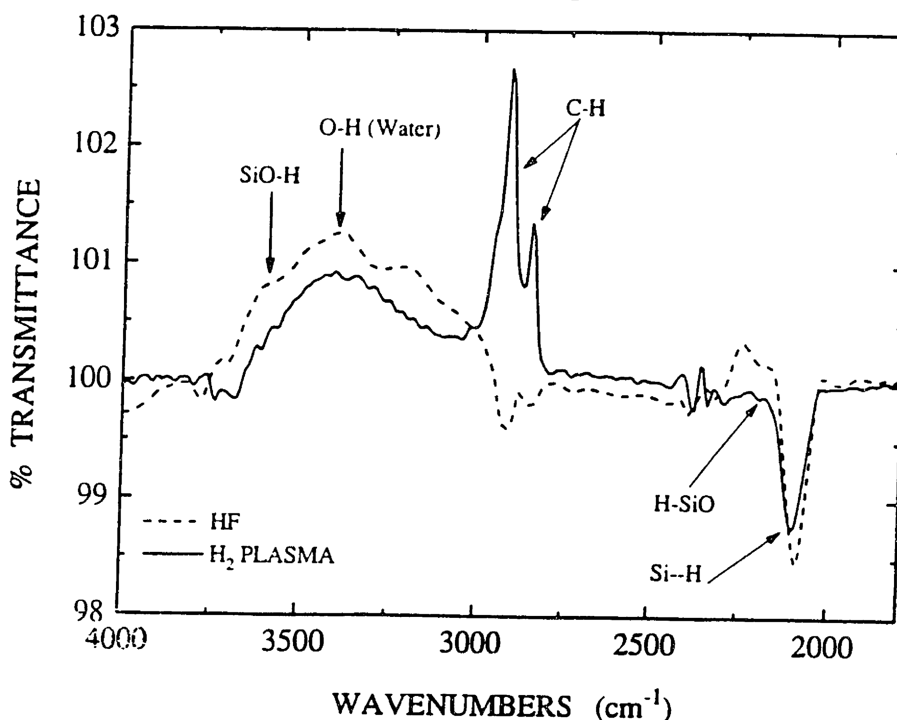

Figure 5.2: ATR-FT-IR spectrum (4 cm^{-1}, 1000 scans averaged) showing presence of H-SiO when samples are treated with only the effluent of a microwave discharge of H_2.

To illustrate the importance of using both upstream microwave plasma and localized weak RF plasma for Si wafer cleaning, we monitor the Si-H absorption feature in real-time as the plasma exposure conditions are changed. Figure 5.3(a) shows the area under the Si-H absorption peak versus process time. The data are plotted

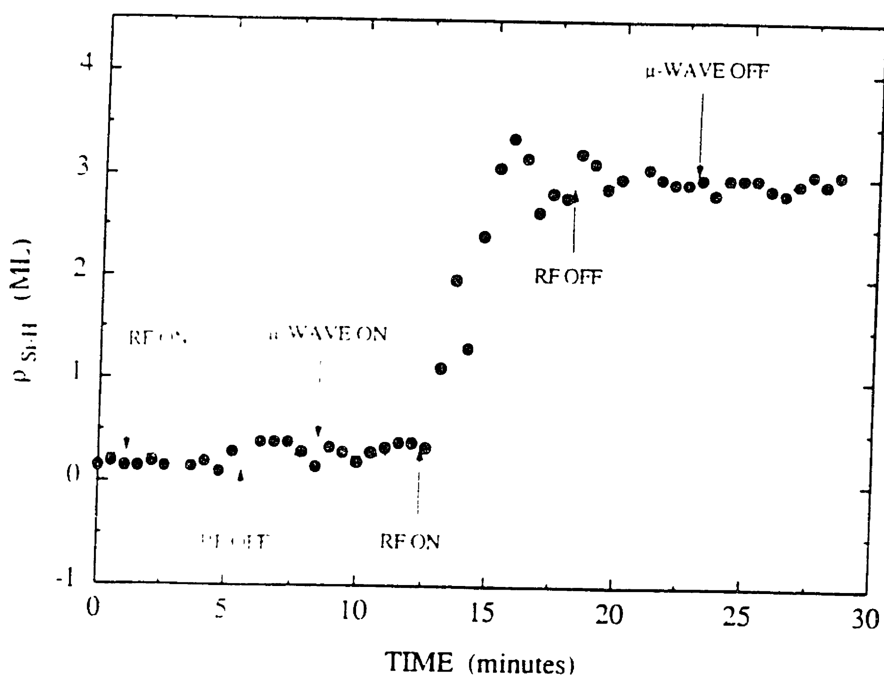

(a)

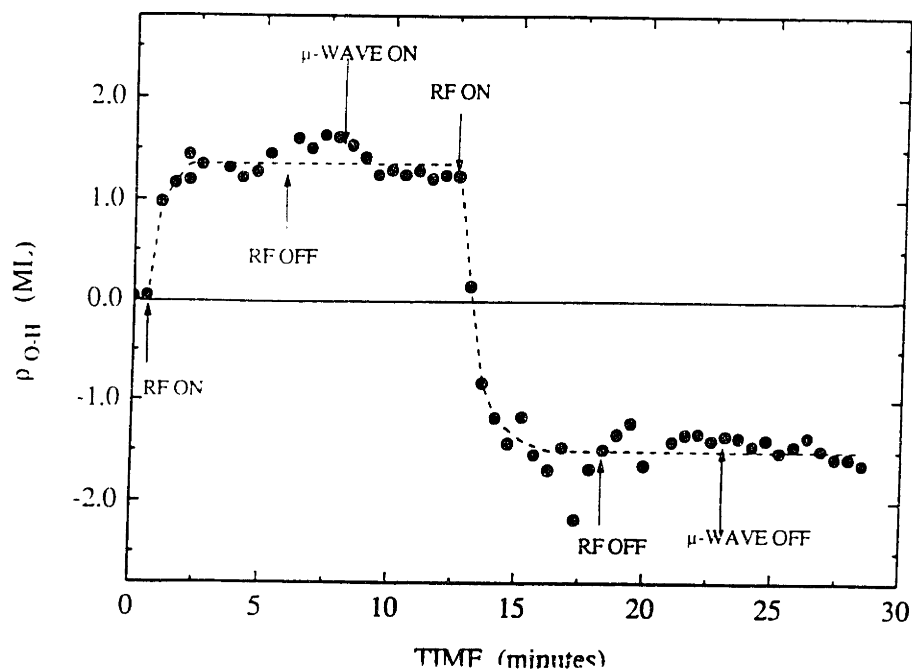

(b)

Figure 5.3: Real-time variations in (a) Si-H (integrated from 2000 to 2200 cm^{-1}), (b) O-H (integrated from 3000-3700 cm^{-1}) stretching absorptions as microwave and RF powers are sequentially turned on and off.

as a change in surface concentration in monolayers (ML) which is deduced from the change in transmission as follows. Since the absorption, or change in transmission, is small compared to one, we can write:

$$\int d\nu \frac{\Delta I(\nu)}{I_o(\nu)} = \int d\nu [1 - T(\nu)] \propto \alpha N \rho \tag{5.1}$$

where T is the transmittance relative to that of the untreated sample. α is the frequency-integrated absorption coefficient in units of $cm^{-1}ML^{-1}$, N=50 is the number of internal reflections from the adlayer, ρ is the change in surface concentration in ML, and the integration is over the absorption feature. The integrated absorption coefficient for Si-H is estimated from the measurements by Jakob *et. al.* [56] to obtain: $\alpha_{Si-H} \propto 10^{-2}$ $cm^{-1}ML^{-1}$. The relative changes in concentration are limited only by the signal to noise in this experiment and are believed to be accurate to better than 10%.

In this process, first, the sample is exposed to an RF plasma for 5 minutes. There was no observable Si-H absorption peak. However, a large, broad absorption peaking at 3400 cm^{-1} appears and is attributed to the O-H stretch mode of H_2O physisorbed on the native oxide surface [55] (Fig.5.3(b)). Next, the RF plasma is turned off, microwave plasma is turned on for 5 minutes keeping the pressure, flow rate and temperature constant. Still, no Si-H peak is observed, and absorption by the O-H stretch remains constant. With the microwave still on, the rf power is turned on again and now Si-H absorption increases rapidly (Fig.5.3(a)), while the broad O-H absorption decreases rapidly (Fig.5.3(b)). The O-H absorption also shifts to higher wavenumbers (Fig.5.4) as first water and then SiOH are removed. Five minutes later, RF plasma is turned off again, and the microwave plasma is maintained. Under these conditions, no adsorbed water on the surface indicates that the surface is hydrophobic, as expected for H-terminated Si surface. Continued microwave treatment does not increase the Si-H absorption proving that the surface is saturated.

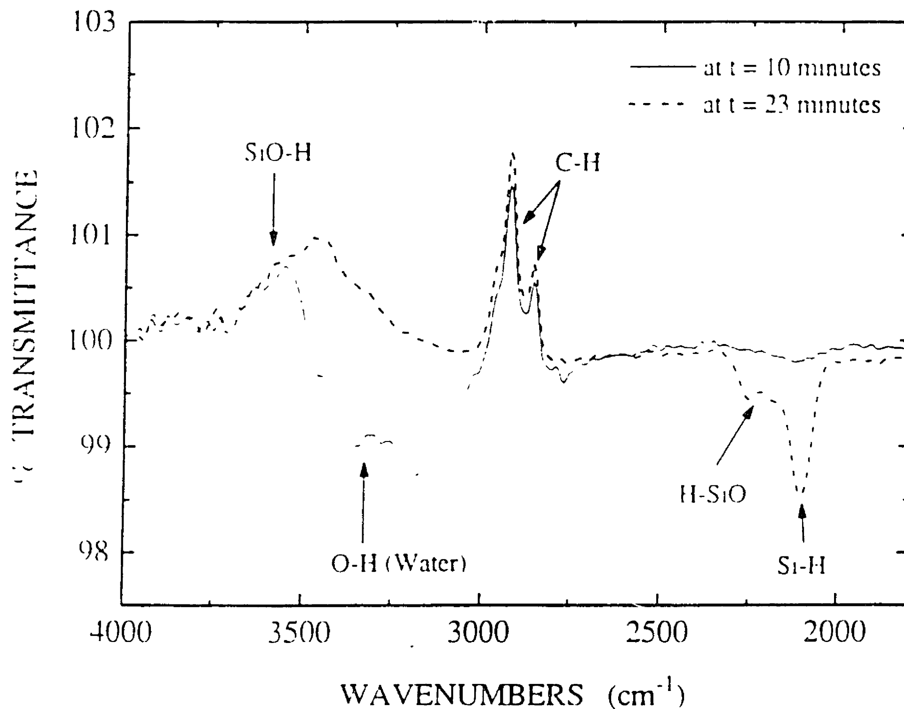

Figure 5.4: ATR-FT-IR spectra at different times during the treatment of Figure 5.3

Figure 5.3 and 5.4 show that the combined action of ion bombardment from the RF plasma and H atom flux from the upstream microwave discharge remove water, hydroxides, and oxygen resulting in a hydrogen terminated Si surface. From here on, we will refer to the combined microwave and RF plasma treatment as a hybrid process. While this experimental sequence nicely illustrates the power of real-time process monitoring for rapidly developing optimized processing conditions, the results shown in Fig.5.3 clearly indicate that the process has not yet been optimized. The amount of Si-H appears to exceed a mono-layer and suggests that the surface has been damaged significantly. As shown in Fig.5.4, the surface oxide has also not been completely removed. Another experiment is conducted under the same conditions using RF plasma alone for 15 minutes. The final spectrum with a broader but smaller Si-H absorption suggesting that although the RF plasma alone can remove SiO_2, it forms fewer Si-H bonds thus it is not an effective cleaning process.

We believe that the plasma cleaning process includes two major competing processes: 1) the removal of SiO_2 by hydrogen radicals with assistance of ion bombardment, and 2) the formation of HSiO and SiO_2 from plasma dissociation of H_2O. The treatment of the silicon surface by a hybrid microwave and RF NH_3 plasma produces more Si-H bonds than RF alone. This is because microwave plasma dissociates NH_3 to form NH_x and H_x. In the down-stream region, most of the active species are recombined to form a mixture of NHx, H, and H_2. This gas mixture is further dissociated by the local RF discharge; therefore the net atomic hydrogen concentration above the sample is expected to be higher than just an RF discharge of NH_3 gas alone. However, the absorption of H-SiO still remains in the ATR-FTIR spectrum, suggesting that the surface is not free of oxygen and is not fully terminated by hydrogen. Increasing RF power reduces the absorption of H-SiO, however, the Si-H absorption peak appears to be broadened. When RF power is increased to 50 Watts, a huge absorption peak at 2100 cm^{-1} is observed, and it increases rapidly as a function of plasma exposure time (Fig.5.5). The magnitude of this absorption corresponds to about 25 ML, too large to be attributed to SiH surface bonds alone, thus suggesting that a sub-surface H-terminated amorphous Si is being created. The fact that it keeps increasing as a function of plasma exposure time, suggests that damage migrates from the surface into the bulk of the sample. Also, at the same time, the IR transmission through the sample is attenuated at all wavelengths as the damaged surface absorbs and scatters the IR beam.

Using the hybrid microwave plus RF NH_3 plasma, we have not yet found a process that produces a sharp Si-H absorption peak like the one in the HF dipped case. From our recent work on plasma passivation of GaAs [101], we have found that NH_3 plasma generates more H_2O by interacting with the quartz wall than that of H_2 plasma. An excessive amount of H_2O present in the reactor may be the limiting factor that prevents us from cleaning the silicon surface by NH_3 plasma.

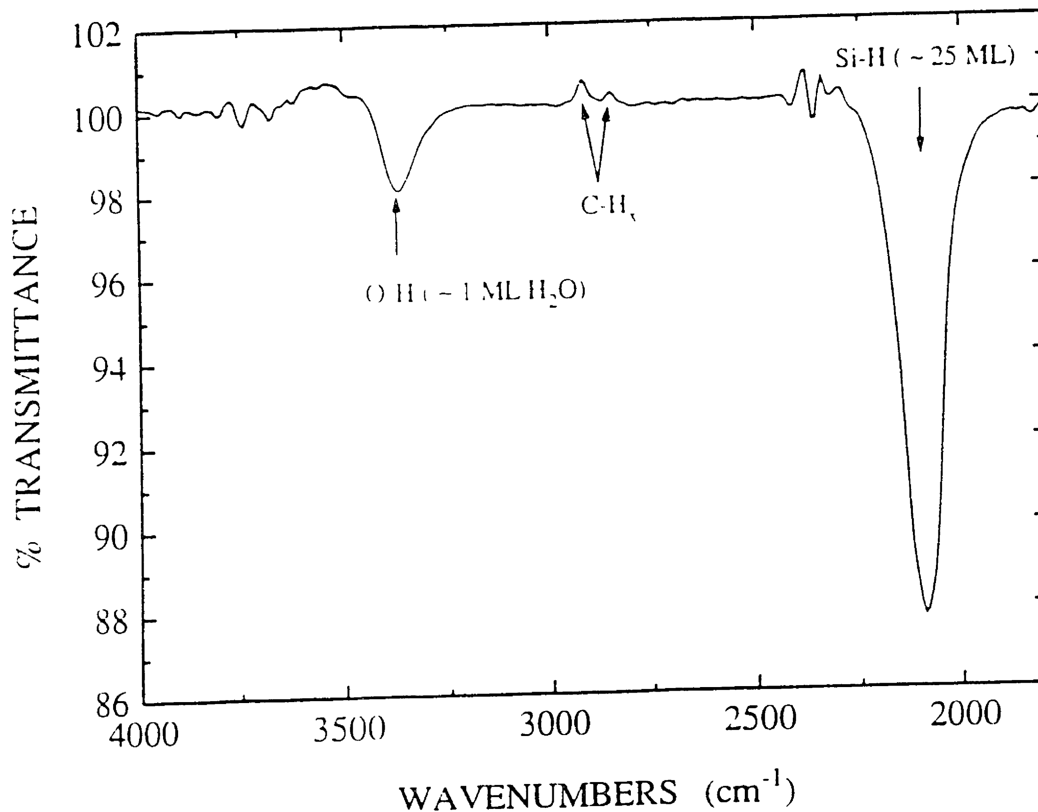

The large absorption peak at 2100 cm^{-1} is attributed to a-Si:H formed as a result of plasma damage.

In order to reduce H_2O and minimize the source of oxygen, we focused our attention on H_2 plasma that generates less water and try to optimize the cleaning process. In Figure 5.6, the dotted curve corresponds to the ATR-FT-IR spectrum obtained when Si is treated by hybrid H_2 plasma for 2 minutes under these conditions: 10W, 2 Torr, and 10 sccm H_2. Absorption by Si-H and H-SiO is evident. To remove the residual H-SiO, we want to minimize H_2O and increase H atom flux to the surface. At the same time, we want to reduce the ion energy flux to minimize damage. This is accomplished by increasing the H_2 flow rate to 50 sccm and decreasing the RF power to 3 W. We found that it was difficult to strike a RF H_2 plasma at low power (less than 20 W). However, with microwave plasma on, the RF power can be reduced to as low as 3 W. The higher flow rate of purified hydrogen at the lower pressure should help to reduce the relative concentration of H_2O in the reactor as well as increase the

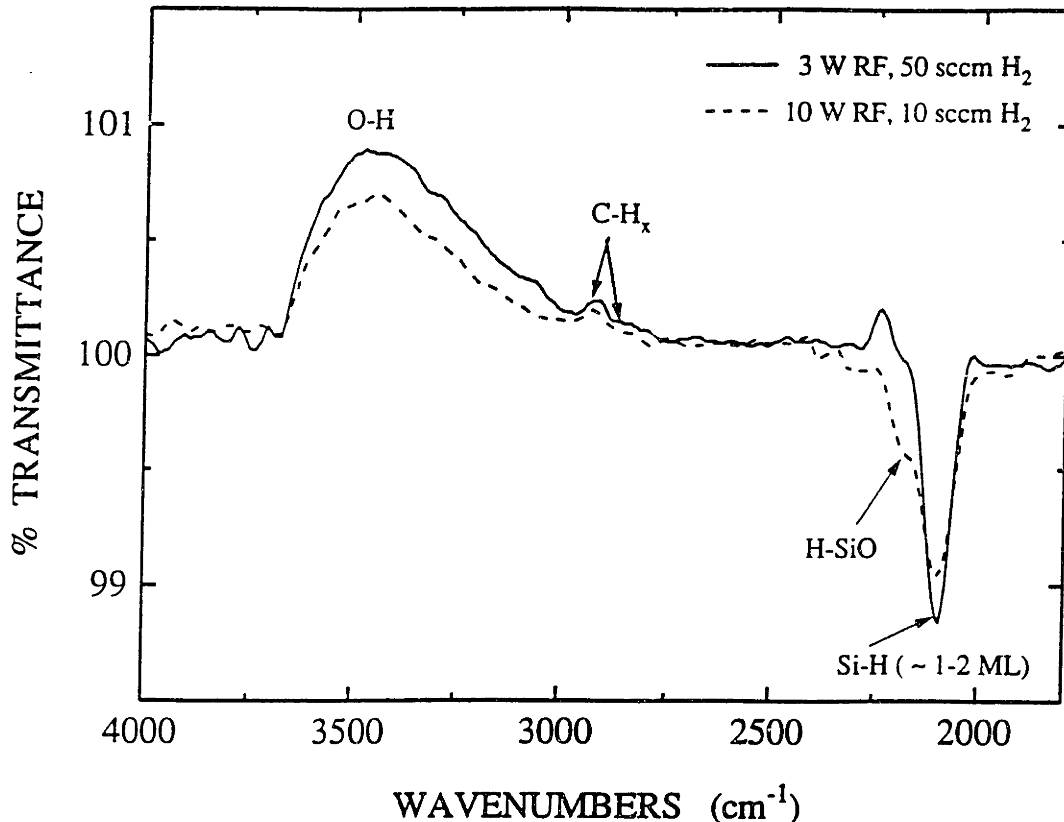

Figure 5.6: Si <100> ATR-FT-IR transmission spectrum relative to untreated sample. The dashed curve corresponds to a process that was too rich in ion energy flux relative to the neutral atom flux (10 W RF power, 10 sccm H_2). The solid curve corresponds to an optimized process (3 W RF power, 50 sccm H_2) resulting in oxide removal and Si-H formation. Other conditions were 1 Torr and 140 W microwave power.

the flux of H atoms to the wafer surface. After a 2 minute exposure, the H-SiO is removed completely (solid curve in Fig. 5.6). Further exposure results in no further changes indicating that the surface is saturated with atomic hydrogen (1-2 ML) and that the process is robust with respect to exposure time: no damage occurs even when the wafer is over exposed to the plasma. From the increase in transmission at 2260 cm^{-1} relative to an untreated sample, we see that the H-SiO present in the chemically grown native oxide [98] has been removed as well.

In the above experiment, the sample is first treated using a relatively low flux

of atomic hydrogen, where some oxide is being removed and some H-SiO is created. After changing the process condition to a relatively high flux of atomic hydrogen, all of the H-SiO species are removed. Consequently, the ratio of neutrals atom flux over the product of ion flux and energy is one of the most critical process paıameter in plasma cleaning of silicon surface. In addition, a high flow rate of ultra pure hydrogen gas reduces the relative concentration of H_2O in the reactor. The removal of H-SiO bonds in chemically grown oxide suggests that oxide is been removed by the hybrid plasma scheme. Over exposure to plasma treatment does not increase the Si-H peak, confirms that oxide is removed completely and the surface is saturated with Si-H bonds. Consequently, the endpoint for the native oxide cleaning is reached. Furthermore, it also suggests that either the plasma produces minimum damage to the surface, or the damage rate is less than or equal to the etch rate of silicon. Because accumulated residual damage would form excessive Si-H bonds as observed earlier (Fig.5.5).

To examine the repeatability of the cleaning process, a sample is taken out of the box without any pretreatment. After 2 minute of hydrogen plasma exposure under the optimized conditions, native oxide is removed. An over exposure of another 3 minutes does not alter the surface, suggesting that no damage is accumulated and the surface is saturated with hydrogen. When comparing to the chemical grown oxide, after plasma cleaning, the Si-H peak overlaps almost perfectly (Fig.5.7). This shows that hydrogen plasma cleaning process is robust against the characteristics of the native oxide, and after cleaning the surface is covered by the same amount of hydrogen. A third sample is cleaned under the same condition, which further confirms the repeatability of the process. The plasma cleaned and passivated sample was left in vacuum overnight, and there was no change observed in the ATR-FTIR spectrum indicating that the hydrogen terminated surface is stable in vacuum. However, it is less stable than the wet chemically treated (HF dipped) hydrogen terminated surface when expose to ambient air.

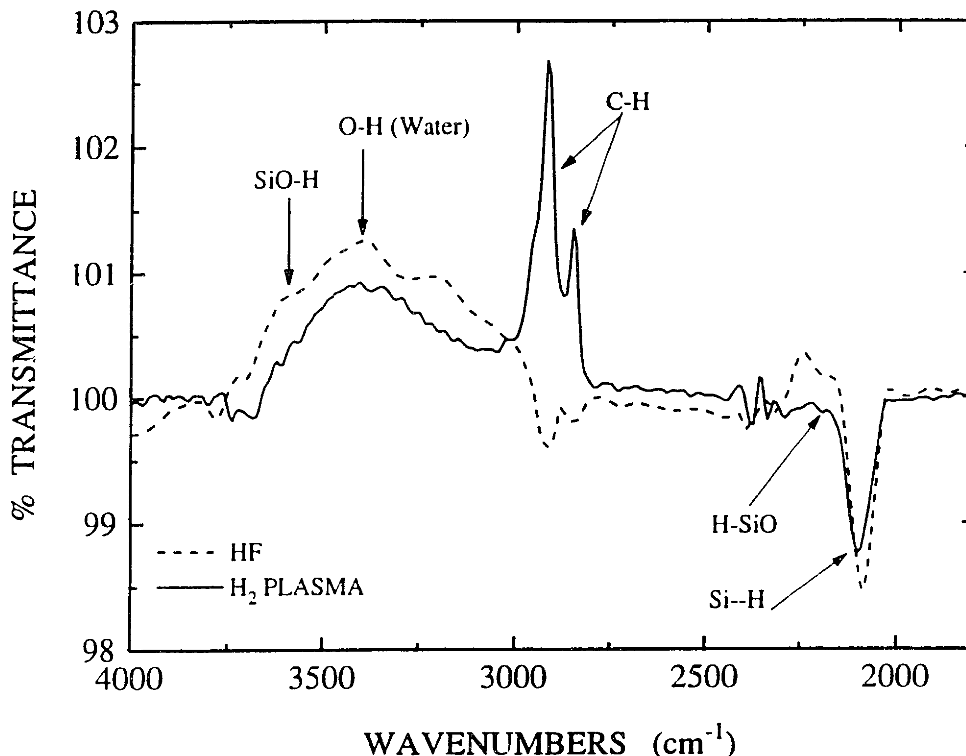

Figure 5.7: A comparison of two experiments performed under the same conditions, the result demonstrates the repeatability of the process.

For comparison, we also show in Figure 5.8, ATR-FT-IR spectrum obtained from an HF-dipped sample (dashed) overlaid with that for an H_2 plasma treated sample (solid). While O-H and H-SiO are removed and Si-H is formed in both cases, hydrocarbons are removed only with the plasma process. The cleaning of silicon surface includes the removal of native oxide and hydrocarbon. Although a wet HF treated surface is passivated against oxidation, it does not prevent hydrocarbon contamination.

Hydrocarbon contamination and removal: We have evidenced that HF dipping can add more hydrocarbon to the sample surface. Moreover, Eaglesham *et.al.* [101] reported that a highly C-contaminated surface (C can exceed 0.5 monolayers in Auger) can be a result of repeatedly redipping the sample in BOE. In addition, they investigated the effect of C-contamination in low temperature silicon epitaxy by

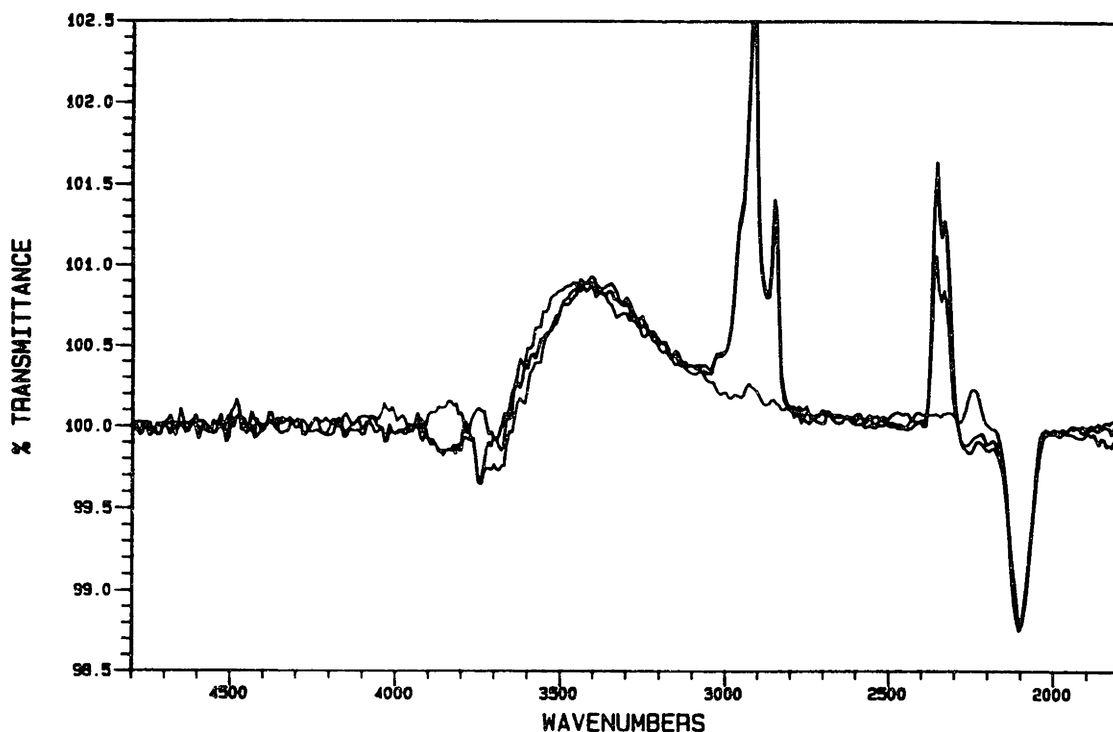

Figure 5.8: Comparison of H_2 plasma treatment with HF dip. While both treatments remove oxides and produce Si-H, the plasma treatment is more effective in reducing hydrocarbon contamination.

MBE. For a temperature less than 600 °C, only amorphous and polycrystalline silicon were deposited on C-contaminated substrates whereas defect free epi was deposited on carbon free substrates. Furthermore, the effect of hydrocarbon on device performance was also investigated recently [102]. In that study, MOS devices fabricated on C-contaminated surfaces were degraded. Consequently, hydrocarbon contamination can not be ignored, and must be removed. To remove hydrocarbon, a thermal desorption treatment at greater than 1100 °C is required [103]. It is well known that H_2 plasma can remove hydrocarbon effectively. Thomas *et.al.* reported a cleaning process tailored to remove carbon and native oxide individually by combining a 30s H_2 plasma exposure at 480 °C to clean carbon, and a 4 min anneal at 700 °C to remove native oxide [104]. Eagleshan et.al. proposed a 5 min 200 °C bake *in-situ* after HF dip to remove hydrocarbon in an UHV MBE reactor. Alternatively, we have

observed for the first time that hydro-carbon can be removed by atomic hydrogen at room temperature without the need of ion bombardment and without the need of a UHV environment [103]. The vibrational modes at 2925 and 2855 cm^{-1} were assigned to the C-H vibrations. From the real time ATR-FTIR spectrum, we observed that hydrogen plasma removes hydrocarbon faster than oxide which agreed well with published results [96] [98]. The endpoint of hydrocarbon removal can be detected by ATR-FTIR technique. When the C-H absorption peaks reach a constant and become independent of plasma exposure time, then the surface is hydrocarbon free.

5.4 Summary

We have shown that the real-time *in-situ* monitor can be used to study plasma cleaning of silicon surface, it can also be used for rapid process development. The real-time *in-situ* ATR-FTIR method allows us to watch chemistry as it happens on the sample surface. The real-time *in-situ* monitoring capability allows us to study the effect of changing process parameters on the same sample during the same experiment. This avoids many time consuming sample preparation, loading and unloading steps. An experiment often takes only a few minutes, however, to get everything ready may take half a day. By exploring the parameter space in real-time, one can get a hands-on feeling of the process. For example, changing some parameters in one way may lead you to the right direction for getting the desired results, conversely, changing the parameters in the other way may produce grief consequences. In addition, the significance of each process parameter can be determined in real-time. Consequently, the parameter space needs to be explored is being reduced significantly, and *in-situ* monitor can steer you toward the right direction, thus new processes can be developed and optimized timely and effectively.

In this Chapter, plasma cleaning of silicon surface is investigated in real-time

by ATR-FTIR technique. By monitoring the vibrational modes of Si-H, H-SiO, O-H, and C-H, a successful cleaning process using a remote microwave plasma and a RF plasma is found. The cleaning process is critically depended on the flux ratio of the neutrals to that of the ionic species. A high flow rate of hydrogen gas and a low RF power plasma sputtering are required to remove silicon dioxide. However, hydrocarbon can be cleaned effectively by atomic hydrogen with or without plasma sputtering. Moreover, Endpoint detection of oxide and hydrocarbon cleaning is demonstrated by ATR-FTIR monitoring of the vibrational modes of Si-H and C-H, respectively. Furthermore, excessive Si-H bonds resulting from a plasma damaged surface is observed. The results demonstrate the power of real-time monitoring for new process development and understanding. The major conclusions of this work are:

1) SiO_2 can not be removed by atomic hydrogen at room temperature and at 350 °C. Plasma sputtering is required to supply enough energy to break Si-O bonds. However, hydro-carbon can be removed by atomic hydrogen generated from NH_3 or H_2 plasma with or without ion bombardments.

2) plasma cleaning of SiO_2 in our system consisted of two competing processes: the removal and the reformation of SiO_2, and H-SiO. By proper selection of gas and process conditions, one can minimized the SiO_2 formation rate and enhance its removal rate. The ratio of neutral atoms flux over the product of ion flux and energy is one of the most critical parameter in plasma cleaning of silicon surface. An optimized process condition is: 140 Watts of microwave power, 3 Watts of RF power; 1 Torr of pressure, and 50 sccm of H_2 flow rate. A high flow rate of H_2 increases the flux ratio of neutrals to ions. In addition, a high flow rate of H_2 reduces the relative concentration of H_2O and oxygen to that of hydrogen in the reactor.

3) Neither RF nor microwave plasma can clean SiO_2 effectively at room temperature. However, the combination of the two gives the best results. Microwave plasma produces more atomic hydrogen and at the same time reduces the RF power

to sustain a localized RF plasma. The RF plasma provides the necessary energy to break Si-O bonds, which allows hydrogen atoms to chemically react with the unbound Si-O forming H-SiO, H_2O and Si-H.

4) Damage was also detected by ATR-FTIR. A damaged surface resulting in excessive Si-H bonds formed in the amorphourization Si surface layer. The amorphourized surface has excessive Si with dangling bonds, which were subsequently terminated by atomic hydrogen. Thus, ATR-FTIR spectrum of a damaged sample shows a huge Si-H absorption peak at 2100 cm^{-1}.

5) Endpoints detection for cleaning of both hydrocarbon and native oxide are demonstrated for the first time by monitoring the vibrational modes of C-H and Si-H respectively. We observe that hydrogen plasma cleaning of hydrocarbon is faster than that of oxide. When the absorption peak of Si-H at 2100 cm^{-1} saturates, the surface is terminated by Si-H bonds and the cleaning can be stopped.

Chapter 6

Silicon Epitaxy Equipment and Process

6.1 The Multi-chamber Single-wafer Chemical Vapor Deposition Reactor

The conventional epitaxial reactor has only one chamber which is tailored for a particular process. For example, a quartz tube placed in a furnace can be used to perform Silicon Chemical Vapor Deposition (CVD). In such a reactor, examination of the end product is the only way to know the effects of parameter variation. There are severe limitations to this approach: (1) the problem will not be realized until the damage is done, (2) examining the end product can only give an overall effect of the whole process; it is difficult to pinpoint the origin of the problem, (3) disturbances during the process are random in nature therefore making them difficult to be predicted and corrected; consequently, processes often can not be reproduced. The fabrication of future generations of devices requires many complex processes and relies on improved

control and understanding of these processes, so that reliable and reproducible results can be obtained. To overcome the limitations of a conventional reactor and meet the requirements of future device fabrication, the reactor should be designed with maximum flexibility. Our particular design allows us to explore and demonstrate the use of *in-situ* monitors. Information obtained from these monitors can be fed-back to control the process parameters in real-time. Such continuous feedback control will lead to more reproducible and more flexible manufacturing, higher yields, and in particular, will allow run-to-run variations to meet the specifications of the end product.

6.1.1 Description of System Components

The cluster concept was utilized in our reactor design. The concept of a cluster involves an integration of multiple independently controlled (smart) vacuum chambers or modules around a central wafer handler [1]. It is capable of performing multiple processes within an ultra high vacuum (UVH) ambient. The beauty of this design lies not only in simplifying the complexity of processes and control of these processes by breaking them into modules so that each can be investigated and controlled separately, it also makes the technology transfer and upgrade easier by transferring or upgrading single modules rather than the whole system. Moreover, with proper arrangement, parallel processing is conceivable.

Our reactor is designed with a total of five chambers. Four of the chambers have been installed, and the fifth one is reserved for future expansion (Figure 6.1). The four chambers are named: Load Lock, Analysis, CVD, and ECR. All chambers are constructed using chemically polished 304 stainless steel. Excluding the Load Lock chamber, all chambers are designed to achieve UHV.

The Load Lock chamber functions as a wafer introduction chamber. It consists of a ionization gauge and a thermocouple for pressure measurements. The pumping

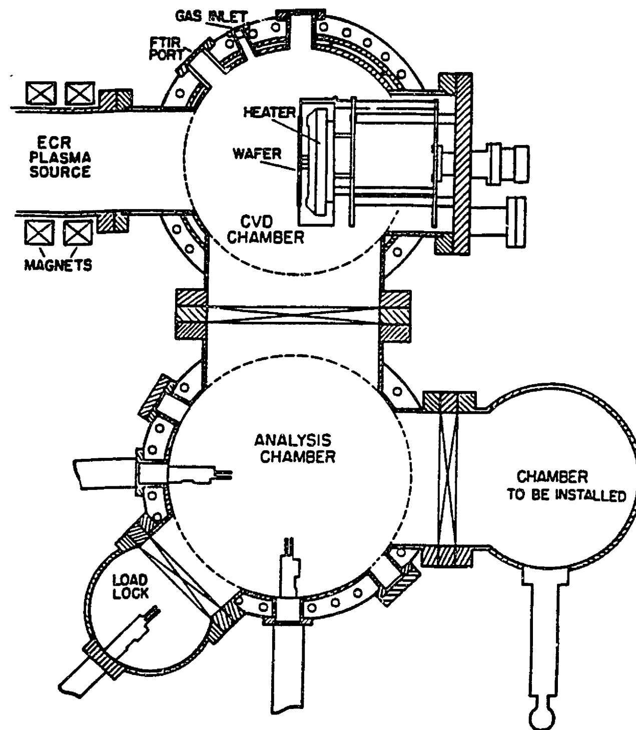

Figure 6.1: Schematic of the horizontal cross section of the MS-CVD system

unit consists of a 100 l/s turbo molecular pump (Alcatel CFF100) backed by a mechanical pump. A Load Lock chamber pressure of about 10^{-7} torr can be reached in approximately ten minutes after a wafer has been loaded.

The Analysis chamber functions not only as a analysis station but also as a central facility for wafer transfer. This chamber is designed with many ports for future implementation of *in-situ* analysis or inspection tools (e.g. RHEED, XPS, Ellipsometer etc.). It is a cylindrical chamber with an inner diameter of 14 inches and a height of 14 inches. The top plate of the analysis chamber is removable so that unexpected future modification can be done by designing a new top plate. The transfer devices are mounted on this chamber. And they reside outside the CVD chamber after wafer transfer is completed. In this way, contamination from transfer devices is reduced (see Figure 6.1). Currently, the main pumping unit is located under this chamber. The unit consists of a chemical resistive 1500 l/s turbomolecular pump (Leybold

Turbovac1500) backed by a mechanical pump (Leybold Trivac 65BCS). The process pressure is measured by a capacitor manometer (MKS390HA) and is regulated via a control gate valve (10 inch inner diameter valve with a stepper motor, Series 64, model 64048-UE52 by VAT of Switzland) located between the chamber and the turbo pump. A Varian ion gauge is used to measure the chamber base pressure. Presently, one overnight pumpdown without baking can yield a base pressure of 1×10^{-8} Torr. With several hours of baking, a base pressure of 5×10^{-9} Torr can be reached. A KBr window is used in the reactor which is not UHV graded, once this window is replaced, a lower base pressure can be expected with appropriate baking.

The CVD chamber is where the epitaxial film growth takes place, and *in-situ* monitors have been implemented here. Currently, an Emission Fourier Transform Infra-Red Spectrometer (EFTIR) is used for epi-film thickness monitoring, a Quadrupole Mass Spectrometer (QMS) is used for gas species monitoring and a Langmuir probe is used for plasma diagnostics. The CVD chamber is a double wall water-cooled chamber with an inner diameter of 14 inches and a height of 12 inches. The purpose of water cooling is to reduce deposition on the wall and therefore reduce a source of particulate contamination. There are over a dozen ports available for future addition of *in-situ* monitors in this chamber. There is a pumping port and space allocated under the chamber for future installation of an independent pumping unit to further reduce cross contamination problems. Also, to keep the contamination at a minimum and assure an ultra clean environment for processes, process gasses are delivered through gas purifiers before entering the CVD chamber. The gas flow is controlled by pneumatic valves and mass flow controllers (MKS 100 series models). Up to eight gases can be delivered at one time.

The ECR chamber is attached to the side of the CVD chamber. Plasma can be generated by ECR excitation and extracted by magnetic fields or an electrostatic potential applied to the substrate in the CVD chamber. The ECR source is a com-

mercial ASTEX mirror magnets source, which consists of a tube 6 inches in inner diameter and 13 inches in length surrounded by two coiled magnets. The microwave is generated by a magnetron at a frequency of 2.45 GHz, guided by a rectangular copper wave guide passing through a dummy load, directional coupler, a three stub tuner and a circulator entering the ECR chamber through a UHV graded alumina window. A separate gas inlet is located at the side of the alumia window in the ECR chamber. The microwave power can be varied from 0 to 1000 Watts.

6.1.2 System Summary

Major features of the reactor include:

- Ultra high vacuum
- Multiple chambers
- ECR plasma
- *in-situ* monitoring
- *in – vacuo* wafer transfer

Major capabilities include:

- Low temperature epitaxy
- Multiple processes within UHV
- *in-situ* thickness monitoring using EFTIR
- *in-situ* gas analysis using QMS
- *in-situ* substrate surface cleaning by ECR plasma

- *in-situ* surface analysis by low energy electron diffraction (LEED) spectroscopy
- ECR Plasma Enhanced CVD

It has the following components:

- Three stainless steel chambers
- A resistive/radiant heater/stage
- ECR plasma source
- *In − vacuo* wafer transfer devices
- Gas delivery and control system
- Pumping units
- Toxic gas detector and safety devices

6.2 Low Temperature Silicon Epitaxy

In general, an epitaxy process consists of two process steps, one of which is the pre-deposition substrate cleaning step and the other is the deposition step. Conventional CVD includes both high temperature (above 900 °C) cleaning and high temperature deposition steps[6]. A low temperature epitaxy process requires that both steps be carried out at low temperatures.

The key difficulty associated with low temperature silicon epitaxy is the lack of energy for oxide removal and surface mobility. At high temperatures, the oxide layer is thermally desorbed:

$$SiO_2 + Si \rightarrow 2SiO_{(g)} \quad (6.1)$$

But at low temperatures, the above reaction is either too slow or goes in the other direction. This problem hampered epitaxy researchers for over two decades [109]. Only until recent years, successful techniques have emerged. These techniques can be divided into three major classes, each with a different approach.

The first class of techniques is energy enhancement [107]. Plasma enhancement, an example of energy enhancement, was successfully demonstrated in [108]. It deals directly with the lack of energy by supplementing thermal energy with external energy, namely energy from a plasma. The oxide layer is removed through Ar/H_2 plasma sputtering at low temperatures. In a plasma enhanced deposition, surface mobility is also increased. Minority lifetime up to 480 μs has been reported for epitaxial films deposited at 775 °C[108]. The second class of techniques is rapid thermal processing or RTP. RTP circumvents the problem of oxide removal at low temperatures by doing processes at high temperatures but only for a very brief period. Wafer temperature is raised and lowered rapidly which enabled minimum wafer exposure to high temperatures, on the order of tens of seconds [110]. This way, even though wafers are exposed to high temperatures, the movement of dopant atoms is minimal because the diffusion length $\sqrt{D \bullet time}$ is kept small. The last class of techniques is ultra high vacuum CVD. Pioneered by B. Meyerson [111] , UHV-CVD avoids the problem of oxide removal altogether by keeping the system so clean that no stable oxide on the substrate surface is formed even at low temperatures. High quality epitaxial materials have been grown at $T \geq 550$ °C[111].

Our unique approach to reduce process temperature and contamination levels is by using both plasma and Ultra-high Vacuum (UHV) technology. Electron Cyclotron Resonance (ECR) plasma was chosen because it has many advantages over conventional radio frequency plasma. ECR plasma offers high excitation rate, low plasma potential and high efficiency. ECR plasma enables processing below 1 mTorr, consequently minimizing recombination reactions among the species, utilizing neu-

trals and ionic species generated in plasmas more effectively, and reducing wafer contamination. Additionally, low plasma potential leads to reduction of damages. From the results of the investigation reported in Chapter 5, these advantages are criticle for effectively cleaning of silicon surface using plasma.

A detailed review of ECR plasma and its applications can be found in Chapter 2 of ref.[112]. ECR plasma was characterized by using a Langmuir probe. The details of this work is reported in Chapter 5 of ref.[112], only the results are summarized here. Langmuir probe I-V curves are measured when a plasma is excited with a microwave power of 300 Watts at 2.45 GHz, a pressure of 1 mTorr, an Ar or He gas flow of 30 sccm, and a floating susceptor. From the probe I-V curve, by assuming a Maxwellian electron energy distribution, one can readily find the plasma potential, and calculate electron temperature and plasma density. The plasma potentials for Ar and He plasmas were found to be 15 V and 30 V, respectively. The kinetic energy of the ions can be obtained by taking the difference between the plasma potential and the applied electric potential (bias voltage at the susceptor). The kinetic energy of the ions dictates the sputtering yield and radiation damage. Electron temperatures for Ar and He plasmas were found to be about 2.6 eV and 3.4 eV, respectively. Electrons are the primary source of excitation in a plasma, and electron temperatures are indicative of the chemical species being excited within a plasma. Such information allows for the study of the etching or growth mechanism of thin films. Plasma densities for Ar and He plasmas were found to be about 3.6×10^{11} cm^{-3} and 5.2×10^{11} cm^{-3}, respectively.

Single crystalline silicon films were successfully deposited (thermal deposition, without plasma enhancement) using SiH_4 as a source gas, at pressures from 1 to 4 mTorr, and at temperatures between 500 °C and 700 °C. Typically, the wafer is *in-situ* cleaned by ECR hydrogen plasma at the process temperature. After plasma cleaning, thermal CVD is immediately followed using silane as the source gas. Table

6.1 summaries some typical silicon epitaxy process conditions.

The ability to monitor chemical species on a silicon surface opens the possibility for precise end-point control of pre-deposition cleaning process. The precise end-point control of precleaning process is very important for high quality epi-film deposition. For example, when plasma was used, over sputtering produces lattice damage, and under sputtering leaves residue oxide on the surface. Both cases can not produce defect free high quality films [107].

Process Steps	Process Parameters	Set Points
ECR Plasma	Magnet Currents	150A, 120A.
Cleaning	Microwave Power	300 Watts
(Hydrogen)	DC Bias	+10 V
	Pressure	1 mTorr
	H_2 flow	20 sccm
	Temperature	600 °C
Deposition	SiH_4	10 sccm
(Thermal CVD)	Pressure	1 mTorr
	Temperature	600 °C

Table 6.1: Silicon epitaxy process conditions for both plasma cleaning and deposition

Chapter 7

Applications of E/FT-IR

7.1 Introduction

Cluster tools have to be supplemented with *in-situ* monitoring/measurement. Without the additional flexibility and capability, time and resources will be wasted because problems could not be discovered until the damages have been done. Sometimes problems can not be pinpointed because the effects of later processes may cover up what had occurred earlier. Therefore, *in-situ* monitoring is a necessity for cluster tools, it adds flexibilities to understand, optimize, and control of manufacturing processes in general.

In the next section (Sec. 7.2), an example of using E/FT-IR for thermal radiation measurement is presented. The results lead to a better understanding of the radiative properties of silicon, which is important for subsequent film thickness measurements using E/FT-IR. In Section 7.3, the characteristics of E/FT-IR for film thickness measurement is presented. The limitation, robustness, and a comparison to conventional FT-IR technique is reported in detail. Issues such as E/FT-IR's repeatability, reproducibility, and the effect of wafer rotation are evaluated. In Section

7.4, real-time applications of E/FT-IR in silicon epitaxy is presented in detail. First, the application of E/FT-IR in low temperature and low pressure silicon CVD process research is demonstrated. Next, the application of E/FT-IR in silicon CVD process monitoring and control is demonstrated. Finally, the application of E/FT-IR in the development and optimization of ECR hydrogen plasma pre-deposition wafer cleaning process is demonstrated. A summary of this Chapter is provided in Section 7.5.

7.2 Thermal Radiation Measurements by E/FT-IR

To investigate the deviations of silicon radiation from the ideal black body radiation, we carried out a set of experiments to measure IR radiation using E/FT-IR. A Bio-Rad FTS 40 spectrometer equipped with a room temperature deuterated triglycine sulfate detector, and a wide band CsI (cesium iodide) substrate beamsplitter, was used to collect the E/FT-IR spectra. To test the feasibility of using E/FT-IR for semiconductor characterization, experiments were conducted (refer to Figure 7.1 for experimental arrangement) using the Harrick EM-1 accessory mounted on the emission port of the spectrometer. The accessory consisted of an ellipsoidal focusing mirror, sample stage, aluminum mask, and a cartridge heater beneath a sampling stage. The sample temperature controller regulates the selected temperature to within 1 °C. The maximum temperature is limited by this design to 250 °C. Typically, emission from the wafer is collected over a large solid angle to maximize the signal-to-noise ratio. In these experiments, wafers with different resistivities were individually heated. Emission spectra were collected from several substrates at 200 °C with a 4 cm^{-1} resolution and by spectral averaging of 300 scans. It takes about 15 minutes to acquire one sample spectrum with the FTS-40 spectrometer. During spectral measurements, the emission accessory is enclosed in a box purged with nitrogen gases.

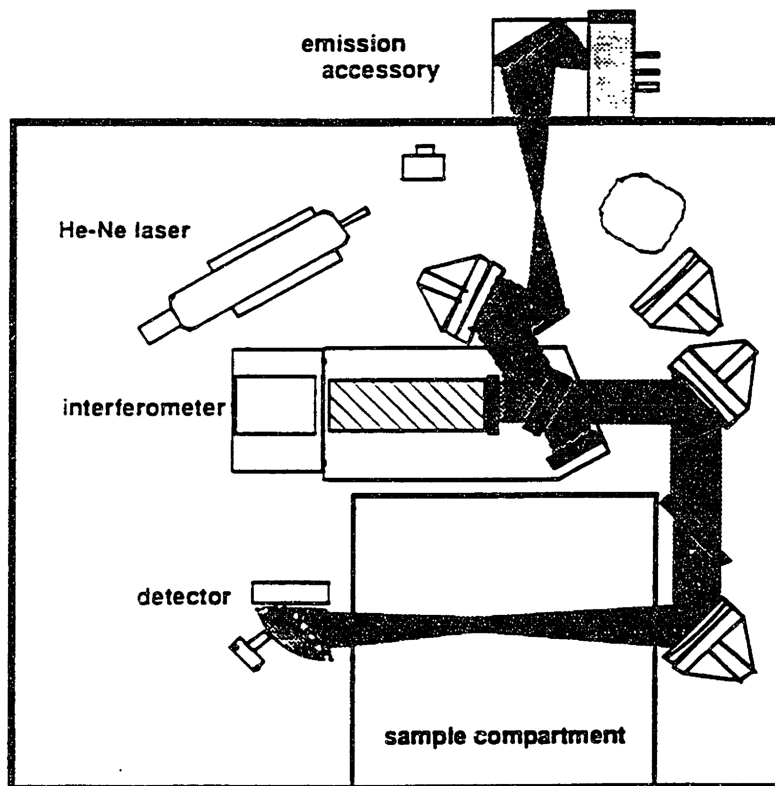

Figure 7.1: Schematic of the E/FT-IR setup used to perform the thermal radiation measurements

Emission spectra were collected from several substrates at 200 °C with a 4 cm^{-1} resolution and by spectral averaging of 300 scans. In Figure 7.2, the strongest emission spectrum is seen to originate from carbon lamp black powder (Fisher Scientific), the lowest emission spectrum is from a shiny aluminum mirror, and the three central spectra are from Czochralski silicon < 100 > substrates. The resistivities of these n-type silicon substrates are 10-20 Ω-cm, 0.01-0.02 Ω-cm, and 0.004-0.005 Ω-cm corresponding to Figures 7.2(b), 7.2(c), and 7.2(d), respectively. Additionally, the middle substrate (Figure 7.2(c)) has a layer of lightly doped (20-40 Ω-cm) epitaxial silicon.

The emission spectra of carbon black and that of the mirror at 200 °C were as expected. The carbon black generated the reference black body spectrum used for subsequent data analysis (Figure 7.2(e)). The low emission profile from the mirror

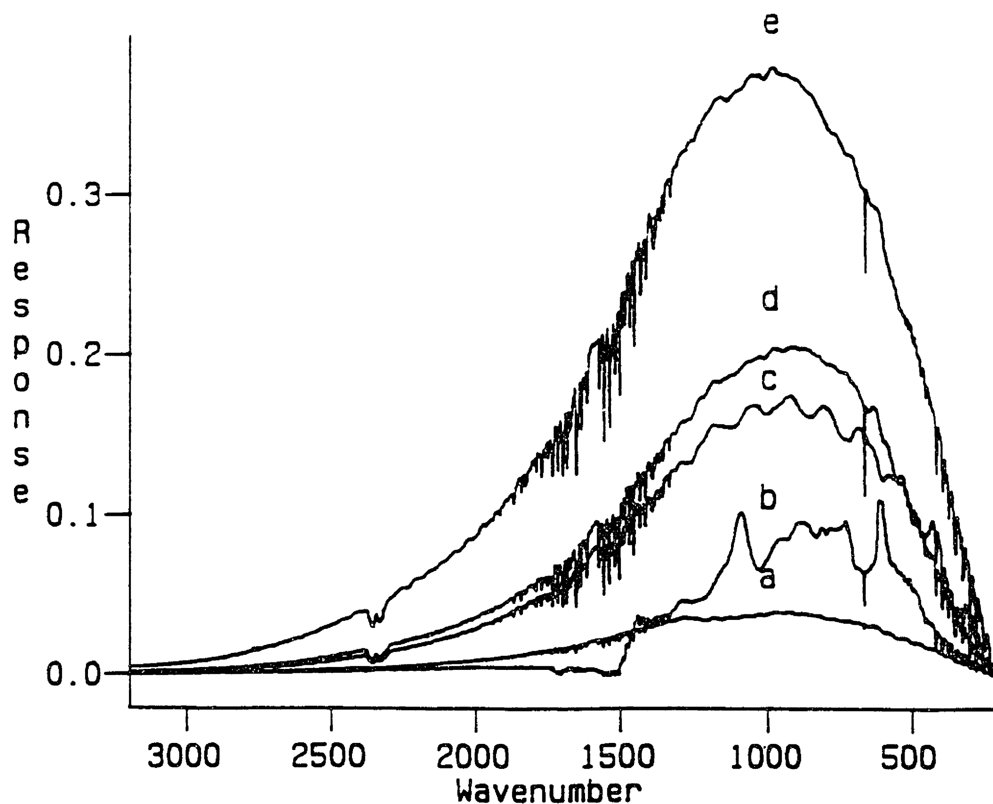

Figure 7.2: Blackbody curves collected for: a) shiny aluminum mirror, b) 10-20 Ω-cm silicon substrate, c) 0.01-0.02 Ω-cm silicon substrate, d) 0.004-0.005 Ω-cm substrate, and e) carbon lamp black powder.

was due to the background emission from components in the accessory and FT-IR spectrometer optics (Figure 7.2(a)). The most interesting emission data, however, are the spectra obtained from the silicon substrates with different resistivities. The emission spectrum for a heavily doped (0.004-0.005 Ω -cm) substrate (shown in Figure 7.2(d)) resembled that of a black body. One reason for this is that when a substrate is heavily doped, there are numerous free carriers (on the order of 10^{19} cm^{-3} in this substrate). Since these carriers are not bound, no associated resonance exists; therefore, only a broad band absorption with a subsequent broad band emission is observed. The strong absorption and re-emission from these carriers dominate the emission spectrum, and the vibrational bands corresponding to lattice phonons and impurity molecules are not observable. Observing that the broad band emission intensity is

proportional to free carrier absorption, and the free carrier absorption depends on dopant concentration or resistivity of the sample, a possible indirect way to monitor dopant concentration is discovered. First, a calibration curve can be found experimentally by plotting the broad band emission intensity at a constant temperature against the dopant concentration of a set of samples. Then, to measure the dopant concentration of an unknown sample, one can measure its emission intensity at the same temperature, and the corresponding dopant concentration can be found from the previously determined calibration curve.

Equation (3.19) shows that the radiation intensity is directly proportional to the absorption coefficient. This agrees well with our observations. The spectrum for the lightly doped (10-20 Ω -cm) substrate, with dopant concentration on the order of 10^{15} cm^{-3}, exhibited less free carrier effect than the heavily doped sample (Figure 7.2(b)). The energy was absorbed partially by lattice phonons and partially by free carriers; consequently, re-emission by these phonons appeared at some well defined resonance frequencies, and the re-emission from the free carriers simply contributed to the broad band spectral offset. The spectrum shown in Figure 7.2(c) is also from a heavily doped substrate (0.01-0.02 Ω-cm) possessing a lightly doped epitaxial silicon film. It exhibits features due to both the substrate and epi-film. Optical interference fringes resulting from light traveling through the epi-film are superimposed upon the substrate emission spectrum.

The emittance of the sample can be obtained by the ratio of its emission profile versus that of a blackbody. Since the radiation collected by the detector is comprised of contributions from the surroundings and from the spectrometer itself, spectral compensation is required to acquire the emission spectrum solely due to the sample. This correction becomes extremely important when attempting to acquire spectra of samples at temperatures near room temperature or samples exhibiting low emissivity. Calculation of the corrected emittance (ϵ) is accomplished according to

Eq.(3.20)

Figure 7.3 shows a comparison of the emissivity of the lightly doped sample at 200 °C to its transmission spectrum acquired at room temperature. The emittance spectrum of the sample was computed using Equation (3). Note that when comparing the two spectra, the bands in the emission spectrum are inverted. This is because a low transmission band corresponds to high absorption, or in other words, a strong emission intensity with an apparent reversal in band intensity. From this emittance spectrum, the bands can be readily assigned by the same methods that are used to analyze the transmission spectrum without any need for additional efforts. The silicon lattice phonon bands were observed at 609cm^{-1}, 736 cm^{-1}, and 885 cm^{-1} (refer to Figure 3), in addition to bands associated with impurities (Si-O) at 1102 cm^{-1}. By performing a complete spectral analysis such as this [64], the oxygen concentration within the bulk of the silicon substrate can be found.

No individual vibrational bands were resolved in the emittance spectra for the two heavily doped substrates studied here. It is believed that free carrier absorption and re-emission dominated these systems. Figure 7.4 illustrates the emittance of a heavily doped substrate with a lightly doped epi-layer. The overall spectrum consisted of contributions from the substrate emission, the epi-film emission, and re-absorption of the subtracted emission by the overlaying epi-film. Therefore, the interpretation of this spectrum is somewhat complicated. For simplicity, we neglect here the emission and absorption within the lightly doped epitaxial silicon film and consider only the emission from the substrate. At the substrate/epi-film interface, part of the radiation from the substrate is reflected and part of it is transmitted. The part that is transmitted will travel through the epi-film reaching the epi-film/air interface, where part of the radiation is emitted and part of it is reflected. When the reflected beam arrives at the epi-film/substrate interface, another reflection takes place, and the reflected beam will again travel through the epi-film and be emitted at the surface of

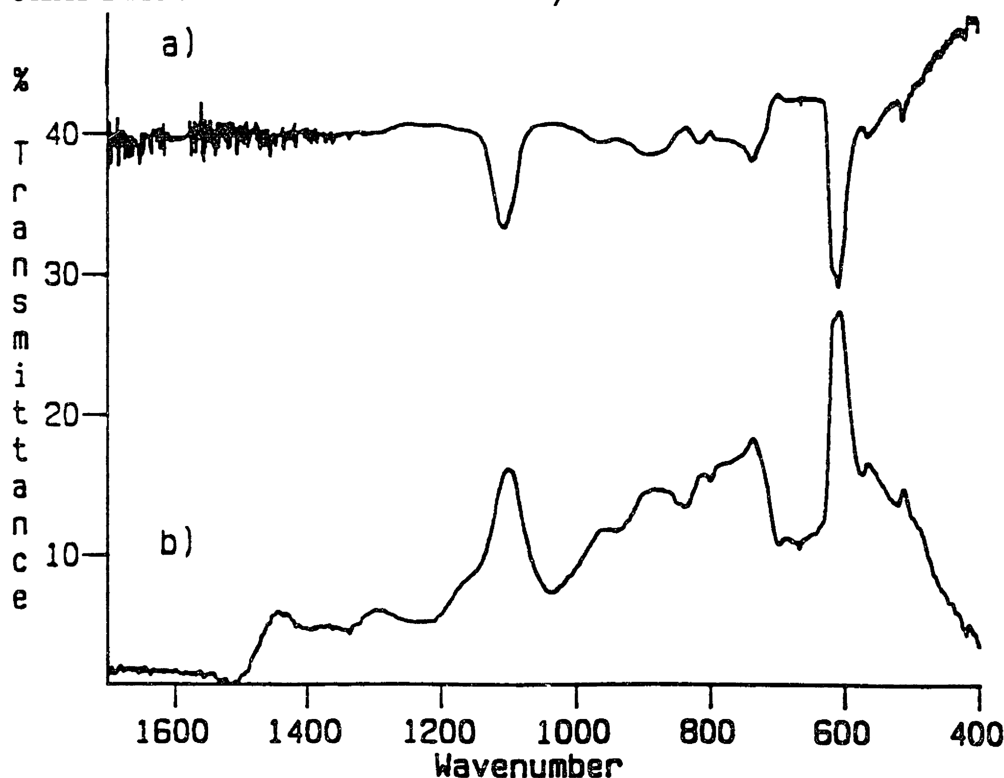

Figure 7.3: Comparison of the a) transmittance and b) emittance spectra collected for the same lightly doped silicon sample directly overlaid on same %T scale. Emittance spectrum is collected at 200 °C.

the film. These two emitted beams interfere with each other causing the appearance of a cosine wave (interference pattern) superimposed upon the emission spectrum. They are exactly $2dn_f\text{Cos}\Theta$ out of phase, where d is the film thickness, n_f is the film refractive index, and Θ is the angle of emission from the surface norm. From the interference pattern collected for the sample, its film thickness can be easily extracted and, in this instance, is calculated to be 11.4 micrometers (confirmed by a spreading sheet resistance profile measurement) assuming a constant refractive index of 3.42. A detailed theoretical treatment of epi-film thickness measurements by R/FT-IR and E/FT-IR will be be given in the next section.

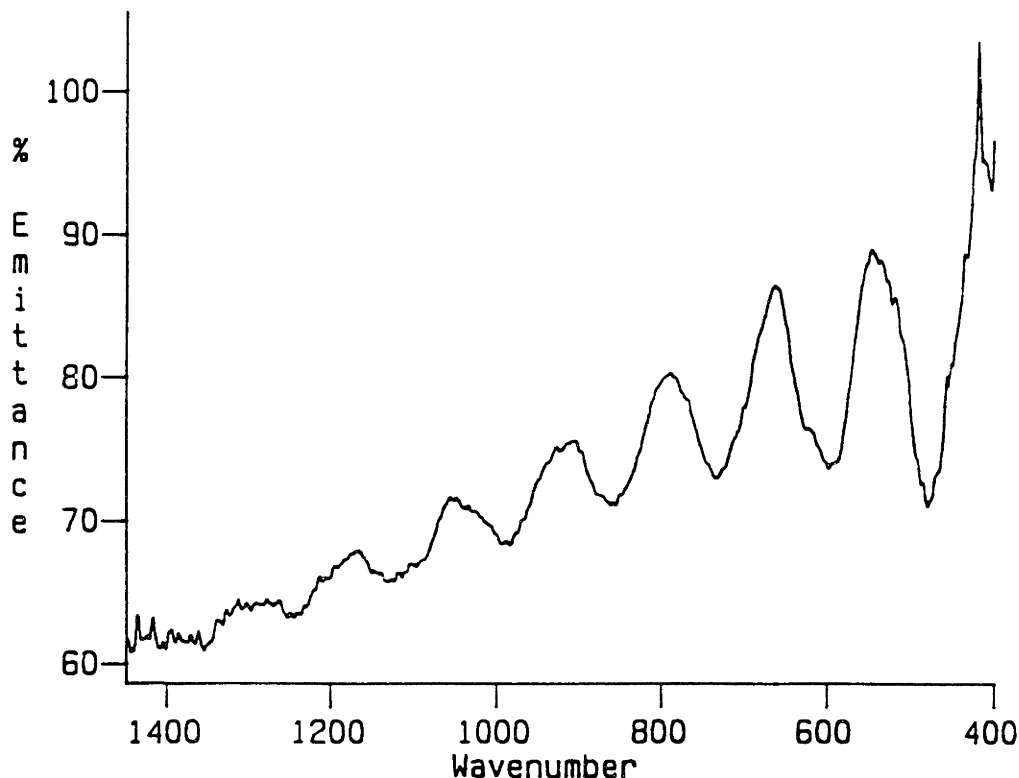

Figure 7.4: Emittance spectrum acquired at 250 °C for a heavily doped substrate (0.01 Ω-cm) with a lightly doped epi-layer.

7.3 Characterization of E/FT-IR for Film Thickness Measurements

The epitaxial film thickness is a critical parameter that must be accurately measured and controlled. For example, it is necessary to ensure that outdiffusion and autodoping during device processing do not consume the entire epitaxial film. In addition, several bipolar transistor device parameters, such as breakdown voltage, junction capacitance, transistor gain, and high frequency performance, depend on the epi-layer thickness. As described in Chapter 2, There are many thin film thickness measurement techniques [113] [123]. However, they are either destructive or not applicable in the case of a silicon epi film on a silicon substrate. The commonly used technique for epi film thickness measurement is the reflectance measurement using an exter-

nal IR source, and is widely used in industries [51] [113] [114]. But it is only used for *ex − situ* measurement, that is, the measurement done outside of the growth or etching chambers. Moreover, it is difficult to be adapted for *in-situ* measurement in its present form. The E/FT-IR technique, on the other hand, takes advantage of a heated wafer as the infrared source. By analyzing the IR emission, we can obtain epitaxial silicon film thickness measurements on heavily doped silicon substrates.

7.3.1 Limitations of FT-IR

Source Band Width

Lasers are used in most of interferometric methods because they have some attractive properties (e.g. monochromatic and coherent). One commonly raised question is why FT-IR uses a broad band thermal radiator (typically a ceramic source at over 1000 °C) rather than a laser as the light source? One distinction of FT-IR technique from other optical technique is the use of a broad band light source rather than a monochromatic laser source. This is because when using FT-IR, we are measuring the Fourier transform of the source and, if the source is broad, then its spatial Fourier transform will be narrow, which corresponds to higher precision in measurements. If a monochromatic laser source is used, the Fourier transform of this delta function in k-space will be a cosine function in x-space. The resulting continuous cosine interferogram makes the side burst identification difficult. Ideally, if one can find a source that has a infinitely broad band, and its spectral distribution changing cosinusoidally with wavenumber (or frequency), then its spatial Fourier transform will be a delta like function which reduces the ambiguity of peak picking for film thickness measurements. Hence, its accuracy will be higher. In reality, an infinitely broad band source is not feasible, which limits the resolution of the technique.

Interference by Incoherent Light Source

Thermal radiation source is a chaotic light source. The shape of its emission spectrum is determined by statistical spread in atomic velocities and the random occurrence of collisions. This complex process can be interpreted as an excited atom radiating a electromagnetic wave steadily at a frequency f_o until it suffers a collision. During the collision, energy levels of the radiating atoms are shifted, and the wave train is interrupted for the duration of this collision. When the wave is resumed after the collision, its characteristics are identical to those prior to the collision, except that the phase of this wave is unrelated to its phase before the collision. The time between collisions is called the coherence time. The coherence time is random in nature, so we will consider τ_c as the average coherence time. Moreover, the path length associated with the coherence time is known as the coherence length, and L_c represents the average coherence length. Their relationship is given by [132]: $L_c = c\tau_c$,

$$L_c = c\tau_c \tag{7.1}$$

where c is a scaling factor that determines the relationship between the temporal and spatial aspects of the beam fluctuations. Here, we will consider only the spatial incoherence of the radiation source. The source intensity in between can be represented by:

$$i(x) = \sum_n i_n(x) h_n(x) \tag{7.2}$$

where

$$h_n = \begin{cases} 1 & \text{if } \mathrm{nL_c} < \mathrm{x} < \mathrm{(n+1)L_c} \\ 0 & \text{otherwise} \end{cases}$$

and the Fourier transform of the source $i(x)$ is:

$$I(k) = \sum_{n=-\infty}^{\infty} I_n(k) \otimes H_n(k) \tag{7.3}$$

where I_n and H_n are the corresponding Fourier transform of i_n and h_n, respectively. The "$\otimes$" sign stands for the convolution [48] of two functions. When the mirrors are at the equidistance from the beam splitter, or when the phase shift is exactly compensated by the movable mirror, the wave will interfere with itself. For any

phase difference longer than $1/2(L_c 2\pi/\lambda)$, the beams will be out of phase due to the nature of incoherence. Therefore, the resulting interferograms have a narrow peak width. This feature is particularly desired for film thickness measurements.

Instrument Limitation

A severe limitation of this measurement technique is that it can not measure epi-films thinner than $\sim 0.2\ \mu m$. This is caused by the limited bandwidth of the source, the detector, the beam splitter, and the limited bandwidth that is transparent to the silicon epi-layer. A finite bandwidth results in a finite spatial width of its Fourier transform. This finite width does not pose a problem for thick film measurements because the center burst is well separated from the side bursts. But as film thickness decreases, the side bursts will start to overlap with the center burst making peak picking difficult. When the overlap is not significant, the problem is resolved by subtracting a reference interferogram from the sample interferogram. The subtraction of the two interferograms requires the alignment of the interferograms, which is accomplished by aligning the peak values of the two center bursts. Any misalignment will result in incomplete subtraction of the center burst even if the two center bursts are identical, and will also result in distortion of the side bursts. When the overlap of the side bursts with the center burst is not significant, the alignment of the center bursts of the sample and the reference interferogram can be accurate, and subtraction is reasonably complete. But this will not happen when the separations between the center burst and side bursts are close to their widths. Because the overlapping significantly shifts the true peak location resulting in ineffective suppression of the sample interferogram's center burst. Another way to determine the minimum measurable film thickness is to take a Fourier transform of the interferogram, and look at the interference fringes in the wavenumber (or frequency) domain. The minimum thickness is limited by the band width of the FT-IR (from 400 to 4000 cm^{-1}). Assume a minimum of a half interference fringe is needed for a reliable film thickness mea-

surement, this corresponds to a film thickness of 0.2 micron, which is the minimum thickness resolution of the instrument. The precision of this technique is limited by the frequency at which the interferogram is sampled [51], the noises from detector [133] and from absorption in the optical path.

7.3.2 Robustness of the E/FT-IR technique

In order to apply the E/FT-IR technique in manufacturing, several issues must be resolved. Issues such as the effect of heating lamp interference, window material, window stress and coating, temperature control and limitations, substrate dopant concentration, repeatability and reproducibility, and wafer rotation, are addressed in the following paragraphs.

Heating lamp interference: Measurements made by E/FT-IR are based on optical interference effects. The E/FT-IR is essentially a scanning Michelson Interferometer. By the principle of superposition, lamp heating interference will superimposed on the interferogram. Assuming the lamp with an intensity distribution I_L, there are three possible path to reach the FT-IR detector. The component (I_{L1}) goes directly from the lamp to the FT-IR detector. The component (I_{L2}) reflects from the reactor wall then enters the detector. The component (I_{L3}) bounces off the wafer before reaching the detector. By going through a similar analysis as that in Chapter 3.5, the contribution from the heating lamp is:

$$I_L(k) = I_{L1} + I_{L2} + I_{A_{L3}} + I_{B_{L3}} + 2\sqrt{I_{A_{L3}} I_{B_{L3}}} \cos k\Delta \qquad (7.4)$$

Where $I_{A_{L3}}$ and $I_{B_{L3}}$ are the reflections from the epi-surface and epi-substrate interface, respectively. The total source intensity enters the FT-IR detector is the summation of the radiation from the wafer (represent by Equation 3.29) plus the

contribution from the lamp:

$$I_{total}(k) = I_{A_e} + I_{B_e} - 2\sqrt{I_{A_e}I_{B_e}}\cos k\Delta + I_{L1} + I_{L2} + I_{A_{L3}} + I_{B_{L3}} + 2\sqrt{I_{A_{L3}}I_{B_{L3}}}\cos k\Delta \tag{7.5}$$

The contribution of I_{L1} and I_{L2} is to the dc term of the interferogram which gives rise to the background intensity. For film thickness measurements a reference interferogram consisting of all the dc terms is normally subtracted from the sample interferogram, so that only those terms with $\cos k\Delta$ remains. Thus the only term that might affect the shape of the side bursts is I_{L3}. However, in most cases, the heating lamps are placed perpendicular to either the front or the back side of the wafer, so that most of the reflected lamp radiations are perpendicular to the wafer surface, and will not be detected by the FT-IR. Consequently, I_{L3} is the weakest component, and the intensities of I_{L1} and I_{L2} are much stronger then I_{L3}. Hence, the effect of lamp radiation on E/FT-IR epi-film thickness measurement is minimum. There are several ways to reduce the I_{L3} component further: 1) Placing the lamp at the back side of the wafer. Since the substrate has to be heavily doped, it is opaque to IR. 2) Choosing the emission angle that will minimize the contribution from the heating lamps. 3) Using a filter to eliminate contributions from the lamp if the emission spectrum of the lamp is narrow. 4) Reducing the IR collection solid angle by placing the optics far away from the wafer and using a mirror with a small curvature (or a long focal length).

Window material, window stress and coating: Since the wafer is processed in a vacuum chamber and the FT-IR is place outside the reactor. All radiation must pass through an IR window which isolates the vacuum from atmosphere. Thus, the optical properties of the window (and window coatings), and the thickness of the window (and window coatings) will affect the IR signal. A simple way to evaluate these effects is using the system approach, where the window material, window stress

and coating can be represented by a transfer function. The transfer function is related to the optical properties of these materials and their thicknesses. Assuming that there are m-layers of window and coatings, the transfer function can be generalized in the following expression:

$$H_{wc}(k) = \prod_{i=1}^{m} T_i(k) e^{-\alpha_i d_i} e^{-jkd_i} \quad (7.6)$$

where H_{wc} is the transfer function for the window and all coatings. T_i, d_i, and α_i are the the transmission coefficient (depends on the refractive index), optical thickness, and the absorption coefficient of the i-th layer, respectively. From the Fourier transform theorems, we know that:

$$f(x - x_o) \leftrightarrow F(k) e^{-jkx_o} \quad (7.7)$$

where $f(x)$ can be any arbitrary function and $F(k)$ is the corresponding Fourier transform of $f(x)$. From equation 7.6 and 7.7, it is clear that the window and its coatings will reduce the light intensity. In addition, the entire interferogram is displace by a distance equivalent to the sum of the optical thicknesses of the window and its coatings. A shift of the entire interferogram will not affect the position of the side burst. Since the film thickness measurement is solely dependent on the location of the sideburst, the window material and its coatings will not affect the film thickness measurement as long as sufficient light intensity reaches the FT-IR detector. Consequently, the only requirement is that the window material must be transparent in the mid-infrared region (e.g. from 2.5 to 25 μm).

Wafer temperatures and substrate dopant concentrations: The effects of wafer temperature and dopant concentration on the optical constants of silicon is studied in detail in Chapter 4. The FT-IR film thickness measurements rely on the

optical interface created by differentially doping of the epi-film and substrate. For a lightly doped epi layer on a heavily doped substrate (p-type, 0.01-0.02 ohm-cm), epi film thicknesses were measured with the epi wafers at temperatures from 100 to 650 °C. For a more heavily doped substrate (n-type, 0.001-0.002 ohm-cm), the range is 100 to 900 °C. The lower temperature limit is due to the weak level of IR emission from the wafers at low temperature. The high limit exists because as temperature rises, the intrinsic carrier concentration in the film also increases. At the high limit, the intrinsic concentration is relatively high, and the refractive indexes of the film and substrate become closer to each other; consequently the optical interface between the epi film and the substrate is washed out. As expected, we observed that the upper temperature limit is dependent on the substrate doping concentration. The upper temperature limit is reached when the intrinsic carrier concentration of the film is about an order of magnitude below the extrinsic dopant concentration of the substrate. For a substrate with 6×10^{19} cm^{-3} dopants, the upper temperature limit is about 850 °C and the intrinsic carrier concentration in the undoped epi-film is about 4×10^{18} cm^{-3} at this temperature.

Repeatability and Reproducibility

The repeatability and reproducibility of FT-IR for epi-film thickness measurement is investigated in detail by a round robin test [67]. The round robin test, organized by the American Society for Testing and Materials (ASTM), which involved 21 different FT-IR instruments. In general, the results show that 92% of the instruments have a repeatability better than 1% (in terms of twice the coefficient of variation (2RS%)) for epilayer thicknesses in the 2.5-120 μm range. A small value for repeatability implied that most measurements are close to the mean. The reproducibility among the 21 instruments ranged from 9.99% (2RS%) on a thin (2.6 μm) epi-layer to 1.83%(2RS%) on a thick (117 μm) epi-layer.

For real-time applications, the repeatability and reproducibility of the moni-

toring technique must be evaluated to minimize the possibility of false alarms. We performed the measurement analysis on the E/FT-IR following the SEMATECH gauge study procedure [121]. For all measurements, the test wafer (silicon) has an undoped 7.30 μm thick epi-layer on a substrate doped by Arsenic, n^+, 0.0044-0.0048 Ω-cm, <100> orientation. The reference is the substrate without epi-layer. The gauge study procedure and result of the analysis is presented next. For this study, all of the E/FT-IR measurements are taken in-situ within the MS-CVD reactor (described in Chapter 6). The E/FT-IR setup is the same as that used for real-time applications (see Chapter 7.4.1). Each interferogram is collected with 16 cm^{-1} resolution and by spectral averaging 16 scans, which takes about 30 second.

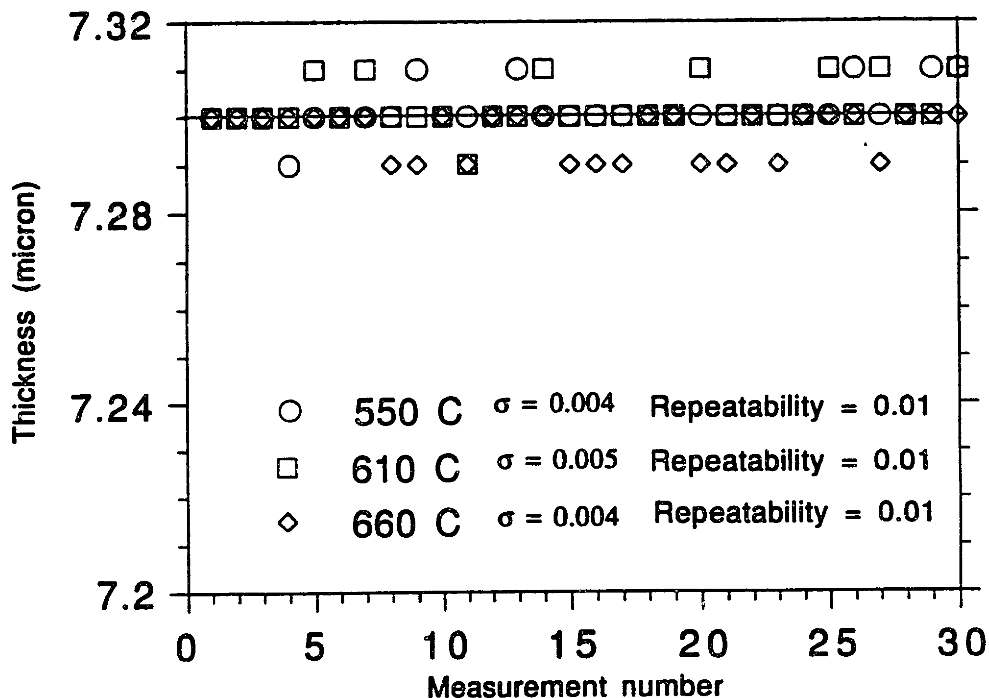

Figure 7.5: Repeatability of the E/FT-IR technique for epi-film thickness measurements

Repeatability Measurement: For repeatability evaluation, epi-film thickness is measured repeatly using E/FT-IR. All sources of variability must be eliminated, except for the inherent variability of the tool itself. Thirty measurements are made at three wafer temperatures by the same operator; using the same set-up

procedure, the same test wafer, the same environmental conditions; and over a short period of time (< 60 min.). The results are shown in Fig.7.5. Figure 7.5 shows that the repeatability of the E/FT-IR technique in terms of standard deviation (2δ) is 0.01 μm, in terms of coefficient of variation (2RS%) is about 0.1%, for all temperatures. For comparison, when the same test wafer is measured by conventional external mode reflection FT-IR, the epi thickness measurement yields a standard deviation of 0. A detailed comparison between E/FT-IR and R/FT-IR is given in the next section, and the reason that R/FT-IR has better S/N ratio is also explained.

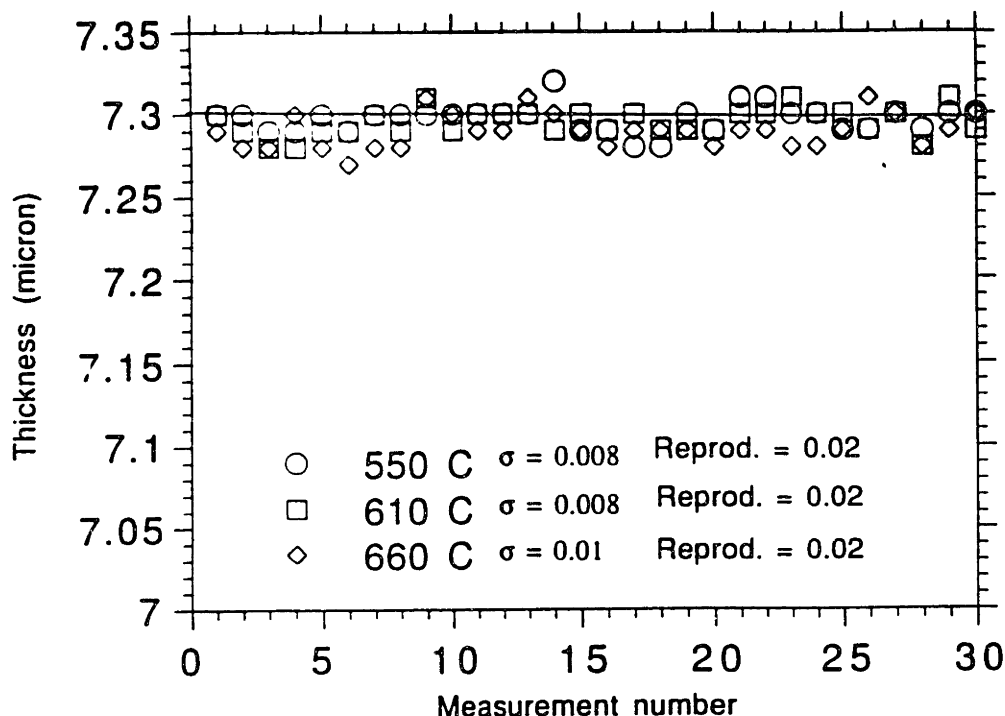

Figure 7.6: Reproducibility of the E/FT-IR technique for epi-film thickness measurements

Reproducibility Measurement: For reproducibility evaluation, epi-film thickness is measured repeatly using E/FT-IR. Again, thirty measurements are made at three wafer temperatures by the same operator. This is done using a different set-up procedure: load/unload wafer and wafer temperature ramp up, the same test wafer, different environmental conditions: chamber pressure and gas (hydrogen, or argon or vacuum), and during a long period of time (30 days). The results are shown

in Fig.7.6. Here, the reproducibility of the E/FT-IR technique in terms of standard deviation (2δ) is 0.02 μm, in terms of coefficient of variation (2RS%) is about 0.3%, for all temperatures.

Effect of Wafer Rotation

The commercialization of E/FT-IR in the manufacturing environment requires our understanding of the effects of wafer rotation. Because most of the commercially available epi reactor is designed with a rotation susceptor to enhance uniformity, it is impossible to rotate the wafer in our existing epi-reactor/ Thus, we decided to use an external reflection FT-IR setup. We believe a general understanding of the effects of wafer rotation on epi-film thickness can be applied equally well to the E/FT-IR case. Therefore, in order to investigate the effect of wafer rotation on the repeatability of FT-IR measurements, we built a rotation platform by modifying a 5.25 inch floppy disk drive. Figure 7.7 shows a schematic diagram of the measurement setup. A 4 inch wafer is mounted on the rotation platform and its rotation speed (ranging from 0 to 150 revolution per minute (RPM)) can be controlled by adjusting the voltage on the DC power supply (from 0 to 10 V). The stage has little vibration at low to moderate speeds. Thickness measurements are made at 0, 55, and 135 RPM.

The same SEMATECH gauge study guidelines are used for the repeatability measurement [121]. All measurements were taken by the same operator, using the same setup procedures, and under the same environmental conditions during a short period of time ($<$ 60 min.). A dozen measurements (interferograms) are made for each wafer at 0, 55, and 135 RPM. Each interferogram is collected with 16 cm^{-1} resolution and by the spectral averages of 16 scans which took about 30 second. Two test wafers are used for the measurements. Sample A has a 6.7 μm epi-film on a n^+ substrate with 0.01-0.02 Ω-cm resistivity. Sample B has a 7.15 μm epi-film on a n^{++} substrate with 0.004-0.005 Ω-cm resistivity. The reference wafers are of the same substrates but without the epi-film. The measurement results are summarized

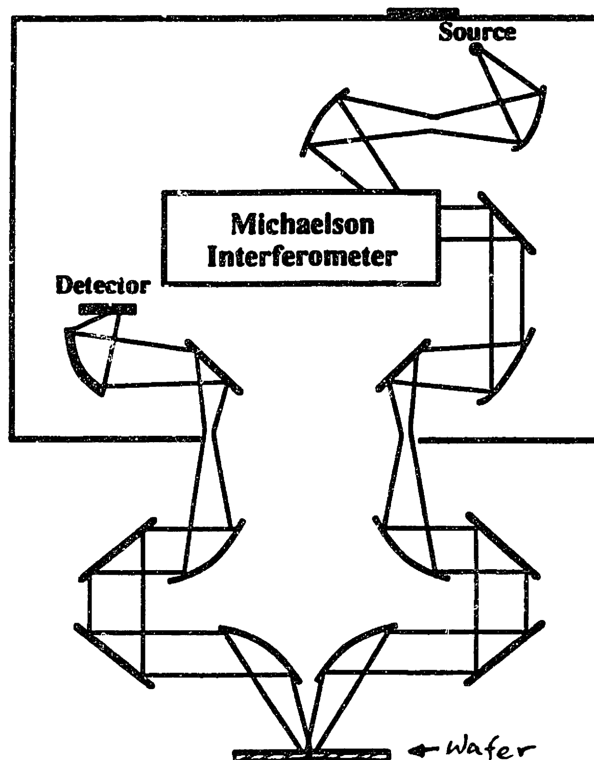

Figure 7.7: Schematic diagram of the setup for investigating the effect of wafer rotation on FT-IR film thickness measurements

in Table 7.1.

There are several observations can be made by looking at the processed results (see Table 7.1). The first is that at high rotation speeds (135 RPM), the signal to noise ratio is low. For sample A, vibrational noise resulting from high speed rotation overwhelms its weak side bursts. Incorrect thickness is randomly reported, thus the repeatability (2δ) is poor. Although the vibrational noise resulting from high speed rotation does not affect the measurement capability of sample B, the standard deviation of the measurements increased 5 times when comparing to measurements made at intermediate speeds (55 RPM). A small value for repeatability implies that most measurements are close to the mean. The reason we can still take measurements in sample B is that the difference in refractive index between the epi-film and the substrate in sample B (with a very heavily doped substrate) is larger, thus it has

Sample	Sample Speed(RPM)	Reference Speed(RPM)	Mean μm	Standard Deviation (δ)	coefficient of variation (2RS%)
A	0	0	6.71	0.0035	0.1%
	55	0	6.74	0.008	0.24%
	55	55	6.72	0.012	0.36%
	135	0	50.95	12.28	50%
	135	135	45.98	20.53	90%
B	0	0	7.16	0.00	0%
	55	0	7.17	0.0037	0.1%
	55	55	7.18	0.0049	0.14%
	135	0	7.19	0.027	0.75%
	135	135	7.20	0.034	0.89%

Table 7.1: Effect of wafer rotation on the repeatability of epi-film thickness measurement

stronger side bursts when comparing to sample A and to the noise. For the same reason, the measurement repeatabilities for sample B are better than those of sample A at all corresponding rotation speeds. At intermediate speeds (55 RPM), the rotation platform is sufficiently stable. Only a small amount of noise is introduced to all measurements. We observed that the repeatability got worst when the rotation speed of the sample increased. Moreover, it is anticipated that a reference interferogram collected when the reference wafer is stationary provides better repeatability than when the reference wafer is rotating because the latter has more noise. This is indeed observed.

7.3.3 Comparison of E/FT-IR and R/FT-IR for Film Thickness Measurement

A typical film thickness measurement procedure for both techniques is as follows: First, a reference interferogram is taken using a blank substrate (or a substrate with a thick film), and the center burst is kept for later subtractions; second, an interferogram of the sample is taken; third, the reference IG is then subtracted from the sample IG to suppress the center burst. The center burst can be eliminated completely if the reference substrate and the sample substrate has similar materials characteristics. By measuring the distance between the two side bursts, and assuming a constant refractive index for Si (e.g.n=3.42), the film thickness can be calculated from :

$$d = \frac{\Delta}{2n\cos\Theta} \tag{7.8}$$

where Θ is the angle of incident or emission angle for R/FT-IR and E/FT-IR, respectively. Therefore, in order to obtain the film thickness, the most important factor is to be able to identify the side bursts clearly. From equations (10) and (15), the side bursts is the inverse Fourier transform of the third term in these equations. The interference term can be rewritten as:

$$I_{C_e} = T_{2,1}^2 R_{1,0} R_{1,2} T_{0,1}^2 e^{-2\alpha\Delta} I_{eo} \cos k\Delta \tag{7.9}$$

$$I_{C_r} = R_{0,1} T_{0,1} R_{1,2} T_{1,0} e^{-\alpha\Delta} I_{ro} \cos k\Delta \tag{7.10}$$

Obviously, the magnitude of these two equations determines the intensity of the side burst; and the phase of these equations determines the position of the side burst. In both cases, the side bursts are located at the same places, thus the film thickness measurements are consistent. This is indeed observed and shown in Fig.7.8. In order to be able to identify the side bursts, the magnitude of these equations must be

greater than the background noise. This means, that $R_{1,2}$ must not be zero, hence the refractive index of the film and substrate must be different; Since $\alpha\Delta$ must be small, hence the absorption in the film must be small; and lastly, the source intensity must be high. With all these conditions satisfied, an acceptable signal to noise ratio of the side burst can be obtained, therefore film thickness measurement can be performed. From our experimental data, we observed that the R/FT-IR interferogram has better signal to noise ratio than E/FT-IR. This observation can be explained by these equations. In the reflection mode, the source temperature is more than 1000 °C; in the emission mode the source temperature is much lower and the source emissivity is also smaller, therefore the source intensity I_{oe} is much smaller than I_{or}. Moreover, in the emission mode, the IR radiation from the substrate has to travel through the epi-layer one more time comparing to that in the reflection mode. Consequently, absorption by the epi-film is more significant, since in the emission mode, the absorption is twice of that in the reflection mode. In both cases, the absorption coefficient increases as temperature increases. Furthermore, the film/substrate interface quality has a bigger effect in the emission mode because the IR beam interacts with this interface twice. Consequently, R/FT-IR has better repeatability and reproducibility than E/FT-IR. However, the E/FT-IR is much easier to implement and is also robust (relatively insensitive to surface roughness and flatness). It is an attractive technique for high temperature process monitoring like silicon epitaxy, therefore an demonstration of real-time *in-situ* epi-film thickness monitoring during a CVD process using E/FT-IR is presented next.

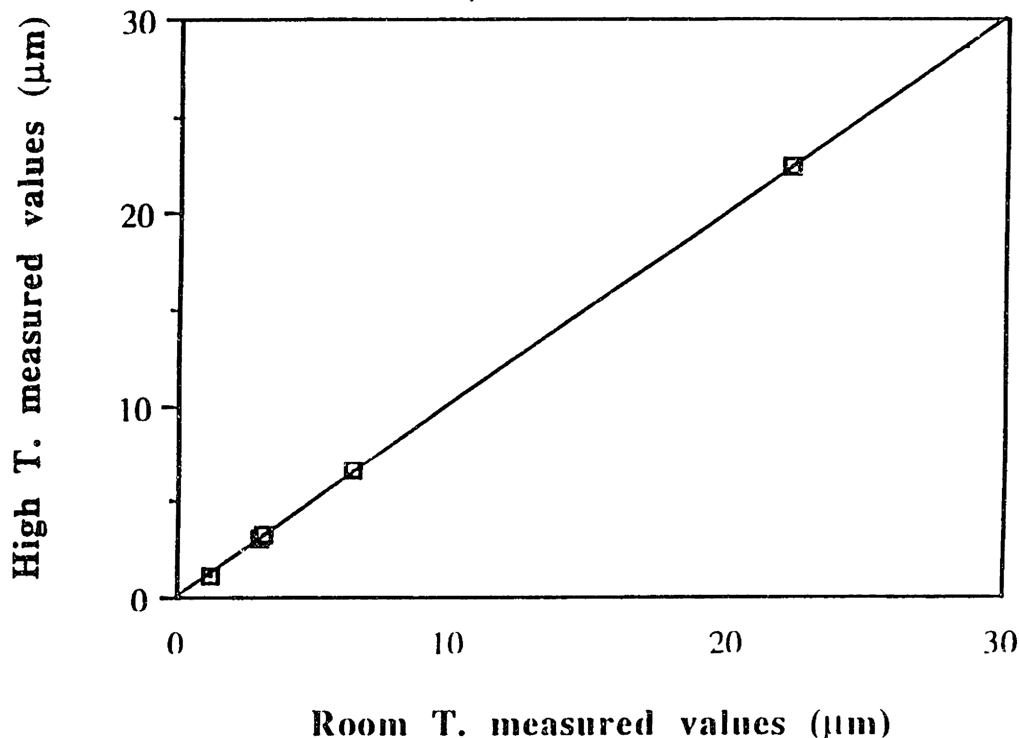

Figure 7.8: Correlation of high temperature E/FT-IR measured values with room temperature R/FT-IR measured values [64].

7.4 Real-time Applications of E/FT-IR in Silicon Epitaxy

Although FT-IR spectroscopy using an external IR source is commonly and widely used in the semiconductor industry [65], it is only used for *ex−situ* measurements (i.e., the measurement is performed outside the process chambers), and is difficult to adapt for *in-situ* measurements. Compared to the conventional reflection FT-IR technique, the infrared emission technique does not need an external light source. Therefore, it is easier to implement, and it is relatively less sensitive to surface roughness and flatness. Moreover, it is robust against vibration, rotation and misalignment of the wafer. Thus, it is well suited for *in-situ* monitoring of rotating wafers in production equipment. Consequently, emission FT-IR spectroscopy has significant potential as a real-time *in-situ* process monitor.

7.4.1 E/FT-IR Implementation

The Fourier Transform Infrared (FT-IR) spectrometer used in the experiment is made by the Digilab division of Bio-Rad. The Digilab Michelson interferometer is equipped with an emission port intended for emission Fourier transform infrared spectroscopy.

The E/FT-IR arrangement is shown on Figure 7.9. The wafer is held in front of a resistive/radiant heater. The radiation beam is collected at a 45 degree angle from the surface norm of the wafer. A KBr window is used for transmission of IR radiation from the heated wafer. The two ellipsoidal mirrors with the same focal length are used to focus so that only radiation from a small point near the center of the wafer is collected and analyzed. The wafer is placed one focal length away from the top ellipsoidal mirror. The collimator inside the interferometer is also placed one focal length away from the second ellipsoidal mirror. These two mirrors are separated by two focal lengths. This arrangement ensures that the image collected on the heated wafer is reproduced at the collimator.

Film thickness measurements are obtained from the interferogram collected by the FT-IR spectrometer. Each interferogram is collected with 16 cm^{-1} resolution and by spectral averaging of 16 scans, which takes about 30 seconds. All depositions are performed on a substrate with an existing epi, typically (unless specified), the existing undoped epi thickness is about 7 μm. The substrates are doped by Arsenic, n^+, 0.0044-0.0048 Ω-cm, and <100> orientation.

On the equipment side, *in-situ* monitoring and feedback control of process pressure and wafer temperature are realized (See Chapter 6 for details regarding the equipment). A capacitor monometer is utilized for *in-situ* chamber pressure measurements, data are fed-back to a control gate valve which regulated the pumping speed and maintaining a preset process pressure; A thermocouple is used for wafer temperature measurements, the measurements are fed-back to regulate the heater

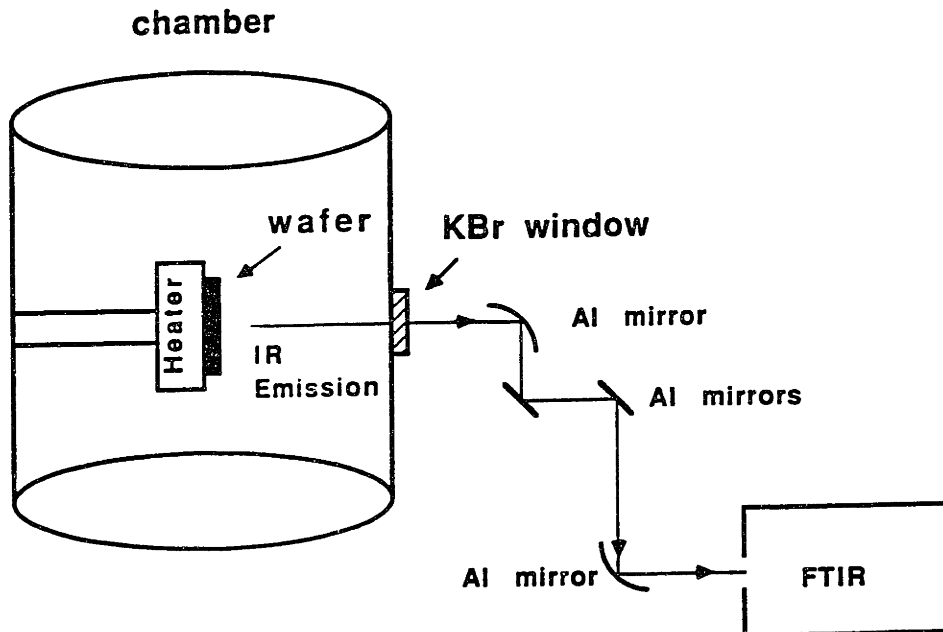

Figure 7.9: A drawing of the E/FT-IR setup

power supply and maintaining a preset wafer temperature. The focus here is in the real-time *in-situ* monitoring of material properties and the processing environment during silicon epitaxy, and in the adaptive control schemes to feed these parameters back to the process controllers. In the next section, results from an real-time *in-situ* film thickness monitor that employs a new emission fourier transform infrared spectrometer are presented.

7.4.2 E/FT-IR Demonstration

The real-time film thickness measurement was demonstrated by depositing a film on a substrate with an existing epi-film. By monitoring the shift in the side bursts as a function of time, the growing film thickness can be found.

The E/FT-IR technique has been applied to measure film thickness ***in-situ*** and in real-time during the deposition processes. A film was deposited on a 3 μm epi wafer (substrate is n-type doped with resistivity equal to 0.001-0.002 Ω-cm; the existing epi layer is also n-type with resistivity equal to about 0.5 Ω-cm). The growing film thickness is the total measured film thickness minus the initial epi-film thickness. Figure 7.10 shows the real-time film thickness measurements during a thermal CVD process at a temperature of 650 $°C$. The wafer is cleaned simply by dipping it in HF (10:1) solution without rinsing before introducing it into the CVD reactor. Deposition was carried out at a pressure of 2 mTorr by introducing 40 sccm of pure silane. We have observed the transient behavior of this process. The slope of the curve gives us the growth rates, and we notice that the initial growth rate is slower. Although the reasons for this change in growth rate is unknown at present, we believe it may be related to perturbations in the deposition parameters. In addition, the real-time *in-situ* monitor can be used for endpoint detection and control. For example, if a 0.27 μm epi-layer is desired, the deposition process can be terminated when the E/FT-IR gives a 0.27 μm epi-film thickness reading. For an even more precise endpoint control, the real-time film thickness measurements were used to extrapolate a real-time growth rate, therefore process endpoint was predicted in real-time. Thickness information was fed-back in real-time to precisely control the film thickness. The final thickness measurement was confirmed by *ex situ* FT-IR and high resolution cross-sectional transmission electron microscopy (HRXTEM), which gave measured film thicknesses of 0.26 μm and 0.3 μm, respectively. The E/FT-IR technique is particularly suited for real-time process monitoring, as it allows repeatable, fast, and accurate (0.01μm precision) measurements of film thicknesses.

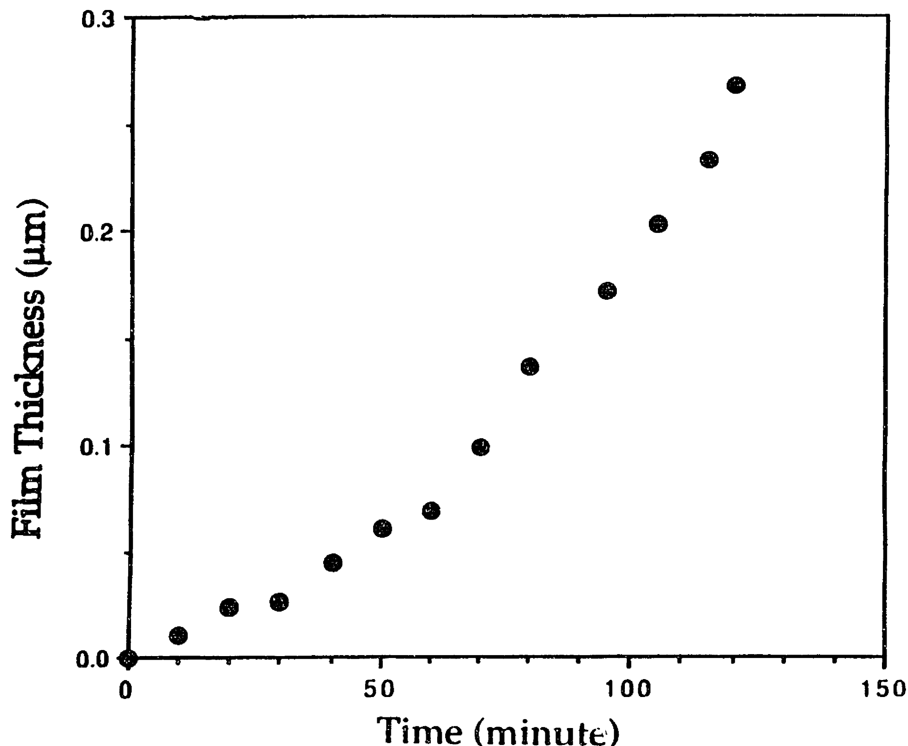

Figure 7.10: Real-time thickness monitoring during a thermal CVD process

7.4.3 E/FT-IR in Process Research

Very low temperature (< 800 °C), very low pressure (< 10mT), CVD of silicon and silicon germanium has gained increasing importance for device fabrication. The commercialization of UHV/CVD technology by IBM is a prime example. Although the fundamental understanding of the conventional high temperature and high pressure CVD processes and their models have been well developed, they may not be directly applicable here. Comfort and Reif have reviewed the field of very low temperature chemical vapor deposition (VLPCVD) of silicon and polysilicon in their epitaxial growth kinetic studies [85, 86]. They have constructed a model. Using their model, they have qualitatively predicted the effect of temperature on reaction efficiencies and growth rates. Additionally, they looked at the effect of pressure on fractional silane surface coverage. Although their predictions were meaningful, the lack of experimental data prevented them from performing any quantitative analysis. Only until

recently, the growth rates have been re-examined and a quantitative model has been proposed by D.W. Greve [89, 90]. The model was based on a recent experimental study of silane decomposition [91]. Under steady state, and in the temperature and pressure region of interest, a two-step reaction sequence was proposed as follows:

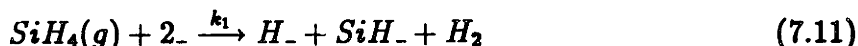

$$SiH_4(g) + 2_ \xrightarrow{k_1} H_ + SiH_ + H_2 \tag{7.11}$$

$$SiH_ \xrightarrow{k_2} \frac{1}{2}H_2(g) + _ + film \tag{7.12}$$

where "_" indicates a surface site and H_ represents a hydrogen atom on a surface site. Using this two-step reaction, the growth rate R[atoms/cm2sec] at high temperatures, is expressed as:

$$R = Nk_1 Z_s \Theta^2 \tag{7.13}$$

where N = 6.78 x1014 cm^{-2} is the number of surface sites/cm2. The dimensionless number Nk1 is the reactive sticking coefficient for a bare surface. Z_s is the impingement rate of silane on the surface. The silane impingement rate is known from the silane partial pressure; Θ is the fraction of vacant sites on the surface. Under high temperatures, $\Theta \approx 1$.

For low temperatures, the growth rate is expected to be hydrogen desorption limited ($\Theta \approx 0$) and the growth rate is limited by:

$$R = \frac{Nk_2}{3} \tag{7.14}$$

From Figure 7.11, we can see that the model provides a good fit to experimental growth rate data at various deposition temperatures and reactant flow rates.

The simulation results, their experimental data, and ours are in good agreement as shown in Figure 7.11. From real-time thickness measurements, growth rates can be extracted. By varying a process parameter (e.g. temperature, pressure, or gas composition), the corresponding change in growth rate can be obtained in real-time (within an experiment).

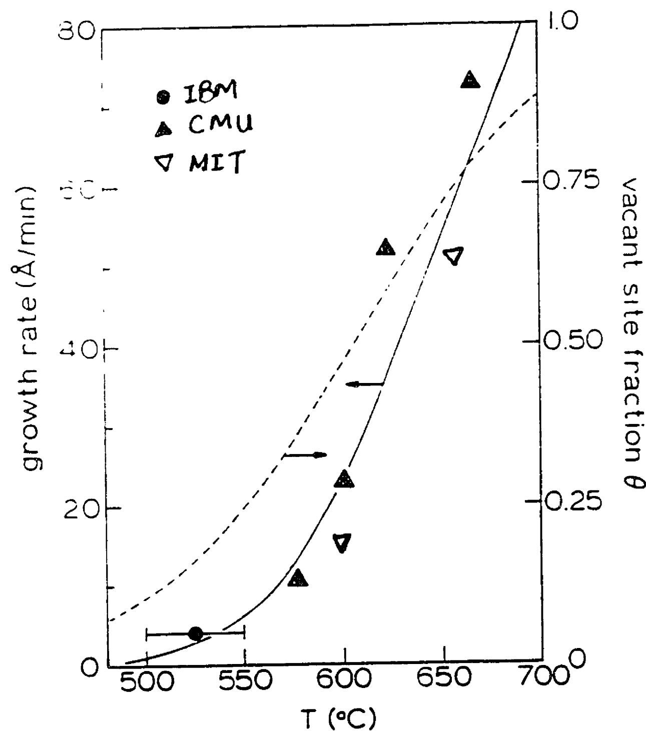

Figure 7.11: Growth rates of silicon as a function of temperature.

Models are critical for equipment/process design and equipment/process control. Model based control is important in cluster tool environment. In case real-time sensor is not available, an accurate model is critical to the success in controlling the process. To establish validated equipment/process models, experimental reactions/reaction rate kinetics and physical constants are needed. Real-time *in-situ* monitors can be used to obtain accurate rate constants to fine tune the model. In the case of low temperature and low pressure CVD, although the reactor geometry and technology (hot wall vs. cold wall; batch vs. single wafer) are different, the reaction mechanism may still be the same. This is confirmed by the growth rate comparison in Fig.7.11. Under similar process condition, a good agreement in growth

rates are observed. Consequently, knowledge learned in our reactor using real-time *in-situ* monitor may be used to fine tune the model for controlling the commercially available UHV/CVD reactor/process in manufacturing. This understanding would form a knowledge base for reliable new reactor/process design and design trade-offs.

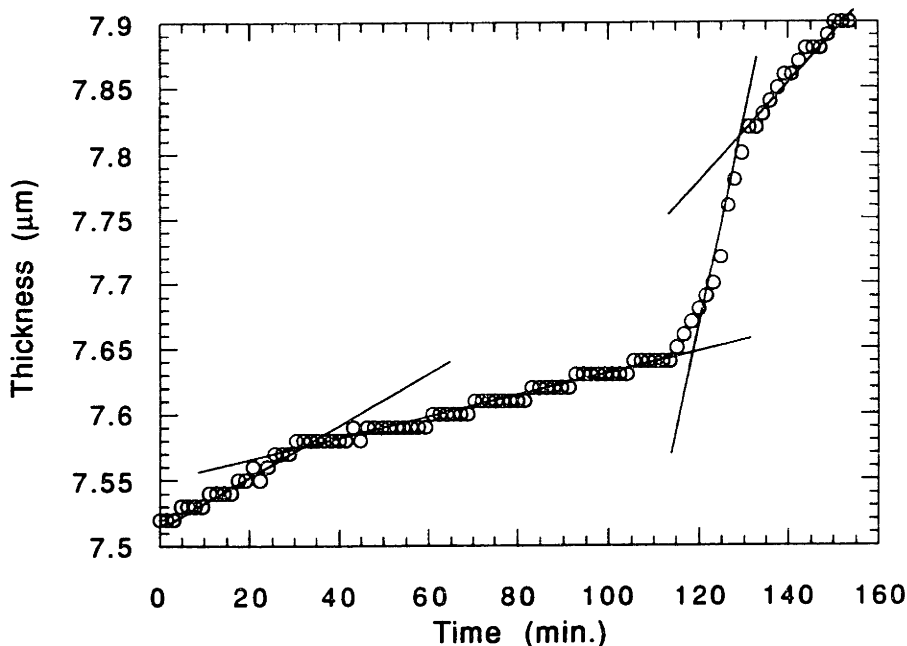

Figure 7.12: Real-time in-situ monitoring of growth rates for growth kinetic studies

An example of kinetic study employing the real-time E/FT-IR is shown in Figure 7.12. During this experiment, process parameters are changed, and the changes in process parameters are reflected in changes of growth rates. Several rate constants can be obtained from this experiment. The experiment can proceed longer if the data are not statically significant for the updating or validating of the model. For this experiment, the wafer is one of those specified in section 7.4.1, and the initial process conditions are specified in Table 6.1. The process temperature is fixed at 660 °C through out this experiment. After one hour of growth, 10 sccm of H_2 is introduced to the reactor, as expected the growth rate is reduced as a result of silane dilution. After another hour of growth, hydrogen is turned off, silane flow rate is increased

from 10 to 20 sccm, and the chamber pressure is changed from 1 to 4 mTorr. A drastic increase in growth rate is observed. After 20 minutes, the silane flow rate is reduced to 10 sccm while keeping the pumping speed a constant, the resulting chamber pressure is halved (2 mTorr). Although the pumping speed is kept at a constant, the growth rate is decreased as the pressure decreases. The observations of growth rate reductions by hydrogen dilution and pressure reduction, suggested that growth rate of silicon is proportional to silane partial pressure. This agrees with the rate equation above. At the temperature of 660 °C, hydrogen on silicon surface is desorbed so that the fraction of available vacant sites on the surface is approaching unity. Thus the primary rate limiting factor is the silane pressure.

Another example is the growth rate dependence on starting materials. Figure 7.13 (a) show real time measurement results from depositions on different substrates. Two observations can be made from this figure. First, the growth rate is clearly slower on <111> silicon substrate compare to <100> substrate. Second, an incubation time as long as 20 minutes was observed. The existence of different growth rates for various crystallographic orientations is well recognized. The observation that growth rates on (100) surfaces are higher than those on (111) surfaces for identical temperatures and silane partial pressures is consistent with previously observed surface controlled growth rate studies. The faster growth rates on (100) surfaces are attributed to either a higher density of adsorption/incorporation sites or to atomic bonding arrangement favoring growth in the (100) planes. MBE experiments involving direct incorporation of an incident atomic silicon demonstrated that direct silicon incorporation is independent of substrate orientation from 450 to 900 °C[92]. This suggests that inhibition of silicon incorporation at step edges cannot account for the observed variation in growth rates. This implies that the growth rate variations are associated with the differences in silane adsorption or decomposition on (100) and (111) surfaces. But it is not possible to differentiate these effects at this point. The inhibition of silicon nucleation during silane decomposition on oxide has been observed both in our present

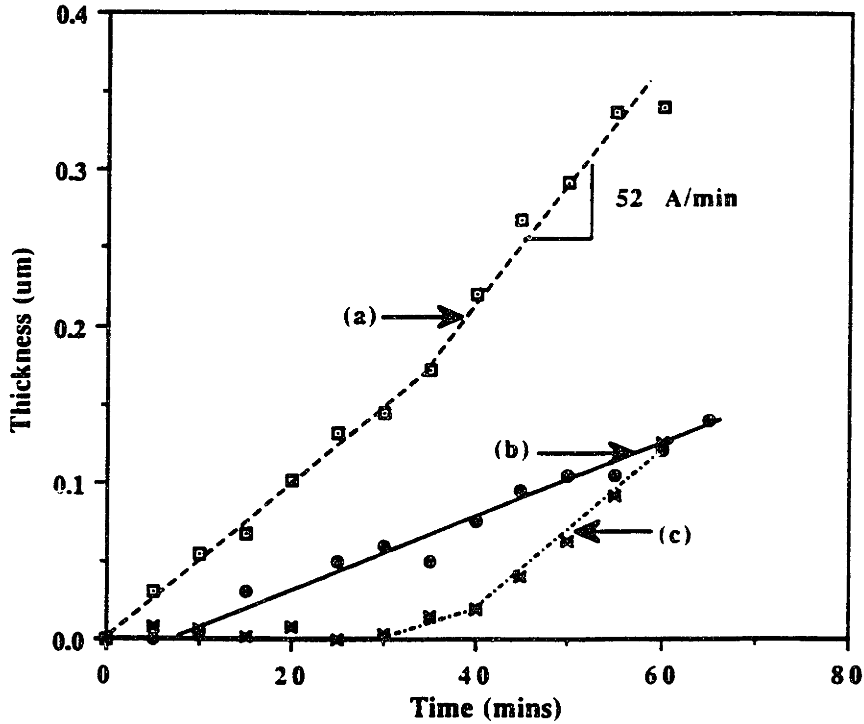

(a) Data obtained by real-time E/FT-IR technique for a 660 °C deposition [132].

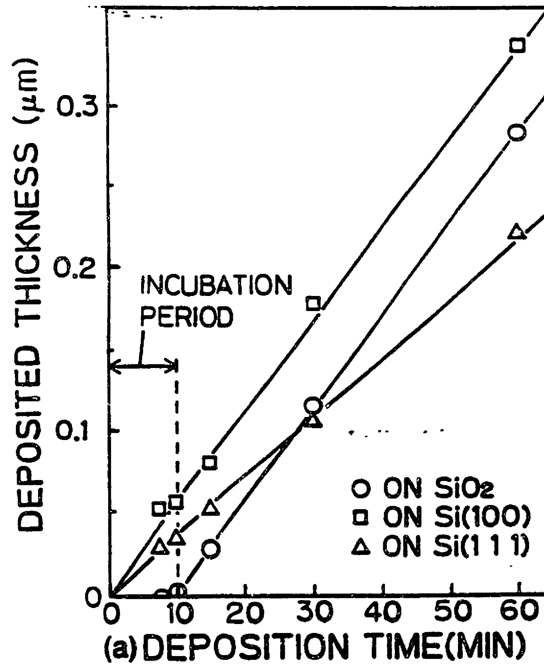

(b) Data reported by Murota for a 700 °C deposition [93].

Figure 7.13: Real-time in-situ monitoring of growth on various substrates

reactor, our previous reactor[97], and other researchers [93]. This inhibition is most evident under very low pressure conditions which suppress nucleation by reducing the density of adsorbed silane molecules. Indeed, it was observed that the incubation time was decreased as the silane partial pressure was increased (see Table 7.2). Table 7.2 summarized the incubation time at various pressures for VLPCVD at 800 °C[94].

Pressure of SiH_4/ H_2 (mTorr)	Incubation time (min.)
3.5/0	2.15
6/0	1.2
11/0	0.75
2/7	7.75
3.5/7	3.85
6/7	1.9

Table 7.2: Summary of incubation time for VLPCVD at 800 °C[94]

A similar study was reported in [95] for deposition at 700 °C(See Figure 7.13(b)). The published article is centered on these observations which require fifteen growth experiments in addition to the predeposition cleaning and the post-deposition characterization efforts. With the availability of real-time *in-situ* monitors, all these efforts can be reduced to three experiments without the need of post-deposition characterizations. This clearly demonstrated the power of real-time *in-situ* monitors in process research and development.

From the above studies, we conclude that real-time *in-situ* monitor offers several distinct advantages in process research:

1. Rapid feedback on growth rates can be obtained in real-time during one run (or fewer runs). Hence, reduces time to develop, update, and validate process

models.

2. Measurement noise due to run to run variations (e.g. materials variation, initial condition variation, equipment drift, process drift, etc.), can be reduced, since data are obtained in one run (or fewer runs). Hence, more accurate kinetic rate constants makes the model more realistic.

3. Process flexibility can be increased by rapid tuning of models for new or different processes.

From real-time *in-situ* film thickness data, two important parameter can be obtained. They are growth rates and incubation times. From growth rate, one can understand the process kinetics, improve the accuracy of the process models, thus lead to efficient process development, optimization and control. In addition, since the growth rate is critically dependent on process parameters, any variation in the process will be reflected in changing growth rates. Consequently, process monitoring and control can be achieved through the monitoring of growth rates. From incubation time, one can obtain a better understanding of the kinetics of polysilicon deposition. The measurements and understanding of incubation time allows one to optimize selective epi deposition, monitor predeposition cleaning, and finally control film quality. Different applications of both growth rates and incubation time measurements in process monitoring, control, and development, are described in details in the next two sections.

7.4.4 E/FT-IR in Monitoring and Control of Silicon Epitaxy

Real-time Process Monitoring

As pointed out in the last section, the growth rate is critically dependent on process parameters. Any variation in the process will be reflected in changing growth rates. Consequently, process monitoring and control can be achieved through the real-time growth rate data. The capability of E/FT-IR for process monitoring is illustrated in the following examples. Figure 7.14(a) shows the real time monitoring result of an experiment. For this experiment, the initial cleaning and deposition conditions are specified in Table 6.1. During this experiment, we intentionally change the deposition temperature from 600 to 650 °C after 60 minutes of deposition. A change in growth rate is observed immediately. As expected, the growth rate is increased when increasing the deposition temperature. Figure 7.14(b) shows the real-time monitoring of another experiment under the same initial process conditions, except that the process temperature is kept constant at 650 °C through out the experiment. Here, the source gas is diluted with hydrogen after 40 minutes of deposition. As expected, a slow down of growth rate is observed immediately.

The stair case like thickness measurement is due to the slow growth rate and precision of the E/FT-IR thickness measurement. The growth rate is typically 2 nm/min at 600 C, it will take five minutes of deposition time for the E/FT-IR (with a precision of 10 nm) to pick up a change in film thickness. With a sampling rate of about 1.5 minutes, we can see several data points with the same thickness, however, this does not mean the film is growing in steps. Oversampling of film-thickness during a experiment can show the real-time repeatability of the E/FT-IR measurements. For the samples we were using for our experiments, the repeatability is excellent. When the growth rate is slow enough, we can even observe (at the transition point when

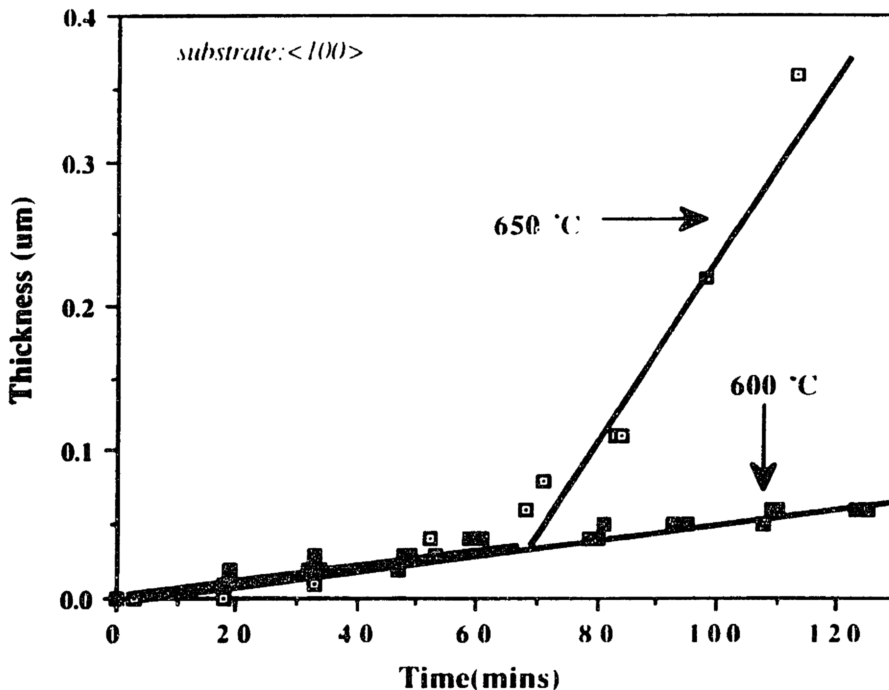

(a)

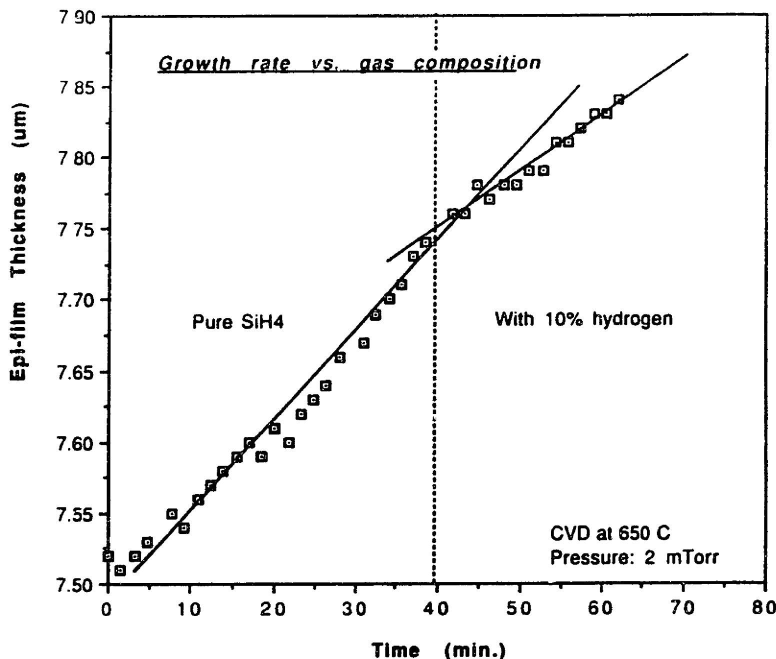

(b)

Figure 7.14: Real-time in-situ monitoring of process variations in a) temperature, b) gas composition

the film thickness change is about 5 nm) the E/FT-IR measurements jumping up and down, then stabilizing at the next level. Measurement noises from real-time sensors may result in adverse effect in process control. The oversampling technique also allows us to check the sensor repeatability in real-time. In addition, by knowing the sensor repeatability of each run, we can easily determine the reliability of the real-time measurements and implement a filter with tight limits (depend on estimate growth rate and sampling time) to eliminate measurement noises. This reduces the chance for false alarm.

From the two examples, we found that the real-time growth rate measured by the E/FT-IR is responsive to variations of process parameter(s) (e.g.temperature, pressure, and gas composition). This information can be used for real-time process monitoring. A growth rate window for the process can be defined such that when the growth rate is outside the limits of the window, an alarm will be signaled. The operator or the computer can check for possible malfunction and determine if the process should be terminated. The real-time growth rates, which is a signature of the process, are recorded in the computer. This information can be used for real-time control (feedback and feedforward). It can also be used for Run-by-Run statistical process control.

Epi-layer Thickness Control

The closed loop control was implemented on the Labview (National Instruments) platform using a Macintosh computer (Quardra 900 model with a Motorola 68040 microprocessor). Real-time thickness data were extracted from the Bio-Rad Digilab's computer (SPC-3200 workstation) through a standard RS-232 communication port. Two control algorithm were used: 1) first past the post (FPP) method; 2) linear forecasting. Mathematical models and other control algorithms, such as time series analysis and neural networks, were evaluated and described in detail in [135]. The

FPP algorithm was the most obvious approach for controlling the film thickness. The FPP algorithm monitors the thickness continuously. Once a measurement is on or exceeds the target, the process will be terminated automatically. The termination step was carried out using a digital input/output (I/O) board (Lab-NB board from National Instruments) to turn off all process gases, mass flow controllers and temperature controller. The E/FT-IR with 0.01μm precision resulted in a control limit of 0.005 μm using the FPP method. The linear forecasting algorithm assumes that the growth rate of silicon follows a linear path. The growth rate was determined and continuously updated by taking the real-time measured film thickness data and performing a linear regression on them. The process end-time was estimated and updated from the growth rate in real-time. When the growth rate was truly linear, the method reduced the effect of E/FT-IR measurement noise and improved the control limit to 0.003μm.

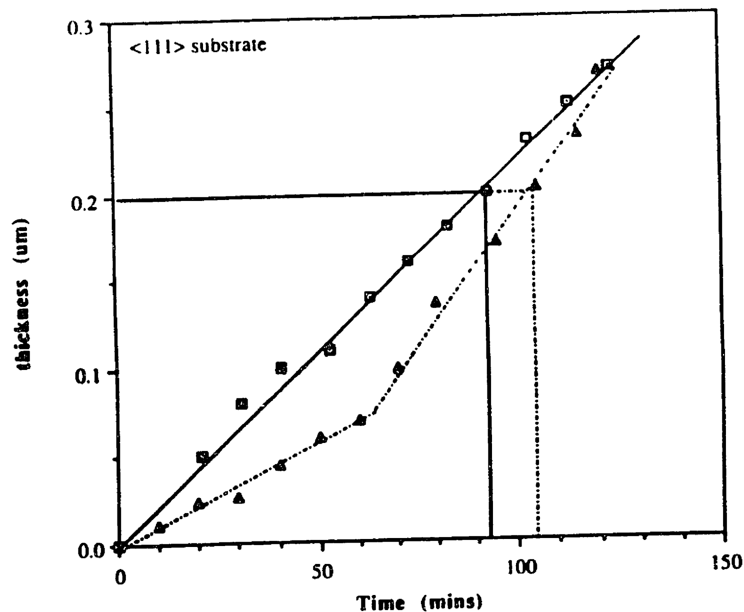

Figure 7.15: Precise closed-loop end-point control using real-time epi-film thickness data

In Figure 7.15, real-time monitoring of two experiments with the same process conditions are shown, and yet the growth rates are different. This illustrates the result of process variation in real-time. The variation in growth rates is caused by fluctuation in the silane mass flow controller. The deviation can be said to be within the process window and deposition is allowed to continue until the desired output thickness is reached. This is a demonstration of precise process end-point control by real-time monitoring of the process, thereby compensating variations within a run. Whereas, in current industrial practices, an average growth rate is obtained by calibration runs. The conventional process control is accomplished by timing the process based on the target film thickness and the growth rate. In many cases, the growth rate is not a constant through out the process. The existence of incubation periods, initial growth transients, process parameter fluctuations, and process/equipment drifts, will all affect the growth rate. As the target film thickness decreases, the epi-film thickness control becomes more challenging. The conventional method may not be able to meet some of the more stringent requirements. Considering the same experiments, however, now suppose the target film thickness is 0.2 micron. Using the average growth rate method for process end-point, the process would be terminated at 92 minutes. At this time, the film thickness is only 0.17 micron, which is under the target by about 15%. Thus, real-time monitoring of epi-film thickness by E/FT-IR, has opened up a new avenue for precise end-point control. This reduces run-to-run process variations as well as target film thickness variations.

7.4.5 E/FT-IR in ECR Hydrogen Plasma Predeposition Wafer Cleaning Process Optimization

The ability to control the wafer surface condition is critical to silicon epitaxy. An atomically perfect surface is important to defect-free growth and high interface quality. in-situ plasma pre-deposition cleaning was proven to be a necessity, and pio-

neering work has been done using a radio frequency (RF) generated plasma in our group. Recently, plasmas generated by Electron Cyclotron Resonance (ECR) have attracted much attention in microelectronics fabrication for both thin film deposition and plasma etching. Electron Cyclotron Resonance (ECR) plasma was chosen because it has many advantages over conventional radio frequency plasma. ECR plasma offers high excitation rate, low plasma potential and high efficiency. ECR plasma enables processing below 1 mTorr, consequently minimizes recombination reactions among the species, utilizes neutrals and ionic species generated in plasmas more effectively, and reduces wafer contamination. Additionally, low plasma potential leads to the reduction of damage.

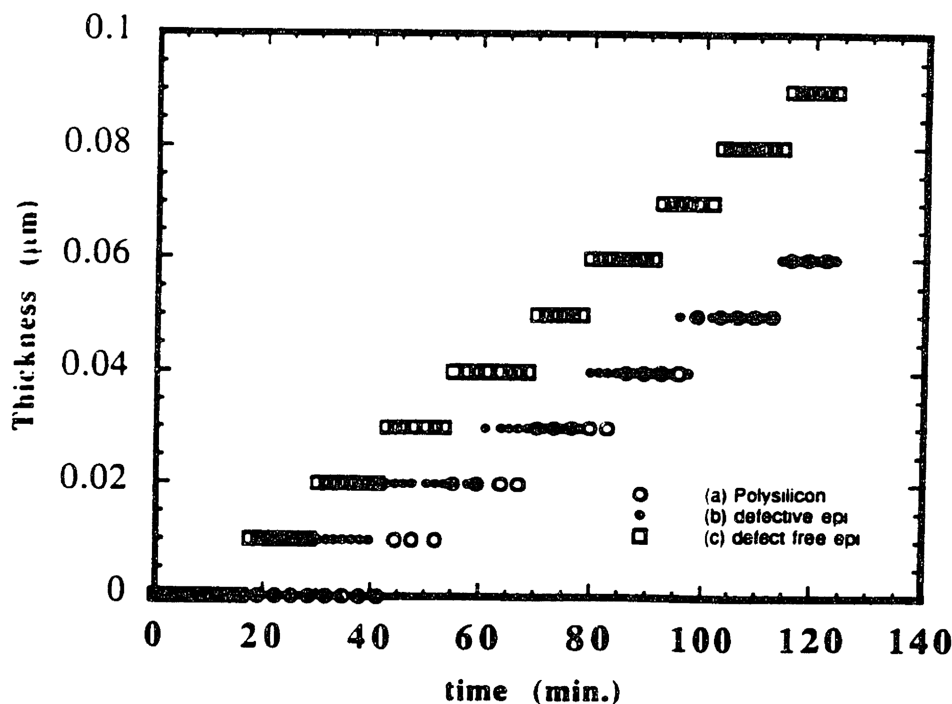

Figure 7.16: Real-time in-situ monitoring of growth incubation time and growth rate during a CVD process

In addition to real-time *in-situ* monitor and control of epi film thickness, we have observed changes in growth rates and incubation times resulting from various predeposition wafer cleaning conditions. By real-time monitoring of incubation time

and growth rate, we are able to obtain qualitative information about the effectiveness of the predeposition wafer cleaning process, and to assess the quality of the depositing film in real-time.

	Film Q	Rate (Å)	u-power (W)	mag. 1 (A)	mag. 2 (A)	DC bias Voltage	cleaning temp.	cleaning time(min)	cleaning pressure	cleaning flow rate
R0003	Poly	10	750 - 010	165	120	0V	600°C	10	8mT	80sccm
R0004	Poly	10	750 - 000	165	120	0V	room.	5	8mT	80sccm
R0006	E	20	300 - 000	150	120	10V	600°C	5	1mT	20sccm
R0007	Poly	14	300 - 000	150	110	0V	room.	5	1mT	20sccm
R0008	Epi	16	300 - 000	150	125	0V	600°C	5	1mT	20sccm
R0011	D-E	6	775 - 025	150	110	10V	600°C	10	8mT	20sccm
R0012	E	10	750 - 202	150	120	10V	room.	5	8mT	80sccm
R0014	D-E	7	Ex-situ	clean	only	by	HF dip.			
R0015	E	20	300 - 070	150	120	10V	600°C	20	1mT	20sccm
R0016	D-E	16	300 - 054	150	120	10V	600°C	10	1mT	20sccm
R0019	D-E	7	655 - 236	150	120	0V	600°C	5	2mT	20sccm
R0020	Poly	14	655 - 242	150	120	0V	600°C	10	2mT	20sccm
R0021	Poly	13	655 - 255	150	120	10V	600°C	5	2mT	20sccm
R0023	Poly	10	655 - 255	150	120	10V	room.	10	2mT	20sccm
R0028	Epi	64	300 - 045	150	120	10V	660°C	10	2mT	20sccm
R0031	E	50	300 - 035	150	120	10V	660°C	5	1mT	20sccm
R0036	E	17	300 - 028	150	120	10V	600°C	5	1mT	20sccm
R0039	E	17	300 - 280	150	120	10V	rt to 600°C	6	1mT	20sccm

Table 7.3: Summary of plasma cleaning conditions and growth rate results.

Figure 7.16 shows the real-time thickness monitoring results of three depositions performed under the same deposition conditions (as indicated in Figure 7.16). Figure 7.16(a) shows an incubation time of 30 minutes resulting from a deposition on a native oxide covered silicon surface. Subsequent cross sectional transmission electron microscopy (XTEM) confirms that the deposited film is polyscrystalline silicon (see 7.17(a)). Figure 7.16(b) does not show an incubation time; however, the growth rate is slower compared to that in Figure 7.16(c). The corresponding XTEM picture

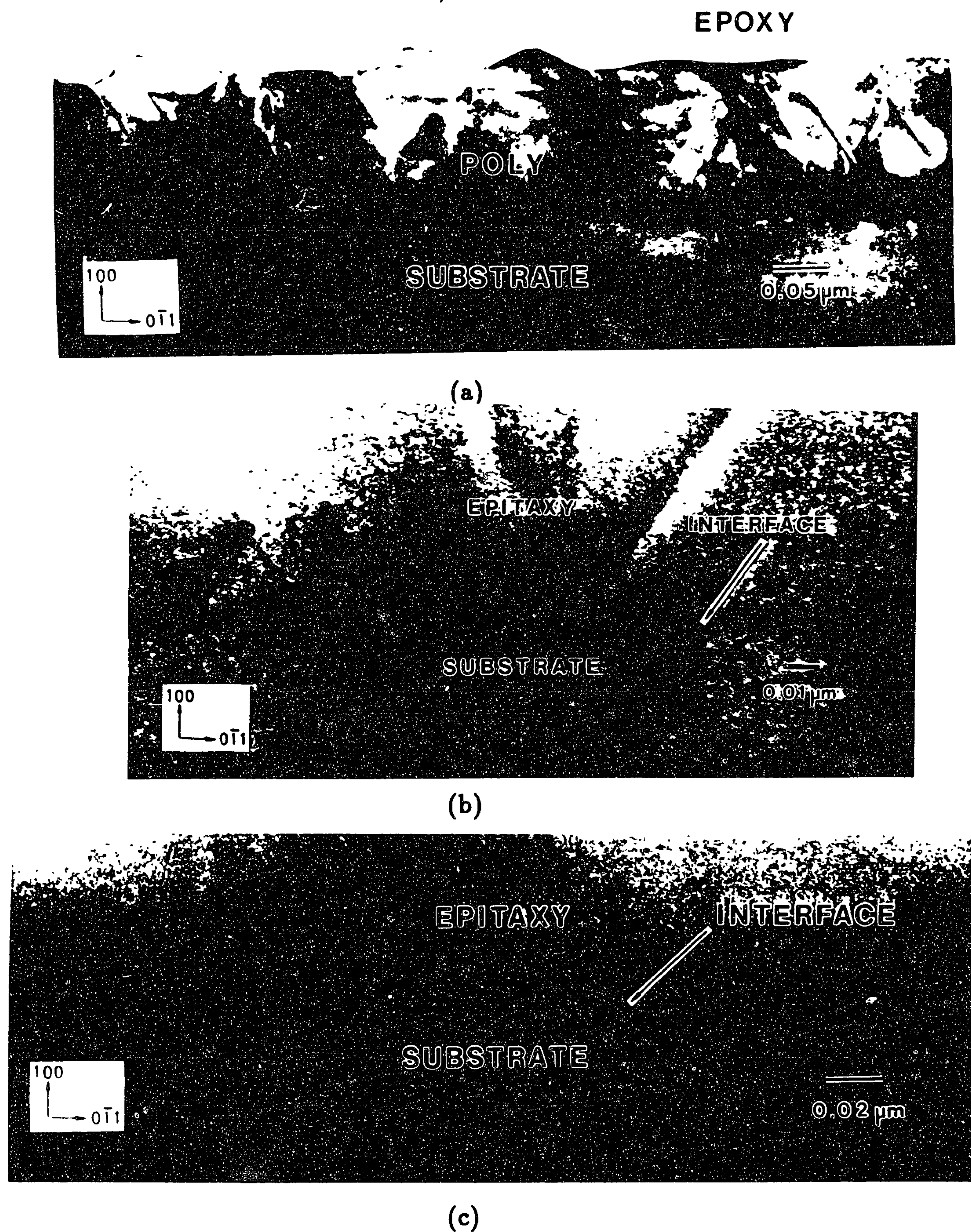

Figure 7.17: XTEM picture of (a) a Poly-Si film, (b) a defective epi-film, (c) a defect free epi-film.

(Fig.7.17(b)) shows that the film grown with slower growth rate is a defective epi film. Figure 7.16(c) showed that a defect free epi-film is deposited after ECR hydrogen plasma cleaning (Fig.7.17(c) shows the corresponding XTEM picture). However, the interface between the epi-film and the substrate is clearly visible, suggesting that the process condition is not optimized. A L_{12} orthogonal design of experiments is performed for optimizing the ECR hydrogen plasma predeposition wafer cleaning process. Table 7.3 summaries the cleaning conditions and results of all the cleaning experiments including the L_{12} experiments. After each cleaning experiment, the deposition conditions are kept the same. Using the E/FT-IR, we have eliminated many unnecessary post-deposition materials characterizations (e.g. Rutherford back scattering (RBS), cross sectional transmission electron microscopy (XTEM), and secondary ion mass spectroscopy (SIMS)). When we see an incubation time and/or a slow growth rate, we know that the cleaning process is ineffective and the epi-film is defective. Consequently, we would not perform those time consuming and costly post-deposition material characterizations. Thus, plasma cleaning process optimization time is shortened and post-deposition materials characterization cost is reduced.

Effect of Bias Voltage

We observed that a plus 10 Vdc bias applied to the wafer is important for reducing plasma damages. Previously, it is shown that hydrogen plasma cleaning of silicon dioxide requires ion bombardment [136]. Since the mass of hydrogen molecules is relatively small, one might expect minimum damage from hydrogen ions; however, severe damage by hydrogen ions was observed during the radio frequency hydrogen plasma cleaning process [136]. We found that a plus 10 volts DC bias is required to suppress damage by ECR hydrogen plasma. Figure 7.18(a) shows a XTEM picture of a sample that is cleaned by ECR hydrogen plasma at -50 Vdc bias. Clearly, an interface layer of about 30 nm is observed. We believe this interfacial layer is the damaged surface layer prior to film growth. Moreover, the contrast below the interface

(a)

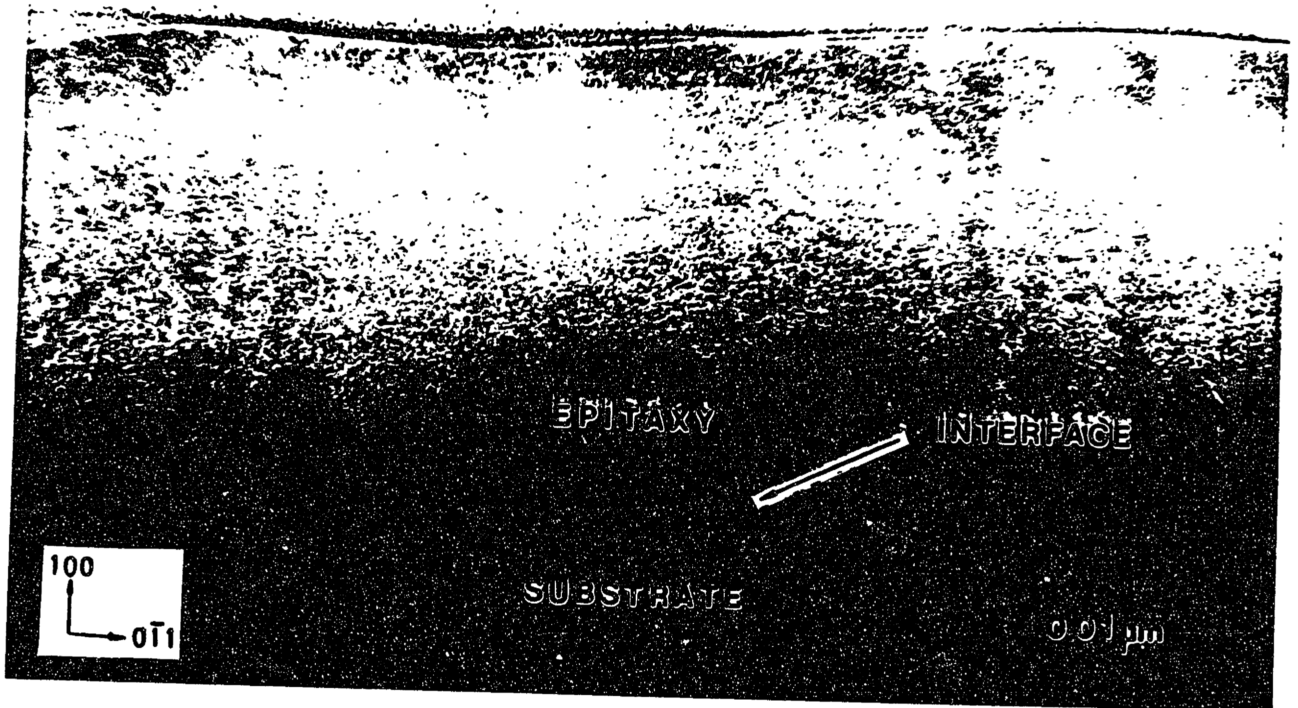

(b)

Figure 7.18: XTEM picture of epi-film grown after hydrogen plasma cleaning with (a) -50 Vdc bias, (b) 0 Vdc bias.

within the substrate, indicates possible stress field resulting from the defective film. Furthermore, the XTEM picture of a sample that is cleaned by ECR hydrogen plasma (under the same cleaning conditions) with a 0 Vdc bias shows a defect free film (see Fig.7.18(b)). However, the interface between the film and substrate of the sample is still clearly visible.

Figure 7.19(a) shows the real-time thickness monitoring results of a wafer that was cleaned under an optimized cleaning condition with a plus 10 volts DC bias. The deposition condition and the optimized plasma cleaning condition are specified in Figure 7.19(a). The corresponding XTEM picture (Fig. 7.19(b)) shows that this film was defect free and the epi-substrate interface was almost invisible. This indicated that the ECR hydrogen plasma did not damage the wafer surface and the surface was in good condition prior to film growth.

7.5 Summary

This chapter is centered on the applications of E/FT-IR. First, the E/FT-IR is used for studying the thermal radiation properties of silicon. The results lead to a better understanding of the radiative properties of silicon, which is important for the subsequent film thickness measurements using E/FT-IR. The *in-situ* infrared emission spectrum of a lightly doped (10-20 Ω-cm) silicon wafer at 200 °C was found to be extremely similar to its transmission spectrum at room temperature, although the bands are inverted. This similarity makes possible the E/FT-IR analysis and spectral interpretation by taking advantage of spectral library information and band assignments based upon the transmission technique. Furthermore, we observed that the emission intensity of the heavily doped sample is higher than that of the lightly doped sample. For film thickness measurements using IR emission technique, since the epi-film is lightly doped and the substrate is heavily doped, the source of IR radi-

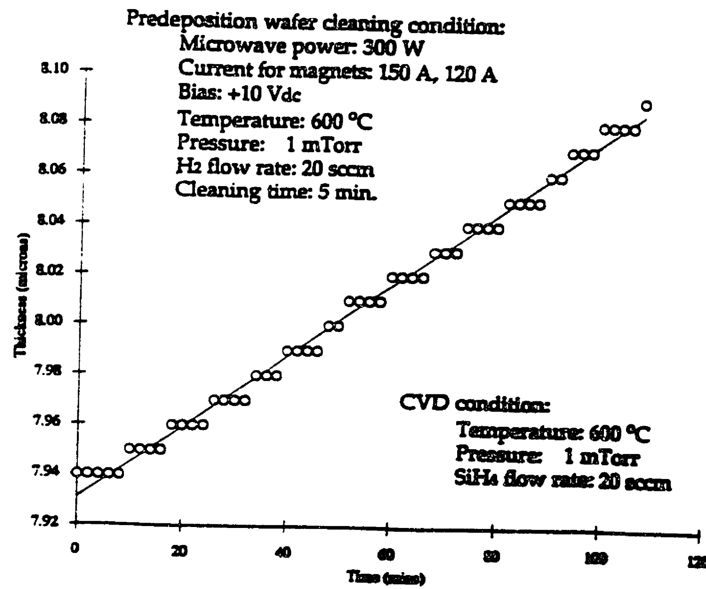

(a)

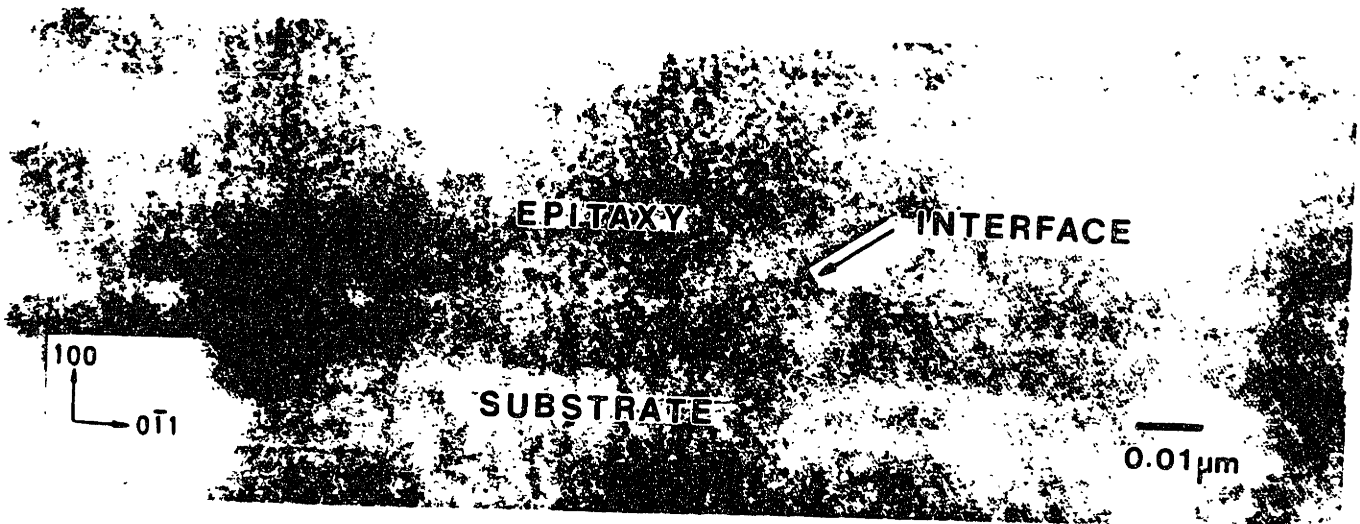

(b)

Figure 7.19: (a) Real-time in-situ film thickness monitoring during a CVD process after optimized hydrogen plasma predeposition cleaning; (b). XTEM picture of the corresponding defect free epi-film.

ation is the substrate. The heavily doped substrate emits IR radiation which travels through the epi-film producing the interferogram. The interferogram is recorded by the FT-IR spectrometer. Film thickness is then extracted from the interferogram.

After the demonstration of epi-film thickness measurement using E/FT-IR, we examined the limitations of the E/FT-IR technique from a theoretical point of view, as well as from an instrumental point of view. The minimum measurable film thickness limit is found to be 0.2 μm, and the precision is 0.01 μm. Moreover, issues such as the effect of heating lamp interference, window material, window stress and coating, temperature control and limitations, substrate dopant concentrations, repeatability and reproducibility, and wafer rotations, are addressed in detail. The effects of lamp radiation on E/FT-IR epi-film thickness measurement are minimum. The window material, window stress, and its coatings will not affect the film thickness measurement as long as sufficient light intensity reaches the FT-IR detector. Consequently, the window material must be IR transparent. There are two limits on wafer temperature. The lower temperature limit is due to the weak level of IR emission from the wafer. It is independent of substrate dopant concentration. However, the upper temperature limit is dependent on the substrate dopant concentration. The upper temperature limit is reached when the intrinsic carrier concentration of the film is about an order of magnitude below the extrinsic dopant concentration of the substrate. Both repeatability and reproducibility of the E/FT-IR technique are excellent. The repeatability of the E/FT-IR technique in terms of standard deviation (2δ) is 0.01 μm, in terms of coefficient of variation (2RS%) is about 0.1% for all temperatures (550°C, 610°C, and 660°C). The reproducibility of the E/FT-IR technique in terms of standard deviation (2δ) is 0.02 μm, in terms of coefficient of variation (2RS%) is about 0.3% for all temperatures (550°C, 610°C, and 660°C). When FT-IR thickness measurements are performed on a rotating wafer (with speed upto 55 RPM), we found that only a small amount of noise was introduced, and good measurement repeatability can still be maintained. Real-time *in-situ* applications of E/FT-IR in

silicon epitaxy are demonstrated in four areas: 1) silicon epitaxy (process) research, 2) silicon epitaxy (process) monitoring, 3) epi-film thickness control, and 4) plasma cleaning process development and optimization.

We concluded that real-time *in-situ* monitor offered several distinct advantages in process research:

1. Rapid feedback on growth rates can be obtained in real-time during one run (or fewer runs). Hence, reduces time to develop, update, and validate process models.

2. Measurement noise due to run to run variations (e.g. materials variation, initial condition variation, equipment drift, process drift, etc.), can be reduced, since data are obtained in one run (or fewer runs). Hence, more accurate kinetic rate constants make the model(s) more realistic.

3. Process flexibility can be increased by rapid tuning of models for new or different processes.

Additionally, from real-time *in-situ* film thickness data, two important parameter can be obtained. They are growth rates and incubation times. From growth rate, one can understand the process kinetics and improve the accuracy of the process models, thus lead to efficient process development, optimization and control. In addition, since the growth rate is critically dependent on process parameters, any variation in the process are reflected in changing growth rates. Consequently, process monitoring and control are demonstrated through the monitoring of growth rates. From incubation time, one can obtain a better understanding of the kinetics of polysilicon deposition. The measurements and understanding of incubation time allows one to optimize selective epi deposition, monitor predeposition wafer cleaning, and finally control film quality. For process monitoring, we found that the real-time growth

rate measured by the E/FT-IR is responsive to variations of process parameter(s) (e.g.temperature, pressure, and gas composition). For epi-film thickness control, two control algorithm were used: 1) first past the post (FPP) method; 2) linear forecasting. The FPP algorithm monitors the thickness continuously. Once a measurement is on or exceeds the target, the process will be terminated automatically. The E/FT-IR with 0.01μm precision resulted in a control limit of 0.005 μm using the FPP method. Using the linear forecasting algorithm, the growth rate was determined and continuously updated by taking the real-time measured film thickness data and by performing a linear regression on them. The process end-time was estimated and updated from the growth rate in real-time. This method reduced the effect of E/FT-IR measurement noise and improved the control limit to 0.003μm. Predeposition wafer cleaning is done *in-situ* using ECR hydrogen plasma. By real-time monitoring of incubation time and growth rate, we are able to obtain qualitative information about the effectiveness of the predeposition wafer cleaning process. When we see an incubation time and/or a slow growth rate, we know that the cleaning process is ineffective and the epi-film is defective. Consequently, we would not perform those time consuming and costly post-deposition material characterizations. Thus, plasma cleaning process optimization time is shortened and post-deposition materials characterization cost is reduced. Using the optimized conditions, we have demonstrated the growth of defect free epitaxial silicon films.

Chapter 8

Summary and Future Recommendations

8.1 Summary

The objective of this thesis is to explore and demonstrate the application of sensors in various stages of a semiconductor manufacturing process. For this research, a Fourier transform infrared spectrometer (FT-IR) is selected as a test vehicle, a low temperature silicon epitaxy process is selected as a test environment, and a low temperature silicon epitaxial chemical vapor deposition (CVD) reactor is selected as a test bed. In materials research, the applications of *ex-situ* reflection FT-IR for material characterizations and for obtaining critical optical parameters, have been demonstrated. In process research and development, the application of real-time *in-situ* ATR-FT-IR for investigating a surface cleaning process using plasma, has been illustrated. A new E/FT-IR technique for film thickness measurements is characterized and evaluated. Its capabilities and usefulness have been explored. The results demonstrated the power of E/FT-IR for real-time *in-situ* process monitoring and process control. The

following summary outlines some of the major accomplishments:

- Equipment:
  - Designed and built a flexible single-wafer cluster tool consistent UHV-CVD reactor
  - Implemented and characterized an electron cyclotron resonance (ECR) plasma source
- Sensor development:
  - Demonstrated and characterized a novel E/FT-IR sensor for epitaxial silicon film thickness measurements
  - Developed a theoretical basis for the understanding of E/FT-IR and FT-IR
  - Measured refractive index of silicon as a function of wavelength, dopant concentration, and sample temperature
- Process development:
  - Demonstrated effective in-situ predeposition wafer surface cleaning by ECR hydrogen plasma
  - Demonstrated the application of real-time in-situ monitors (E/FT-IR and ATR-FT-IR) for rapid R&D of plasma cleaning process
  - Demonstrated defect free epitaxial silicon film growth at 600 °C after in-situ ECR hydrogen plasma cleaning
- Process monitoring and control:
  - Demonstrated the application of E/FT-IR for real-time silicon epitaxy process monitoring

- Demonstrated the application of E/FT-IR for real-time close-loop feedback control of epi-film thickness
- Demonstrated ECR plasma pre-deposition wafer cleaning process optimization using E/FT-IR
- Demonstrated film quality evaluation by real-time monitoring of growth rate and incubation time

8.2 Other Applications of E/FT-IR

Real-time In-situ Monitoring of Dielectric Film Thickness by E/FT-IR

Dielectric films deposition (SiO_2, Si_3N_4) are necessary throughout the modern integrated circuit fabrication process. As design rules shrink to the submicron range for MOS ULSI, it becomes increasingly vital to grow thin dielectrics on silicon (in the 5 to 20nm range) in a repeatable manner. These oxides must also exhibit good characteristics and provide long-term reliability. Moreover, these dielectrics are active components of the storage capacitor in Dynamic RAMs, and their thickness determines the amount of charge that can be stored. Producing high quality and high reliability ICs requires the ability to deposit high quality dielectrics in a controllable and repeatable manner. Emission Fourier Transform Infrared Spectroscopy (E/FT-IR) is a non-contact and non-invasive technique which is suitable to measure the dielectric film thickness and possibly quality $in-situ$ and in real-time during process.

To test the feasibility of using Emission Fourier Transform Infrared (E/FT-IR) spectroscopy for $in-situ$ dielectric film thickness measurement, a simple experiment was first conducted. In this experiment, a wafer with lightly doped substrate (10-40 Ω-cm) is heated in a furnace with an observation window. The window material is

ZnSe for IR transmission. The Digilab Michelson interferometer is equipped with an emission port intended for E/FT-IR. During testing, the interferometer is placed close to the furnace so that the emission port is next to the window and IR emission from the wafer can arrive at the interferometer after a short travel. Radiation from the wafer at 1000 °C was collected and saved for subsequent analysis. Ideally, radiation from a blackbody placed in the furnace should be collected for reference, but it was not available to us at the time. So the radiation from the furnace (with nothing inside) was taken as the reference. Fig.8.1 shows the infrared emission spectra of the wafer after ratio against the reference. The Si-O phonon band around 1100 cm^{-1} is strong and clear, making calculation of the oxygen concentration straightforward. This initial concentration is believed to be the contributions from both the native oxide and oxygen impurity within the bulk of the substrate. By collecting the emission from the wafer in a fixed interval of time, then ratio against the same reference, one can clearly see the rising and broadening of the Si-O peak. By measuring the change in area under this peak, one can readily obtain the oxide thickness and therefore the growth rate. This technique is ideal for thin film thickness measurement, its minimum resolution is well below 10 nm. Furthermore, by carefully examining the shape and width of the band (peak), one can also deduce the quality of the deposited film. Because the band shapes are associated primary with relaxation phenomena, i.e. the interactions between the normal mode of vibration (Si-O) and all other oscillators (impurities) in the system. Although we have only demonstrated thermal oxidation in room air, the monitoring technique is equally applicable to any other forms of oxidation. For example, low temperature plasma oxidation, low temperature CVD of oxide, etc. It is also conceivable that using the same technique, nitridation can be monitored as well by tracking the Si-N peak around 875 cm^{-1}.

FTIR for Junction Depth Measurements

It would be useful to be able to measure the junction depth nondestructively.

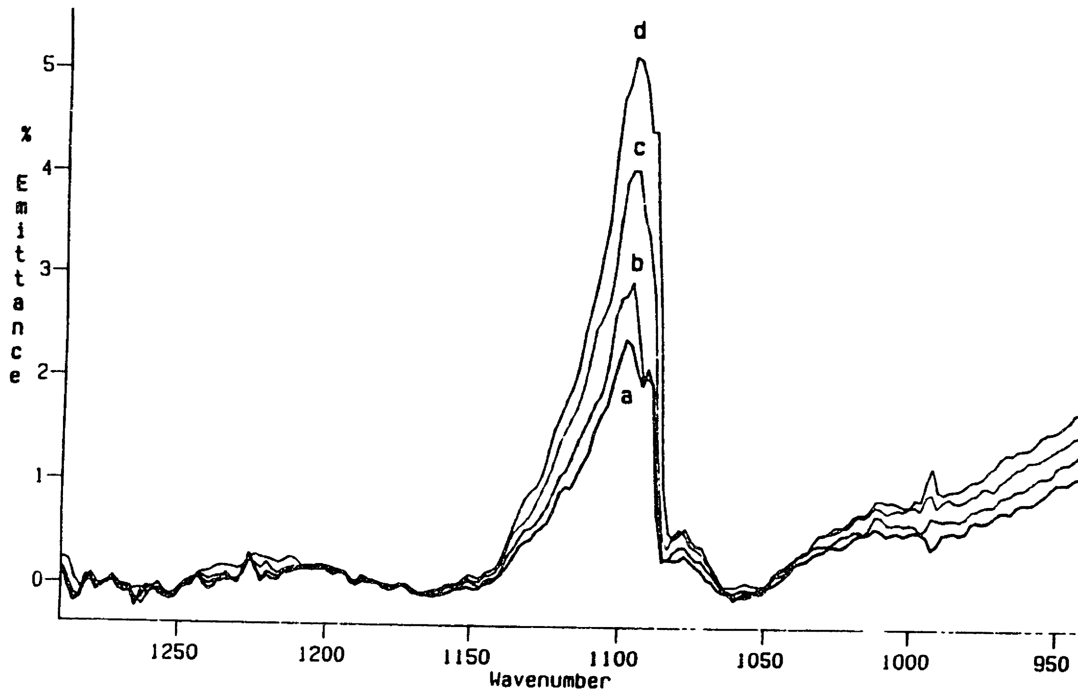

Figure 8.1: Real time monitoring of an oxidation process using the E/FT-IR

Moreover, as device dimensions become smaller, it would be greatly beneficial to measure junction depths in-situ and in real time. We have explored the junction depth measurement using FTIR. For this demonstration, we deposited a 0.5 μm and a 1 μm in-situ boron doped $p^+(>10^{19})$ epi on lightly doped substrates (10-20 Ohm-cm). The FTIR measured junction depths agreed well with those measured by other destructive techniques, e.g. spreading resistance profiling.

Impurity Identification by EFTIR

The infrared emission profiles from the high temperature substrates were collected by a standard FT-IR spectrometer. Differences in the emission spectra acquired from substrates are explained through correlation to the optical properties of the corresponding substrate. The *in – situ* infrared emission spectrum of a lightly doped (10-20 Ω -cm) silicon wafer at 200 °C is very similar to its *ex situ* transmission spectrum at room temperature, although the spectrum appears inverted. This similarity

makes the analysis of the E/FT-IR spectra straightforward, as the existing spectral libraries and standard spectral analysis methods can be applied directly. Finally, we have shown that the E/FT-IR technique can be applied *in – situ* to perform non-contact and non-invasive identification, and possibly quantification of impurities in semiconductors at elevated temperatures.

Kinetic Studies

The E/FT-IR is an ideal tool for studying kinetics of CVD processes. Among many interesting topics are: SiGe deposition, dopant incorporation, plasma assisted dopant incorporation. Growth rate enhancement was reported for SiGe depositions. In addition, growth rate enhancement was observed during in-situ doping. From E/FT-IR measurement of growth rates, a better understanding of SiGe growth mechanism and dopant incorporation mechanism is made possible.

Growth Rate Control

For atmospheric pressure CVD or low pressure CVD, most of the commercial reactors are not UHV. In this reactors, due to high level of contaminants, high growth rates must be maintained to minimize contamination in the films. Real-time growth rate control using E/FT-IR can be accomplished by controlling the deposition temperature and silane partial pressure. Temperature control can be realized by controlling of the heater power supply. Silane partial pressure can be controlled by tuning the mass flow controllers, or by adjusting the process pressure. This way, film quality can be assured regardless of process perturbations, and equipment/process drifts.

Thin Film Thickness Measurements

In order to overcome the minimum film thickness limitation of FT-IR, other film thickness measurement techniques are need to be explored. One possible idea is

to build an infrared ellipsometry using a carbon dioxide laser with a wave length of about 10.6 micron. There were a few published papers that uses infrared ellipsometry for epi-film thickness measurement. In one of these papers, the authors Hilton and Jones of Texas Instrument reported their results using a 54.6 micron infrared ellipsometry in 1966. Their results mostly covered thickness measurements between 1 and 10 micron, and not much details were provided for thickness below 1 micron. Recently, an infrared spectroscopic ellipsometer that combines the sensitivity of spectral ellipsometer and the analytical power of FT-IR spectrometer, are commercially available from Sopra, Inc. This FT-IR ellipsometer is ideally suited for *ex-situ* epi-film thickness measurements, although the minimum epi-film thickness limit has not yet been determined. This technique may not be useful for *in-situ* applications because of its slow measurement speed. For each measurement, data acquisition typically takes from 1 to 700 minutes depending on the sample material properties and the desired precision of the measurement. The data analysis time is on the order of 5 seconds to 2 minutes for single layer film, and on the order of 1 to 5 minutes for multilayers. Data reduction is also strongly dependent on the number of data points, the structure of the sample, and the method of calculation. Work needs to be carried out for identifying the limits and improving its capabilities.

8.3 Future Road Map

The process/equipment control roadmap is given in Figure 8.2. This roadmap articulated the trend and direction of process/equipment development from now to the year of 2007. The work accomplished in this thesis fits well in this picture, and is perhaps several years ahead of the game. According to the roadmap, real-time sensors will be incorporated in the semiconductor factory around year 2000. A description of the roadmap is given in the following:

Detailed Potential Solutions	1992	1995	1998	2001	2004	2007
Product Wafers to Total Wafers	70%			100%		
Sensors	Ex Situ	Inline	Real Time		In Product	
	Equipment Control Equipment State Process/Treatment State			Product State		
Process Control	Run by Run *Ex Situ Metrology		Run by Run *In Situ Metrology		Real Time *Wafer State	
Fault Detection	Wafer Testing		Physical Property		Inline	
Process Flexibility	Rigid				Flexible	
Linkage Roadmap	Manufacturing Systems; All Processes; TCAD					
CIM Connectivity	SECS		GEM			?

Figure 8.2: Semiconductor Industry Association (SIA) process and equipment control roadmap

Benefits: The major objective of process control is to increase the predictability of manufacturing process. Increases in predictability will significantly increase the asset utilization. Currently, as indicated on the roadmap, only 70% of total wafers are used for making products. The rest of the 30% wafers are test wafers (scraps) used in process calibration, or equipment certification. Materials as well as process time are wasted. These resources can be recovered by effectively using sensors together with process control algorithms.

Requirements: Sensor requirements are different in research environment as compare to production environment. The research system must be designed to facilitate development of fundamental models and isolation of the actual mechanism involved. Production sensors must be robust, non-invasive, and low cost. They must also be calibrated easily and the measurements must be interpreted simply.

Location: Sensor types will progress from *ex-situ*, to *in-situ*, to real-time, and to in product (embedded structures that provide data about product properties directly). Their locations migrates from outside the equipment, to inside the equipment, then to inside the process, and finally to inside the wafer.

Control and testing: The control methods will evolve from run-by-run control using ex-situ measurements, to run-by-run control using in-situ measurements, to real-time control by real-time monitoring of the physical and electrical characteristics of the wafer and devices. At the same time, the diagnosis of faults will progress from logical testing, to physical property sensing, to in-situ diagnosis based on local electrical property measurements.

The progression in sensors and controllers will increase manufacturing flexibility using flexible processes rather than rigid processes. At the same time, integration of the sensor and controller with other elements in the factory becomes important. The reader is referred to [10] for more details regarding these elements.

This thesis, although addresses only one sensor (FT-IR) and one process (silicon epitaxy), the results demonstrated here are very promising. It is a first step towards the implementation and the realization of the SIA roadmap.

Bibliography

[1] Betty Newboe, "Cluster Tools: A Process Solution?", Semiconductor International, p82, July 1990

[2] A.S. Bergendahl, *et. al.*, "Cluster Tools, Part2: 16Mb DRAM Processing", Semiconductor International, p.94, Sept. 1990.

[3] Industry News, "Wafer Fab Pricetag of $1 Billion Predicted", Semiconductor International, p22, Dec. 1989

[4] S.C. Wood and K.C. Saraswat, "Factors affecting the economic performance of cluster-based fabs", Proceedings of the Third International Symposium on Ultra Large Scale Integration Science and Technology. ULSI Science and Technology 1991.

[5] P. Berggraaf, "Epi's Leading Edge", *Semiconductor International*, 7, p68, 1991.

[6] J.H. Comfort, "Plasma enhanced chemical deposition of *in – situ* doped epitaxial silicon from silane at low temperatures," Doctoral Thesis, M.I.T., 1988.

[7] S.S. Iyer, *et al.*, " Heterojunction Bipolar Transistors Using Si-Ge Alloys," *IEEE Transactions On Electron Devices*, vol. 36, no. 10, p. 2043, 1989.

[8] G.G. Patton, *et al.*, "75-GHz f_T SiGe-Base Heterojunction Bipolar Transistors," *IEEE Transactions On Electron Devices*, vol. 11, no. 4, p. 171, 1990.

[9] W. Andrews, "IBM, Analog Devices SiGe Deal Spurs GaAs Attack", Electronic News, p.52, Dec. 13, 1993.

[10] Semiconductor Technology Working Group Reports, Semiconductor Industry Association, 1993.

[11] A. Hu, E. Sachs, A. Ingolfsson, and P. Langer, " Run-by-run process control: performance benchmarks" IEEE/SEMI International Semiconductor Manufacturing Science Symposium, San Francisco, CA, June 1992.

[12] R.A. Gottscho, *et. al.*, "Real-time monitoring of low-temperature hydrogen plasma passivation of GaAs", J. Appl. Phys. 68, 440, 1990.
Richard A. Gottscho, Head Display Research, AT&T Bell Laboratories, Murray Hill, NJ.

[13] R.A. Gottscho and T.A. Miller, "Optical Techniques in plasma diagnostics", Pure & Appl. Chem., V. 56, pp.189-208, 1984
(Richard A. Gottscho, Head Display Research, AT&T Bell Laboratories, Murray Hill, NJ, 07974).

[14] F.H. Pollak, "Photoreflectance for the in-situ monitoring of semiconductor growth and processing", SPIE V. 1361, p.109, 1990.
(Fred H. Pollak, Professor, Department of Physics, Brooklyn College of CUNY, Bedford Avenue & Avenue H, Brooklyn, NY 11210).

[15] D.E. Aspnes, "Real-time surface optical diagnostics for epitaxial growth", J. Vac. Sci. Technol., A 9 (3), p.870, 1991.
(David E. Aspnes, Professor, Department of Physics, North Carolina State University, Raleigh, NC 27695).

[16] G.G. Gifford, "Applications of optical emission spectroscopy in plasma manufacturing systems", Proc. SPIE v.1392, p.454-65, 1991.

[17] B.J. Curtis, Solid State Technology, v.23 No. 4, p239, 1980.

[18] E.O. Degenkolb, C.J. Mogab, M.R. Goldrick, and J.E. Griffths, Applied Spectroscopy, 30, p520, 1977.

[19] A. Banerjee and T. DebRoy, "Optical emission investigation of the plasma enhanced CVD of silicon oxide film", J. Vac. Sci. & Techn. A, v.10, p. 3395-3400, 1992.

[20] E.A. Rietman, et. al., "Active neural network control of wafer attributes in a plasma etch process", J. Vac. Sci. & Techn. B, v.11, p. 1314-6, 1993.

[21] R. Shadmehr, et. al., "Principal component analysis of OES and mass spectrometry: application to RIE process parameter estimation using neural networks", J. Elect. Chem. Soc., v. 139, p.907-14, 1992.

[22] V. Comello, "RGAs provide real-time process control", Semiconductor International, p.70-74, Sept. 1990.

[23] J.M Baker and D.D. Dimilia, "Real-time RGA Monitoring of Vacuum Manufacturing Process", Proceedings of 40th American Vacuum Society National Symposium, Orlando, Fl, Nov. 15-19, 1993.

[24] I.P. Herman, "Raman Scattering as an in-situ optical diagnostic", SPIE, V. 1594, 1992.
(Irving P. Herman, Professor, Department of Physics, Columbia University, New York, NY 10027)

[25] G.P. Hansen, *et. al.*, Applied Optics, 28, 10, 1989.

[26] D. Kirillov, J. Appl. Phys. 58, 3, 1985.

[27] Y.J. Lee, *et. al.*, "Photoacoustic measurement of silicon wafer processing temperatures"; IEEE Ultrasonics Symposium, 1989.

[28] Ircon Corp., "Introduction to Infrared Thermometry", Technical notes (#TN102).

[29] M.M. Moslehi, R.A. Chapma, *et. al.*, "Single-wafer ıntegrated semiconductor device processing", IEEE Trans. on Elect. Dev., 39, p.4-32, 1992.

[30] V.M. Donnelly and J.A. McCaulley, "Infrared-Laser Interferometric Thermometry", J. Vac. Sci. Technol. A 8, 1, 1990.

[31] D. Peyton, H. Kinoshita, G.Q. Lo, and D.L. Kwong, "Systems-oriented survey of non-contact temperature measurement techniques for rapid thermal processing", SPIE Vol. 1393, Rapid Thermal and Related Processing Techniques, p.295-308, 1990.

[32] P.H. Berning, Physics of Thin Film, Vol. 1, p.69, 1963.

[33] H.P. Kleinknecht, and H. Meier, J. Electrochemical Soc., Vol. 20, p.77, 1977.

[34] R.M.A. Azzam and N.M. Bashara, *Ellipsometry and polarized light*, North-Holland, Amsterdam, 1977.

[35] J.A. Wollam, *et. al.*, "in-situ and ex-situ ellipsometric characterization for semiconductor technology", SPIE, v. 1678, 246, 1992.
(John A. Wollam, Professor, Dept. of EE, University of Nebraska, Lincoln, NE 68588.)

[36] D.E. Aspnes, "New developments in SE: the challenge of surfaces", Thin Solid Films, V. 233, p.1-8, 1993.
(David E. Aspnes, Professor, Department of Physics, North Carolina State University, Raleigh, NC 27695.)

[37] D.E. Aspnes, *et. al.*, "Closed-loop control of growth of semiconductor materials and structures by SE", J. Vac. Scie. Techn. A, 10, p.1840, 1991;

[38] R.W. Collins and K. Vedam, "Ellipsometers", Encyclopedia of Applied Physics, V. 6, pp 191-205, 1993.
(Robert W. Collins, Professor, Department of Physics, The Pennsylvania State University, University Park, PA)

[39] E.A. Irene, "Applications of spectroscopic ellipsometry to microelectronics", Thin Solid Films, vol.233, no.1-2, pp. 96-111, 1993.
(E.A. Irene, Professor, Dept. of Chem., North Carolina Univ., Chapel Hill, NC 27599).

[40] S.W. Butler, *et. al.*, "An intelligent model based control system employing in-situ ellipsometry", Proceedings of 40th American Vacuum Society National Symposium, Orlando, Fl, Nov. 15-19, 1993. See also, C.T. Yu, K.H. Isaak, and R.E. Sheets, "using in situ ellipsometry for film thickness endpoint control", Semiconductor International, p.166-9, May 1991.

[41] S.A. Henck, W.M. Walter, L.M. Loewenstein, and J. Kuehne, "In situ spectral ellipsometry for real-time thickness measurement and control", Proc. SPIE, v.1803, p.299-308, 1992. See also, W.M. Duncan and S.A. Henck, "In situ spectral ellipsometry for real-time measurement and control", Applied Surface Science 63, pp.9-16, 1993.

[42] M.A. Nokes and P.G. Borden, "Profiling the wafer bulk", Microelectronics manufacturing technology, pp.33-38, Nov. 1991.

[43] J.E. Mahan, K.M. Geib, G.Y. Robinson, and R.G. Long, "A review of the geometrical fundamentals of RHEED with application to silicon surfaces", J. Vac. Sci. Technol., A 8, p.3692-3700, 1990.

[44] S. Nikzad, C.C. Ahn, and H.A. Atwater, "Quantitative analysis of semiconductor alloy composition during growth by REELS", J. Vac. Sci. Technol. B, Vol. 10, No. 2, p.762-765, 1992.

[45] S.S. Wong, S. Nikzad, C.C. Ahn, and H.A. Atwater," In-situ analysis of surface contaminant desoprtion during low temperature silicon substrate cleaning using REELS", Mat. Res. Soc., Symp. Proc., No. 259, 1992.

[46] L.C. Feldman and J.W. Mayer, *Fundamentals of surface and thin film analysis*, (North-Holland, New York, 1986)

[47] "Standard method for measuring resistivity of silicon wafers using a spreading resistance probe", 1984 Annual Book of American Society for Testing and Materials (ASTM) Standards, F525-84, v.10.05, p.455, 1984.

[48] A. Papoulis, *Circuits and Systems*, Holt, Rinehart and Winston Inc., New York, 1980.

[49] W.M. Siebert, *Circuits, Signals, and Systems*, The MIT Press, Cambridge MA, 1986.

[50] E.C. Titchmarch, *Introduction to the Theory of Fourier Integrals*, Oxford, Clarendon Press, 1937.

[51] P.R. Griffiths and J.A. Haseth, *Fourier Transform Infrared Spectrometry*, J. Wiley, New York, 1986.

[52] R.A. Carpio, "IR spectroscopy enhances dielectric film QC", Semicondcutor International, p100, August, 1989.

[53] W. Kern, R.K. Smeltzer, "Boronphosphosilicate glass for integrated circuits", Solid State Technology, p171, June, 1985.

[54] The American Society for Testing and Materials (ASTM), Committee F-1 on Electronics, Philadelphia, Pennsylvania.

[55] Y.J. Chabel, in *Studies of Semiconductor Surfaces: Vibrational Spectroscopy of Adsorbates*, (1992)

[56] P. Jakob and Y.J. Chabal, Appl. Phys. Lett. 59, 2968 (1991).

[57] Y.J. Chabal, G. Higashi, K. Raghavachari, and V. Burrow, J. Vac. Sci. Technol. A 7, 2104 (1989)

[58] Y.J. Chabal, *Surface Science Reports*, 8, 211, (1988)

[59] N.J. Harrick, *InternalReflectionSpectroscopy*, (Eiley, New York, 1967).

[60] Y.J. Chabel, Surf. Sci. 168, 594 (1986)

[61] R. Eisberg and R. Resnick, *Quantum Physics of Atoms, Molecules, Solids, Nuclei, and Particles*, (John Wiley & Sons, New York, 2nd Ed., 1985).

[62] T.S. Moss, G.J. Burrell and B. Ellis, *Semiconductor Opto – Electronics*, Butterworths, London, (1973)

[63] S.V. Compton, D.A. Compton, and R. Messerschmidt, *Spectroscopy*, 6, 35, (1991)

[64] F. Cahn and S. Compton, *Applied Spectroscopy*, 42,865, (1988)

[65] O.S. Heavens, *Optical Properties of Thin Solid Films*, Butterworths Scientific Publications, Ltd., 1955.

[66] F. Yu, Z.H. Zhou, P. Stout, R. Reif, "*In – situ* Monitoring of Epitaxial Film Thickness by IEMI", *IEEE Trans. on Semicon. Manufac.* 5, 34, 1992.

[67] D.L. Rehrig, " In search of precise Epi thickness measurements", *Semiconductor International*, 11, 90, November 1990.

[68] P.J. Severin, "The influence of the phase shift on thickness measurements of silicon epitaxial layers with a fouries transform spectrometer" *J. Electrochem. Soc.*, 121, pp150-153, (1974)

[69] P.A. Schumann, Jr., R.P. Phillips, and P.J. Olshefski, "Phase shift corrections for infrared interference measurement of epitaxial layer thickness" *J. Elec. Chem. Soc.*, 113, pp368-371, (1966)

[70] Z.H. Zhou, I. Yang, F. Yu, and R. Reif, "Fundamentals of Film Thickness Measurements Using Reflection and Emission Fourier Transform Infrared Spectroscopy", Journal of Applied Physics, 73 (11), p7331-7, 1993. *J. Appl. Phys.*, 73 (11), p7331, (1993)

[71] Z.H. Zhou, S. Compton, I. Yang, and R. Reif, *IEEE Trans. on Semicon. Manufac.* (1993) (in press)

[72] L. Wooten, *Optical properties of solids*, Academic Press, New York, Chapter 3 and 6, (1972)

[73] V.K. Subashiev, G.B. Dubrovskii, and A.A. Kukharskii, "Determination of the optical constants and free carrier concentration from the coefficient of reflection in highly doped semiconductor materials", Soviet Physics Solid State, V.6, No.4, pp830-832, (1964)

[74] S.M. Sze, *VLSI Technology*, McGraw-Hill, New York, p. 90, (1988)

[75] S. Wang, *Fundamentals of Semiconductor Theory and Devices Physics*, Prentice Hall, Englewood Cliffs, New Jersey, p.243, (1989)

[76] S.M. Sze, *Physics of Semiconductor Devices*, J. Wiley, New York, p. 19, (1981)

[77] J.C. Hensel, and G. Feher, "Cyclotron resonance experiments in uniaxially stressed silicon: valence band inverse mass parameters and deformation potentials", Physics Review, V. 129, 3, pp1041-1062, (1963)

[78] Z.H. Zhou, F.Z. Yu, and R. Reif, "A Multi-chamber Single-wafer CVD reactor and ECR plasma for flexible IC manufacturing", *J. Vac. Sci. Tech.*, B.9 (2), 374, (1991).

[79] F. Lukes, "The temperature dependence of the refractive index of silicon" Czechosl. J. Phys. B10, pp317-326, (1960).

[80] E. Antoncik, "On the theory of temperature dependence of the refractive index of homopolar crystals", Czechosl. Journ. Phys., 6, pp209-216, (1956)

[81] F. Lukes, "On the theory of the temperature dependence of the refractive index of insulators and semiconductors", Czechosl. Journ. Phys., 8, pp423-433, (1958)

[82] C. Cannali, C. Jacoboni, F. Nava, G. Ottavaini, and A. Alberigi-Quaranta, "Electron drift velocity in silicon", Phys. Rev. B, 12 (4), pp2265-2284, (1975)

[83] G. Ottavaini, L. Reggiani, C. Cannali, and A. Alberigi-Quaranta, "Hole drift velocity in silicon", Phys. Rev. B, 12 (8), pp3318-3329, (1975)

[84] I. Yang, Z.H. Zhou, F. Yu, Z. Ye and R. Reif, *Technical Conference Proceedings*, SEMICON/EUROPE (1992)

[85] B. Senitzky and S.P. Weeks, "Infrared reflectance spectra of thin epitaxial silicon layers" *J. Appl. Phys.* 52 (8), pp 5308-5314, (1981)

[86] B.E. Deal, M.A. McNeilly, D.B. Kao, and J.M. de Larios, Elec. Chem. Soc. Meeting, Extended Abstract No. 393, (1990)

[87] W.R. Burger and R. Reif, J.Appl.Phys. 62, 4255, (1987)

[88] L.M. Garverick, J.C. Comfort, T.R. Yew and R. Reif, J.Appl.Phys. 62, 3398, (1987)

[89] D.W. Greve and M. Racanelli, "Growth rate of doped and undoped silicon by ultra-high vacuum chemical vapor deposition", Journal of the Electrochemical Society, vol.138, no.6, p. 1744-8, 1991.

[90] M. Racanelli and D.W. Greve, Appl. Phys. Lett., 56, 2524, 1990.

[91] S.M. Gates, C.M. Greenlief, S.K. Kulkarni, and H.H. Sawin, J. Vac. Sci. Technol., A8, 2965, 1990.

[92] E. Kasper, App. Phys. A, 28, 129, 1982.

[93] R. J. Bennet and P.W. Gale, Philos. Mag., 22, 135, 1970.

[94] T.R. Yew,"Growth and characterization of low temperature silicon selective epitaxy", Ph.D. Thesis, Dept. Materials Science and Engineering, MIT, 1990.

[95] J. Murota, *et. al.*, "Low temperature silicon selective deposition and epitaxy on silicon using thermal decomposition of silane under ultraclean environment", Appl. Phys. Lett., 54 (11), pp. 1007-9, 1989.

[96] M. Delfino, S. Salimian, D. Hodul, A. Ellingboe, and W. Tsai, J. Appl. Phys., 71, 1001 (1992)

[97] T.R. Yew and R. Reif, J. Appl. Phys. 68, 4681, (1990)

[98] B. Anthony, T. Hsu, L. Breaux, R. Quian, S. Banerjee, and A. Tasch, J. Elec. Mats. 19, 1027 (1990)

[99] E.S. Aydil, K.P. Giapis, R.A. Gottscho, V.M. Donnelly, and E. Yoon, submitted to J. Vac. Sci. Techn. (1992)

[100] H. Ogawa and T. Hattori, Appl. Phys. Lett., 61, 577, (1992)

[101] E.S. Aydil, Z.H. Zhou, R.A. Gottscho, to be published.

[102] R.A. Gottscho, B.L. Preppernau, S.J. Pearton, A.B. Emerson, and K.P. Giapis, J. Appl. Phys. 68, 440 (1990)

[103] D.J. Eaglesham, G.S. Higashi, and M. Cerullo, Appl. Phys. Lett., 59, 685, (1991)

[104] S.R. Kasi, M. Liehr, *et.al.*, Appl. Phys. Lett., 59, 108 (1991)

[105] J. Abrefah and D.R. Olander, Surf. Sci. 209, 291 (1989)

[106] R.E. Thomas, M.J. Mantini, R.A. Rudder, D.P. Malta, S.V. Hattangady, and R.J. Markunas, presented at AVS, Seattle, WA. (1991)

[107] J.H. Comfort and R. Reif, "Plasma enhanced chemical vapor deposition of in-situ doped epitaxial silicon at low temperatures: I. Arsenic doping," *J. Appl. Phys.*, vol. 65, p. 1053, 1989.

[108] W.R. Burger and R. Reif, " A low-temperature CVD process for the deposition of device quality epitaxial silicon," *J. Materials Science and Engineering*, vol. B1, p. 131, 1988.

[109] G.R. Srinvasan, B.S. Meyerson, "Current status of reduced temperature silicon epitaxy by chemical vapor deposition," *J. Electrochem. Soc.*, vol. 134, no. 6, p. 1518, 1987.

[110] M.L. Green, *et al.*, "High-quality homoepitaxial silicon film deposited by rapid thermal chemical vapor deposition," *J. Appl. Phys.*, 65 (6), p. 2558, 1989.

[111] B.S. Meyerson, *et al.*, "Nonequilibrium boron doping effects in low temperature epitaxial silicon," *Appl. Phys. Lett.*, 1986.

[112] Z.H. Zhou, "A multichamber, UHV/CVD system with in-situ monitors and ECR plasma for flexible IC manufacturing", Master Thesis, Dept. of Electrical Engineering and Computer Science, MIT, 1989.

[113] K. Krishnan, P.J. Stout, in *Practical Fourier Transform Infrared Spectroscopy*, edit by J.R. Ferraro, K. Krishnan, Chap.6, 285, Academic Press, 1990.

[114] K. Krishnan, *ASTM Spec. Tech.*, Publ. 850, 358, 1984.

[115] L.I. Maissel and R. Glang, *Handbook of thin film technology*, McGraw-Hill, New York, p. 11-29, 1970.

[116] J.K. Wilmshurst, *J. Chem. Phys.* 39, 2545 (1963)

[117] M. A. Ford and R. A. Spragg, *Appl. Spectrosc.* 40, 715 (1986) 58479

[118] J. L. Lauer and P. Vogel, *Appl. of Surf. Sci.* 18, 183 (1986)

[119] T.M. Niemczyk, B. Wangmaneerat, and D.M. Haaland, *SRC Publ.* No. C91229, March, (1991)

[120] Z.H. Zhou, *et. al.*, *J. Appl. Phys.* (in press) (1993)

[121] Karen Horrell, *Introduction to Measurement Capability Analysis*, SEMATECH Technology Transfer Publication No. 91090709A-ENG, 1991

[122] L.I. Maissel and R. Glang, *Handbook of thin film technology*, McGraw-Hill, New York, p. 11-29, (1970)

[123] S.M. Sze, *VLSI Technology*, McGraw-Hill, New York, p. 90, (1988)

[124] S.M. Sze, *Physics of Semiconductor Devices*, J. Wiley, New York, p. 19, (1981)

[125] Y.H. Lee, Z.H. Zhou, D.A. Danner, P.M. Fryer, and J.M. Harper, "Chemical sputtering of Al_2O_3 by fluorine-containing plasmas exited by electron cyclotron resonance", *J. App. Phys.*, 68, p. 5329, 1990.

[126] Y.H. Lee and Z.H. Zhou, "Threshold energy for SiO_2 reactive ion etching," IBM research report RC 15408, 1990.

[127] W.H. Southwell and W.J. Gunning "High-speed ellipsometry for thin-fim deposition monitoring," SIPE vol. 1019, *thin film technologies III*, p. 84, 1988.

[128] H.F. Hazebroek and W.M. Visser, "Automatic laser interferometric ellipsometry and precision reflectometry," *J. Phys. E : Sci. Instrum.*, vol. 16, p. 654, 1983.

[129] K. Sufawara, K. Yoshimi, and H. Okuyama, "*In situ* monitoring of film deposition using He-Ne laser system," *J. Electrochem. Soc.*, vol. 120, no. 2, p. 287, 1973.

[130] P.D. Krasicky, R.J. Groele, and F. Rodriguez, "A laser interferometer for monitoring thin film process: Application to polymer dissolution," *Chem. Eng. Comm.*, vol. 54, p. 279, 1987.

[131] K.L. Saenger, and H.M. Tong, "Laser interferometric measurement of polymer thin film thickness changes during processing," *J. Appl. Polym. Sci.*, vol. 33, p. 1777, 1987.

[132] R. Loudon, *The Quantum Theory of Light*, second edition, Oxford University Press, New York, 1983.

[133] M.I. Flik and Z.M. Zhang, "Influence of nonequivalent detector responsivity on FT-IR photometric accuracy", to appear in *J.Q.S.R.R.*, 1991.

[134] I. Yang, P. Stout, Z.H. Zhou, R. Reif, F. Yu, "IEMI for in-situ real-time film thickness determination", submitted to IEEE Trans. on Semicon. Manufact. 1993.

[135] O. Marenzi, *Real Time Epitaxial Silicon Film Thickness Control*, Master Thesis in Mechanical Engineering, MIT, June 1993.

[136] Z.H. Zhou, E. Adyil, R.A. Gottscho, Y.J. Chabal, R. Reif, "Real-time, In situ Monitoring of Room-Temperature Silicon Surface Cleaning Using Hydrogen and Ammonia Plasmas", *J. Electrochem. Soc.*, 140 (11), p3316-21, (1993)